NUMERICAL SIMULATION OF INTERNAL FLUIDISATION AND CAVITY EVOLUTION DUE TO A LEAKING PIPE USING THE COUPLED DEM-LBM TECHNIQUE

XILIN CUI

BEng

A thesis submitted to The University of Birmingham

for the degree of

DOCTOR OF PHILOSOPHY

School of Civil Engineering

The University of Birmingham

November 2012

ABSTRACT

Motivated by internal fluidisation due to a leaking pipe, this thesis aims to achieve a deeper understanding of the leakage-soil interaction by numerical simulations. The coupled DEM (Discrete Element Method) – LBM (Lattice Boltzmann Method) technique has been regarded as a promising tool to efficiently provide detailed description of fluid-particle systems, especially with intensive fluid-particle interactions. Therefore, *FPS-BHAM,* a 2D DEM-LBM computer code is developed for this thesis. In this code, DEM models the soil as an assembly of circular particles, and LBM is employed for fluid flow simulations. The Immersed Moving Boundary (IMB) scheme is adopted for the treatment of fluid-particle interaction.

Numerical results are validated against existing experimental findings. Different regimes of bed behaviour are demonstrated under various flow rates. The onset of fluidisation is studied by analytically deriving for the flow equation and fluidising pressure, which are compared with numerical solutions. Moreover, deeper insights are made into the post-fluidisation phenomenon. The mechanism underlying a stable cavity is explored, and how a cavity evolves with different factors is also investigated through parametric studies.

KEY WORDS: Discrete Element Method, Lattice Boltzmann Method, numerical simulation, pipe leakage, fluidisation, cavity

ACKNOWLEDGEMENTS

I firstly give praise to Lord Jesus Christ, who is the creator of the world, and thank Him for the wisdom and strength gifted me to accomplish this thesis.

My most gratitude goes to my supervisors: Prof Andrew Chan and Dr David Chapman for their far-sighted guidance, kind help, patient advices, as well as encouraging support throughout the course of my PhD research. My great appreciation also goes to my husband and dearest friend, Mr Jun Li, who is also my colleague, for his steadfast love and encouragement.

I wish to extend my gratitude to Dr Colin Thornton and Prof Charley Wu for their help using the *TRUBAL* code and wisely suggestions given to me. I wish to express my great appreciations to Dr Alexander Royal, Prof Christopher Rogers, Dr John Bridgeman, Dr Hassan Hemida, Prof Christopher Clayton, and Dr Majed Alsaydalani for their kind help and advices on the validation work against experimental results. My sincere thanks also go to Prof Yuntian Feng and Prof Curt Koenders for their kind advices and encouragement.

I would like to thank the BlueBEAR Committee for their efficient technical supports throughout the course of this thesis. A great thank also goes to School of Civil Engineering for providing me a 3-year fully-funded PhD studentship.

I wish to extend my thanks to my former tutors and mentors: Prof Mark Sterling, Dr Yingang Du, and Prof Longyuan Li for their kind help and encouragement. A special gratitude also goes to Ms Helen Booth for her kind support and sweet smiles.

Finally, I thank my parents for their self-giving love and encouragement.

CONTENTS

LIST OF FIGURES, TABLES, SYMBOLS, AND ABBREVIATIONS

List of Figures

List of Tables

List of Symbols

c	global damping coefficient for translational motion
c'	global damping coefficient for rotational motion
c_u	undrained shear strength
C	LBM lattice speed
C_d	drag coefficient
C_s	speed of sound
D	centre-to-centre distance of two particles
d_p	particle diameter
E^*	effective contact Young's modulus
$\mathbf{e}_0$	zero velocity of fluid particle in LBM
$\mathbf{e}_i$	prescribed discrete velocities in LBM
$\mathbf{F}$	total force applied to particle
$\mathbf{F}_\mathrm{b}$	body force
$\mathbf{F}_\mathrm{c}$	total contact force

$\mathbf{F}_\mathrm{d}$	drag force on a single particle
$\mathbf{F}_\mathrm{h}$	fluid-induced force applied to particle
$\mathbf{F}_\mathrm{n}$	normal components of total contact force
$\mathbf{F}_\mathrm{t}$	tangential components of total contact force
F	upward drag force applied to the uplifting wedge
F'	effective normal contact force
F_0	upward drag force applied to the wedge at the onset of fluidisation
F_c	inter-particle adhesion force (i.e. 'pull-off' force)
F_{nd}	normal dashpot force
F_{slc}	sliding force
F_{tc}	critical tangential force for peeling process
F_{td}	tangential dashpot force
f_i	density distribution functions used in LBM
$\tilde{f}_i$	filtered density distribution functions in LBM turbulence modelling
f_i^{eq}	equilibrium density distribution functions used in LBM
$\tilde{f}_i^{eq}$	filtered equilibrium density distribution functions in LBM turbulence modelling
G	shear modulus
G^*	effective contact shear modulus
g	gravitational acceleration
H	bed height
H'	equivalent bed height

Δh	unity lattice spacing in LBM
I	particle moment of inertia
K	ratio of inter-particle adhesion force to average particle weight
k_n	normal contact stiffness
k_t	tangential contact stiffness
L_0	orifice size
m	particle mass
m^*	effective mass
Ma	Mach number
N	number of DEM sub-cycles within one LBM cycle
$\mathbf{n}$	unit normal vector
p	fluid pressure
p_0	theoretical fluidising pressure
Δp_f	fluidising pressure
Q	flow rate
Q_0	theoretical critical flow rate for growing-cavity generation
R	particle radius
R^*	effective contact radius
R_{ave}	averaged particle radius
R_h	hydraulic radius
S_c	Smagorinsky constant

$\mathbf{T}$	total torque applied to particle
$\mathbf{T}_c$	torque generated by contact force
$\mathbf{T}_h$	torque generated by fluid-induced force
T	volumetric submerged weight of the uplifting wedge
t	time
Δt_c	critical DEM time step
Δt_{DEM}	DEM time step
Δt_{LBM}	LBM time step
$\mathbf{u}$	flow velocity
$\mathbf{u}_b$	velocity of solid particle at the nominal boundary point in IMB
u_{in}	interstitial velocity
$u_{\max}$	maximum fluid velocity
V	cavity size
W	bulk weight of the uplifting wedge
$\mathbf{x}$	coordinates
$\boldsymbol{\alpha}$	relative approach of two particles
α_w	the complement of wedge angle
$\Delta\boldsymbol{\alpha}$	relative normal displacement increments within a DEM time step
β	contact damping factor
Γ	particle surface energy
$\boldsymbol{\delta}$	tangential displacement between two particles

$\Delta\boldsymbol{\delta}$ relative tangential displacement increments within a DEM time step

ε porosity

ε_0 initial bed porosity

$\boldsymbol{\theta}$ particle rotation

λ local solid/fluid ratio

μ inter-particle friction coefficient

μ_f dynamic viscosity of fluid

ν Poisson's ratio

ρ_f fluid density

ρ_p solid particle density

ρ_w water density

τ a dimensionless relaxation time in LBM

τ_{total} total relaxation time used in LBM turbulence modelling

υ kinematic viscosity of fluid

υ_t turbulence viscosity

ϕ_s particle sphericity

χ inclination angle of the wedge drawn for force calculations

$\boldsymbol{\Omega}$ rotation of contact plane

Ω_i^s bounce-back of non-equilibrium part of density distribution functions

$\boldsymbol{\omega}$ particle angular velocity

ω_0 bed thickness

List of Abbreviations

BALL	A two-dimensional DEM computing program developed originally by Cundall (1978)
BGK model	The lattice Bhatnagar-Gross-Krook model
CFD	Computational Fluid Dynamics
CPU	Central Processing Unit
DEM	Discrete Element Method
DEM-CFD	A numerical technique coupling the discrete element method and the computational fluid dynamics model
DEM-DFF	A numerical technique coupling the discrete element method and the Darcy fluid flow model
DEM-LBM	A numerical technique coupling the discrete element method and the lattice Boltzmann method
DEM-SPH	A numerical technique coupling the discrete element method and the smoothed particle hydrodynamics model
DFF	The Darcy Fluid Flow model
DNS	Direct Numerical Simulation
D2Q9 model	A two-dimensional LBM model with nine discretised velocities
FPS-BHAM	short name of *Fluid Particle System-Birmingham*, a DEM-LBM computing program developed to model fluid-particle systems in this thesis

IMB	Immersed Moving Boundary scheme
JKR model	The Johnson-Kendall-Roberts model, a theoretical model of elastic contact with the consideration of effect of adhesion (Johnson et al., 1971)
LBM	Lattice Boltzmann Method
LES	Large Eddy Simulation
LGA	Lattice Gas Automata
PIV	Particle Image Velocimetery
SPH	Smoothed Particle Hydrodynamics
TRUAL	A three-dimensional DEM computing program extended from BALL, originally developed by Cundall and Strack (1979c)

CHAPTER 1: INTRODUCTION

1.1 Problem Statement

Pipes buried underground are widely used to transport water and sewage waste for water distribution and drainage. However, underground pipes may suffer from leaks caused by a number of factors, such as corrosion, external loads, and internal pressure (Makar, 2000). In recent years, accidents triggered by pipe leakage have been reported all over the world. The accidents are usually found in the form of a sinkhole, in which ground surface collapses due to a leak from an underground pipe (see Figure 1.1). A major spill took place at the Kemira Kemi site in Helsingborg, and recognised as the biggest chemical accident in Swedish history, was mainly caused by a major leak from a nearby underground concrete cooling-water pipe (Söderlund et al, 2007). In such a case, the foundation of a big sulphuric acid tank was undermined by the leakage, generating a subsurface cavity with around 1000 m^3 in size. This led to a sudden tank failure and a release of a large amount of sulphuric acid in a very short time.

It is clear that such an underground cavity would act as a potential threat to surrounding infrastructures due to the lack of any early warning of the problem. Due to the fact that it is not possible to 'see' how they are behaving, it is necessary to understand the soil behaviour better when subjected to leakage from buried pipes. Previous laboratory studies (Royal et al., 2008; Rogers et al., 2008; Supraksorn, 2009; and Zoueshtiagh and

Merlen, 2007) have revealed different failure modes in the soil bed, which are dependent on the internal pipe fluid pressure and flow rate. In addition, a two-dimensional experimental work has also been conducted (Alsaydalani, 2010), whereby an internal fluidisation has been identified as the mechanism underlying the soil subject to a locally injected fluid. However, as only limited data could be acquired from the laboratory monitor system, a full knowledge of bed regimes, the flow field, and the post-fluidisation behaviour still requires further investigation.

(a) (b)

Figure 1.1 Sinkholes formed due to a pipe leakage problem: (a) Sinkhole in downtown London, 31st October, 2007 (Steindorff, 2008); (b) Sinkhole on the Ring Road at the University of Birmingham, 26th September, 2011.

Challenges are raised by a pipe leakage problem due to its complicated nature. It has been argued that fluid flow would be non-laminar at the vicinity of a leak (van Zyl and Clayton, 2007). In Alsaydalani (2010), higher pressure gradients were found near the source of a

local leakage, indicating localisation behaviour in the flow field. In addition, once fluidisation occurs, a localised cavity forms near the leak area. Within the cavity, intensive fluid-soil interactions may be involved, where soil particles may leave the soil matrix and move with the leaking fluid. Due to the localised large displacements in the soil, continuum analytical methods would encounter difficulties. Besides, laboratory approaches are regarded as limited due to their lack of flexibility and difficulties of data acquisition especially under three-dimensional conditions. In an effort to overcome the above drawbacks, numerical simulations using an appropriate technique should be applied, so that such a complicated behaviour in the leakage-soil interaction can be efficiently simulated.

1.2 Aim and Objectives of the Research

This thesis is motivated by the problems stated in Section 1.1. Its primary aim is to provide deeper understanding of the leakage-soil interaction by numerical simulations using an appropriate technique. It consists of the following objectives:

- to identify an appropriate numerical technique for efficiently simulating the complicated behaviour of the leakage-soil interaction, and to establish a computer code with the capability of performing the numerical simulations of a pipe leakage problem;
- to achieve a more thorough understanding of the internal fluidisation induced by

a local leakage, including a full knowledge of the bed regimes, flow field, and post-fluidisation behaviour; and

- to quantify the cavity evolution due to the local leakage, so as to provide more practical meanings from the numerical results.

1.3 Thesis Layout

This thesis is divided into eight chapters. Chapter 2 provides a literature review of previous work on leakage-soil interaction, and typical numerical techniques applied to geotechnical engineering. The coupled DEM-LBM technique is then identified as a promising tool for the simulation of the associated phenomena of internal fluidisation. Since no appropriate open source code was found, a computer program had to be developed initially and the relevant algorithms and implementations are presented in Chapter 3. In order to verify the newly-established code, a series of simple tests to examine different simulation functions were conducted and these are reported in Chapter 4. These include describing the particle-particle/particle-wall interactions, the fluid flows with various boundary conditions, as well as the fluid-solid two-phase interactions. In Chapter 5, the onset of fluidisation is investigated using the newly-established DEM-LBM code, and the numerical results are validated against existing experimental data and analytical derivations. The main findings on different bed regimes and fluidising mechanism are also demonstrated in Chapter 5. As numerical

simulations indicate the existence of a stable-cavity regime, Chapter 6 explores its underlying mechanism using the DEM-LBM code. This is then followed by parametric studies on the cavity evolution after fluidisation occurs, as presented in Chapter 7. By analysing the numerical results using a curve fitting technique, the cavity size is expressed as functions of time, controlled flow rate, controlled pressure in the pipe, and the ratio of inter-particle adhesion to average particle weight. Finally, in Chapter 8, the main conclusions are drawn from the research, and suggestions are given for potential future research.

CHAPTER 2: LITERATURE REVIEW

2.1 Introduction

In this chapter, the interaction between a leaking fluid and the surrounding soil is firstly reviewed in Section 2.2. As numerical simulations are performed in this thesis, Section 2.3 reviews the numerical modelling of geotechnical problems using DEM, which is a widely-used method for granular material simulations. With a focus on liquid-solid two-phase applications, Section 2.4 presents a review of DEM coupled with different fluid models. The coupled DEM-LBM technique is then regarded as a promising tool to fulfill the aim of this thesis, which is capable to describe the localisation phenomenon and bed behaviour in internal fluidisation. Therefore, a review of the DEM-LBM applications is then provided in Section 2.5. A summary of this chapter is finally given in Section 2.6.

2.2 Review of Leakage-Soil Interaction

2.2.1 General

Failures of buried water pipes are mostly found in cast iron pipes (Rajani and McDonald, 1994; and Kunkel et al., 2008), and the causes of failure can be varied, including corrosion, fatigue due to cyclical operating water pressure, and the external loads due to heavy traffic and differential settlement, and seasonal changes in the soil (Makar, 2000; Clayton et al., 2010; Rajani and Kleiner, 2012; and Rajani et al., 2012).

However, among literatures, the studies on the leakage-soil interaction due to a buried leaking pipe are found to be limited. Attentions have been paid to the leakage-induced moisture changes in expansive soils which result in differential foundation movement (Wray et al., 2004; and Li, 2006). In these studies, numerical simulations based on the moisture diffusion equation were adopted. Nevertheless, it is regarded problematical surrounding the leaking area where soil structure may undergo large displacements and fracturing, and the continuum method is no longer applicable. In recent years, leakage-induced accidents for which surrounding soils are largely deformed by leaking fluid from a buried pipe have been reported all over the world (Söderlund et al., 2007; Steindorff, 2008; Lynch and Stimpson, 2011; and Elhoud, 2012). Although such cases have brought about safety and economic issues to the modern society, it is surprising that not many literatures addressing the leakage-soil interaction with the local large displacements have been published.

A number of researchers carried out laboratory tests on fine-grained soils subject to leakage from a water pipe under different internal pressure values (Royal et al., 2008; Rogers et al., 2008; and Supraksorn, 2009). Three failure mechanisms in the soil were identified: (i) permeation of the leaking fluid into soil; (ii) cavity being created within the soil; and (iii) the soil being ruptured with the leaking fluid migrated up to the top surface. Due to the limitation of laboratory tools to detect within the samples, how these mechanisms were induced and how they acted remain unconfirmed. Similarly, an

experimental study on a granular bed, which is subject to a vertically injected fluid, led to an observation of three distinct bed regimes with respect to flow rate (Zoueshtiagh and Merlen, 2007): (i) a motionless bed; (ii) a local bump-shaped deformation at the bed surface; and (iii) a local fluidisation at the bed surface. However, such a three-dimensional study did not allow observations made inside the bed. Therefore, what happens within it still remains unclear.

From further experimental findings, it has been recognised that a leakage from an underground pipe can result in the build-up of pore water pressure and hydraulic gradients within the soil bed (Al-Karni, 1995; and Al-Karni, 2000). This was also noticed by Alsaydalani (2010) and was argued to be a potential reason for the occurrence of an internal fluidisation. In Alsaydalani (2010), a two-dimensional experimental study was conducted with the aid of the Particle Image Velocimetery technique. The sample granular bed was deposited in a seepage tank made of Perspex sheets, and the behaviour under the bed surface could be monitored.

From the results, Alsaydalani (2010) stated that the underlying mechanism is different from the classic backward erosion, or *piping* as is sometimes referred to. The backward erosion has been widely known in the field of civil engineering (Terzaghi, 1939; Fell et al., 2001; and Richards and Reddy, 2007). It is initiated at the exit point of seepage by

Darcy's flow, removing soil particles from the matrix. It progresses backwards, leading to the formation of a pipe. However, it is argued by Alsaydalani (2010) that internal fluidisation occurs due to a locally injected fluid, the soil particles lose stability and move within a localised zone along a pre-existing opening. In internal fluidisation, the fluid regime is non-laminar especially at the vicinity of the leak. The phenomenon is characterised by an uplift mechanism of the above grains and formation of an internal fluidised zone at the injected area, thereby the term 'internal fluidisation' was given. At the onset of fluidisation, the upward drag force overcomes the weight of a wedge-shaped uplifting zone, which is extending from the leaking area towards bed surface. Meanwhile, within the internal fluidised zone in the form of a cavity, particles are mobilised and moving with fluid. Such a phenomenon can be comparable to fluidisation in a tapered fluidised bed used in the chemical engineering (see Figure 2.1), where the Ergun (1952)'s flow equation through a packed bed is proved to be valid (Shi et al., 1984; Peng and Fan, 1997; and Gernon et al., 2008).

In addition, the localisation phenomenon was identified in the fluid flow (Alsaydalani, 2010), where pore pressure changes significantly near the source of flow but less so far from it. It was argued by Alsaydalani (2010) that the flows shall spread radially due to the local leakage. However, no direct supporting evidence was provided by his results.

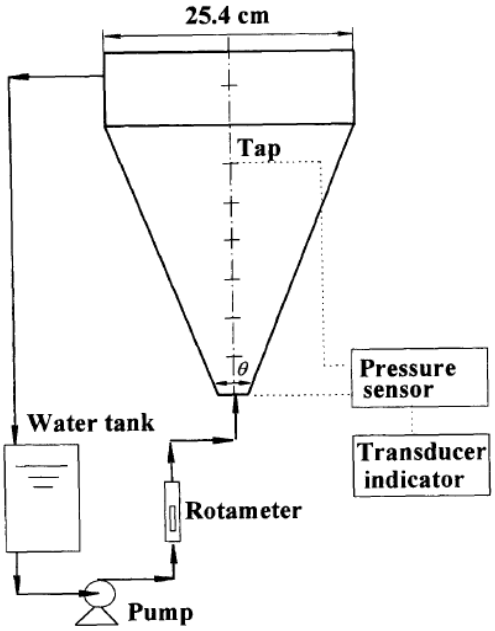

Figure 2.1 A simple skech of a typical tapered fluidised bed used in the chemical engineering (Peng and Fan, 1997)

Although Alsaydalani (2010) has achieved a successful investigation into the fundamentals underlying a granular bed subject to a local leakage under a two-dimensional condition, only limited information can be obtained from the experimental results. For example, the spatial distribution and time evolution of pore pressures has not been clearly revealed, though it may provide crucial information for a better understanding of the mechanism. Besides, a full knowledge of different bed regimes and post-fluidisation response, particularly how the cavity grows, still require more explorations.

However, laboratory tools lack of transparency and flexibility, and both the soil and flow information acquired is limited as well. Hence, a more promising tool is expected to easily provide an insight into samples, the monitoring of required data, and an extended application to repeatable samples under various conditions. For this reason, numerical simulations are conducted in this thesis. Since local large displacements may be involved in the leakage-soil interaction, numerical simulations using a continuum model based on the assumptions of a continuous, homogeneous, and isotropic material (Malvern, 1969) would encounter difficulties. Besides, a continuum model usually adopts a macroscopic constitutive relationship, which is applied to the particle assembly scale. This involves adopting many model parameters without clear physical meanings (Kishino, 1998), and considers implicitly the particle configuration in a granular material (Gong, 2008). Therefore, the Discrete Element Method (DEM) (Cundall and Strack, 1978), which performs analysis at the particle scale, is considered more suitable for simulating a granular soil in this thesis. Hence, a review of the DEM simulations in geotechnical application is presented in Section 2.3.

2.2.2 A conceptual model of soil behaviour when subject to a leaking fluid

When soil is subject to a leaking fluid, a number of actions are involved and their combined effect could be varying, demonstrating different soil behaviours. This sub-section presents a conceptual model of the soil behaviour from the point of view of the particle scale.

The movements of soil particles are controlled roughly by two groups of factors: activation and resistance. When soil is exposed to a leaking fluid, seepage force acts on the soil particles as a primary activation factor of particle movements. The seepage force is directly proportional to the hydraulic gradient under which a soil particle tends to move from an area with higher pressure towards that with lower pressure. On the other hand, however, the motion of a particle is resisted by a number of factors: particle weight, inter-particle friction, inter-particle cohesion, and self-healing potential. In general, a soil particle is not mobilised unless the seepage force is sufficiently high to overcome the particle self-weight, inter-particle friction and cohesion. Among those, inter-particle friction is mainly controlled by particle roughness and interlocking effect. Inter-particle cohesion is closely related to electrostatic force between particles, soil suction and dispersion. In the experimental work on clayey soils, Royal et al. (2008) found out that dispersive soils created larger cavities due to a leaking fluid than a non-dispersive soil did, although they had higher strength and particle quantities. This further suggests that inter-particle cohesion is one of the important factors affecting soil mobilisation.

For a soil with a low self-healing potential, small particles are firstly mobilised due to low weight, and start to move through the connected pores formed by larger-sized particles (Shire and O'Sullivan, 2013). During such a process, more and more particles

are removed from the soil, thus the original soil skeleton suffers changes and become unstable. This is referred to ‘internal erosion’ or ‘suffusion’ (Fell et al., 2001; and Shire and O’Sullivan, 2013). With more and more particles being removed, the pore size is increasing, and so is the local permeability. The unstable soil skeleton is no longer able to sustain the increased seepage force (due to the increase in permeability), and therefore leads to soil failures. From literatures, such a phenomenon has been regarded as a primary cause of many dam and embankment damages (Foster et al., 2000; Fell et al., 2001; and Zhou et al., 2012).

However, if the soil has a high self-healing potential, the mobilised small particles either block the pores, or cannot pass through the pores (Wan and Fell, 2008). Hence, they travel some distance and still remain in the soil, or stay at their original places. In such a case, soil is performing as integrity. When the upward seepage force applied to a bed of cohesionless material is equal to its bulk weight, ‘fluidisation’ was found to occur (Shi et al., 1984; Peng and Fan, 1997; and Alsaydalani, 2010). Figure 2.2 illustrates a conceptual model of particle movement and the resulting soil behaviours when subject to a leaking fluid.

Since quite a number of factors mentioned above are involved in the leakage-soil interaction, it is considered difficult to study all these factors in a single project. Hence, as an early attempt to understand its underlying mechanism, simplifications are adopted

in the models used in this thesis that the sample soil is non-dispersive, with low interlocking effect and high self-healing potential. Soil cohesion is only considered in Chapter 7, and its effect is simply modelled through particle surface energy. All these simplifications would definitely generate discrepancy from the real, yet however, the understanding of leakage-soil interaction can still be broadened, and its behaviour microscopically investigated. As for those factors that this thesis does not consider, further researches are expected and more sample models shall be used.

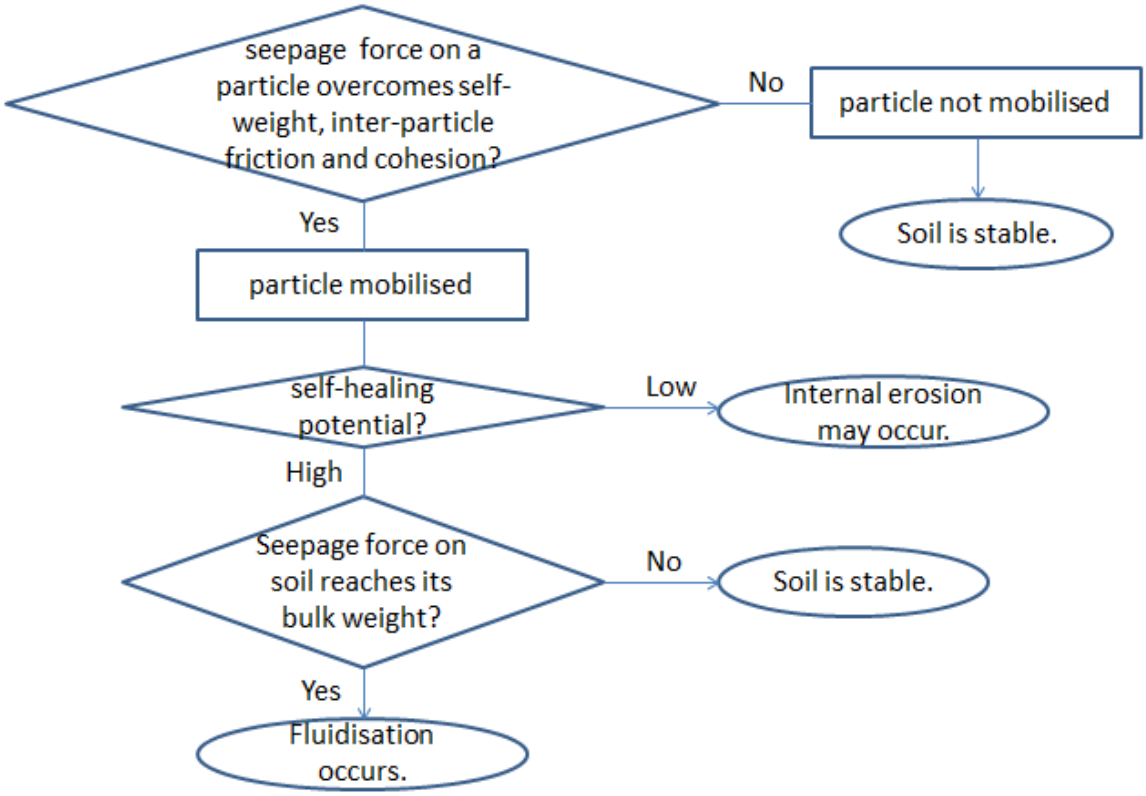

Figure 2.2 A conceptual model of particle movement and the resulting soil behaviours when subject to a leaking fluid

2.3 Review of DEM Simulations in Geotechnical Application

2.3.1 DEM simulations

DEM was initially proposed to deal with problems in rock mechanics (Cundall, 1971; and Cundall, 1974), and it has been increasingly used in the geotechnical field during recent decade (see e.g. O'Sullivan, 2011). In DEM, material is viewed as an assembly of discrete particles. Among literatures, two different algorithms are generally employed: hard-sphere and soft-sphere approaches (Duran, 2000). The former one tracks the particle motions based on momentum-conserving binary collisions, in which the particle-particle interactions are assumed to be impulsive, and considered one by one according to certain orders (Campbell and Brennen, 1985; and Hoomans et al., 1996). Although for a loose system, such models are regarded to be more efficient than the soft-sphere approach (Deen et al., 2007); its algorithm is not suitable for densely-packed systems, such as granular soils. This is because multiple collisions which occur at a same time cannot be easily taken into consideration. By contrast, in the soft-sphere approach, particle-particle interaction is viewed as a dynamic process, and a slight deformation in a particle is allowed during contacts. Contact forces are determined from particle deformation according to contact theories. And particle motion is computed by the Newton's second law. With the aid of the soft-sphere DEM, complete particle information can be obtained with the consideration of multiple collisions. Hence, this approach is adopted for simulating the intensive particle-particle

interactions in this thesis. It shall be noted that the term ‘DEM’ appeared hereinafter is used to refer to the soft-sphere approach. Its detailed algorithm and implementations are presented in Section 3.2.

From a large number of literatures on the DEM simulations, it is recognised that the soft-sphere DEM has been successfully applied to various geotechnical problems. Laboratory tests were reproduced using DEM to study the mechanical behaviour of cohesionless soils (Thornton, 2000; Zhang and Thornton, 2007; Gong, 2008 and Gong et al., 2012), or even fibre-reinforced sands (Maeda and Ibraim, 2008). Besides, attempts were made to capture the features of rock behaviour using DEM (Potynody and Cundall, 2004; and Huang and Detournay, 2008). In addition, behaviour of clayey soils was also studied using DEM with complex consideration of inter-particle forces (Anandarajah, 2000; Anandarajah, 2003; and Peron et al., 2009). Moreover, as for the special importance of pore pressure in a saturated soil, an explicit consideration of pore fluid should be needed, although without it, reasonable qualitative behaviour could be captured with the assumption of a constant volume (Ng and Dobry, 1994). It thereby generates an idea that DEM is coupled with fluid models, so that the drag force applied to the solid phase by pore fluid flows can be calculated simultaneously with fluid calculation cycle by cycle. With this idea, researchers have conducted simulations on various problems, including seepage through granular soils (El Shamy et al., 2002), undrained response (Bonilla, 2004; and Shafipour and Soroush, 2008), liquefaction

(Nakase et al., 1999; and Zeghal and El Shamy, 2008), and sand production (Preece et al., 1999; and O'Connor et al., 1997). For a more detailed review of the DEM simulations coupled with various fluid models, please refer to Section 2.4.

2.3.2 Development of DEM codes

With the increasing applications of DEM, the development of DEM computer code has progressed in different directions. In the late 1970s, the original two-dimensional DEM computer program *BALL* was developed in order to study the constitutive relations for a granular media (Cundall, 1978; Cundall and Strack, 1978). The code was validated by comparing the numerical outcome with the experimental observations (Cundall and Strack, 1979a; and Cundall and Strack, 1979b). Later, *BALL* was extended to a three-dimensional program *TRUBAL* (Cundall and Strack, 1979c). In those early versions of *BALL* and *TRUBAL*, circular discs or spherical particles were used as discrete elements, and a linear spring-dashpot contact model was adopted. Afterwards, elliptical particles were incorporated into *BALL*, so that some effects of particle shape on the behaviour of granular materials was explored (Ting et al., 1995). The simulation results demonstrated that elliptical particles provide more realistic macroscopic behaviour compared to circular discs, in both quantitative and qualitative perspectives. Similar conclusions were also drawn by Rothenburg and Bathurst (1992). Thereafter, a variety of particle shapes have been adopted, including assemblies of ellipsoids (Lin and

Ng, 1997; and Ng, 2001), super-quadric elements (Preece et al., 1999; and Han et al., 2007a), and clusters composed of simple-shaped particles (Jensen et al., 1999). Although it was pointed out the circular or spherical particles would underestimate the shear resistance of a granular material (Gong, 2008), in that particle interlock is hard to be considered, the implementation with irregular-shaped particles requires a lot more computational cost, in particular for contact detection. In this thesis, as fluidisation is the predominant phenomenon, the shear resistance contributed from particle interlock is identified to be less important. Therefore, only circular elements are adopted for the sake of simplicity for this first major attempt.

During the recent decades, a number of nonlinear contact models have also been incorporated into *TRUBAL*. The Hertz normal contact theory was adopted along with a simplified tangential contact theory (Johnson, 1985; Mindlin, 1949; and Cundall, 1988), and along with a complete tangential contact theory (Mindlin and Deresiewcz, 1953; and Thornton and Randall, 1988). In addition, an auto-adhesive contact theory (Thornton, 1991; Thornton and Yin, 1991; and Thornton and Ning, 1998) based on a well-known JKR model (Johnson et al., 1971) has been applied (Yang, 2009). With the aid of this model, the inter-particle adhesion force is computed, which is of key importance in the case where inter-particle adhesion force is comparable to particle weight. For this reason, this auto-adhesive contact model is also adopted in this thesis, so as to simulate the mechanical behaviour of a cohesive soil as an early attempt. The

detailed computations in this contact model are presented in Section 3.2.2. Moreover, among literatures, contact models for describing the apparent cohesion of unsaturated soils have also been proposed. In these models, efforts have been made to represent cohesive force, which is mainly due to capillary tension (Jiang et al., 2004; Richefeu et al., 2006; and El Shamy and Gröger, 2008). As in this thesis, only saturated soils are considered, no matric suction is accounted for in the numerical simulations and this should be considered in future work.

2.4 Review of DEM Simulation Coupled with Fluid Models

As mentioned in Section 2.3.1, DEM has been coupled with fluid models for the explicit consideration of pore fluid. Thereby the DEM program has been incorporated with various fluid methods. Among literatures, most early coupling programs were reported in which Darcy's law was adopted for the fluid flow calculations (Hakuno and Tarumi, 1988; O'Connor et al., 1997; and Nakase et al., 1999). Later on, the DEM program was developed to include solutions to the Navier-Stokes equations (El Shamy et al., 2002; Kafui et al., 2002; and Suzuki et al., 2007). In the coupling programs mentioned above, the computational cell used for fluid calculation is usually larger than an individual particle, and the fluid information within each cell is adopted as a local averaged value. By contrast, small-sized fluid grids are adopted in the Lattice Boltzmann Method (LBM) (Chen and Doolen, 1998). It has been coupled with DEM in

order to achieve detailed description of fluid-particle interaction (Cook et al., 2004; Feng et al., 2007; and Mansouri et al., 2009). Besides, a mesh-free fluid method, the Smoothed Particle Hydrodynamics (SPH) (Gingold and Monaghan, 1977), was also coupled with DEM to facilitate simulations of fluid flow through granular media (Li et al., 2007). More detailed reviews of the coupling techniques employed by those programs are given in the following sub-sections, in an effort to identify an appropriate technique, by which the behaviour of large displacements in soil, the localisation phenomenon in flow, along with the interactions between particle and fluid phases can be described.

2.4.1 DEM coupled with Darcy fluid flow (DFF)

When DEM is coupled with a fluid model, drag force obtained from the fluid calculation is usually added to the total force acted on an individual particle, so that particle motion can be further determined. On the other hand, the effect of particle motion on the fluid flow is also taken into account in each calculation cycle. This can be accomplished by modifying permeability according to updated particle locations and/or adding a semi-empirical drag force term in the fluid equations, or alternatively, expressing the local flows with explicit consideration of the solid phase. From literature, several categories of fluid models have generally been identified, including the Darcy Fluid Flow (DFF) model; the Computational Fluid Dynamics (CFD) model; the model

by LBM; and the mesh-free model by SPH. Among the above categories, the DFF model is regarded the simplest one, and hence has been widely used from an early stage.

A decade ago, Preece et al. (1999) and Jensen and Preece (2000) successfully employed a two-dimensional coupled DEM-DFF technique to simulate sand production phenomenon in oil wells. In their simulation, fluid flows were calculated from continuity equation along with Darcy's law, of which the solutions were pressure functions:

$$k_x \frac{\partial^2 p}{\partial x} + k_y \frac{\partial^2 p}{\partial y} = 0 \tag{2.1}$$

Eqn.(2.1) is the notable two-dimensional Laplace equation and was solved by the finite element techniques. In Eqn.(2.1), p is the pressure at each finite element node, and k_x and k_y are the permeabilities along the x- and y- directions, respectively. Integration of fluid pressure on each particle was then carried out to calculate fluid-induced force. By summing up body force, contact force and the fluid-induced force, the resultant force exerted on a particle was obtained. Thereafter, the particle locations were updated through DEM calculations. According to the updated particle locations, a new permeability value was calculated from volume fraction and ready for solving Eqn.(2.1) at the next calculation cycle. Although this technique is easy to be implemented, the fluid flow is implicitly solved without considering the time-dependent pore volume

changes which also affect pore pressure evolution.

In contrast, another coupled DEM-DFF technique has been developed to provide a time-dependent solution to fluid flows. Such a technique is mostly applied to granular media under undrained conditions. Pore pressure generation due to pore volume changes was firstly accounted for by Hakuno and Tarumi (1988) when they treated fluid as an elastic medium. And the dissipation of pore pressures was determined by Darcy's law. It was also assumed that an instant equilibrium state was achieved within every calculation cycle. Although the similar idea was adopted in Bonilla (2004), the instant equilibrium assumption was abandoned, and the pore pressure evolution is viewed as a totally dynamic process, which gave more realistic solutions.

Unlike the above works that pore pressures were considered at the pore scale (see Figure 2.3(a)), Nakase et al. (1999) adopted a simplified determination of pore pressures at the cell scale (see Figure 2.3(b)). This avoided tedious identification of individual pores within each calculation cycle. In their work, the fluid cell was chosen to be larger than the particle size. The pore pressure generation and dissipation were computed using the cell-averaged values, and a single fluid-induced force was determined by the pressure gradients and applied to all particles in a particular cell. Meguro and Ravichandran (2000) applied this technique to study the mechanism of liquefaction. Good qualitative results were obtained from the three-dimensional simulations. More

recently, the semi-empirical Ergun's equation was employed for calculating the drag force (Shafipour and Soroush, 2008; and Zeghal and El Shamy, 2008), in order to investigate the undrained behaviour of granular media and the liquefaction of saturated soils.

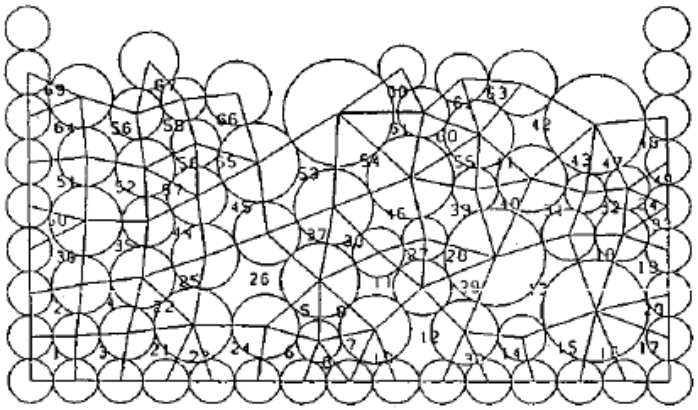

(a) at the pore scale (Hakuno and Tarumi, 1988)

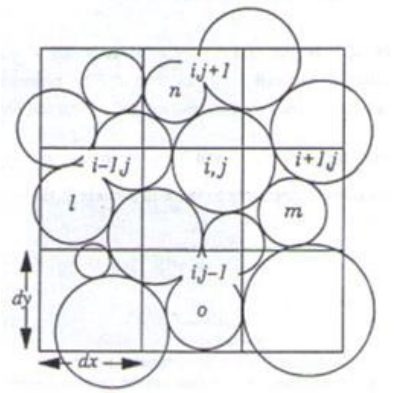

(b) at the cell scale (Nakase et al.,1999)

Figure 2.3 Basic scales adopted for fluid calculations in DEM-DFF

Although the Darcy fluid flow has relatively simple formation so that the computational cost can be kept low, it is not applicable to flows with high Reynolds number. Moreover,

it fails to give a good description of the physics where particles are dragged away or transported by fluid (Jensen and Preece, 2000), such as in a fluidisation phenomenon.

2.4.2 DEM coupled with computational fluid dynamics (CFD)

Compared to the DFF model, the Navier-Stokes equations provide a more generalised description of fluid flows, and the Computational Fluid Dynamics (CFD) is commonly understood as the art of solving the Navier-Stokes equations computationally. The idea of combining CFD with DEM was pioneered by Tsuji et al. (1993), when they performed two-dimensional numerical simulations of gas-fluidised beds. The fluid domain was divided into large-sized cells, and the standard Navier-Stokes equations were transferred to a cell-averaged form:

$$\begin{aligned} &\frac{\partial \varepsilon}{\partial t} + \nabla \cdot (\varepsilon \mathbf{u}) = 0 \\ &\nabla \cdot (\varepsilon \mathbf{u}\mathbf{u}) = -\frac{\varepsilon}{\rho_f} \nabla p + f_s \end{aligned} \tag{2.2}$$

where p and $\mathbf{u}$ are the cell-averaged fluid pressure and velocity, respectively. ρ_f is the fluid density, and ε was the volume fraction calculated for each cell. f_s represents the effect of particle motion on fluid flow, which is related to particle relative velocities. Similar to the coupled DEM-DFF technique, in DEM-CFD, the DEM calculations updated particle motion and locations, allowing the volume fraction of each cell to be acquired. With the particle velocity and volume fraction obtained, the cell-averaged Navier-Stokes equations were solved, yielding pressure and velocity fields for the fluid

phase. Drag force was then calculated through semi-empirical relations, and added to the total force applied to individual particles for the next cycle of DEM calculation.

Thereafter, the work by Tsuji et al. (1993) was extended to three dimensions, and a good agreement between numerical and experimental results was obtained (Kawaguchi et al., 1998). From then on, the coupled DEM-CFD technique has been widely applied, for example, to seepage flows (El Shamy et al., 2002; and Suzuki et al., 2007) and fluidised beds (Xu and Yu, 1997; Kafui et al., 2002; Feng and Yu, 2006; and Zhao et al., 2008). A useful review was given by Zhu et al. (2007 and 2008). From literature, however, most fluidised beds modelled have been the uniform ones, where the fluid is injected uniformly at the bed base. It is recognised that it would not be straight forward to apply DEM-CFD to a locally injected fluid, such as a pipe leakage. This is mainly because the adopted coarse cells are difficult to define localised boundary settings, unless mesh refinement is involved at the boundaries. Furthermore, there has been an argument on the semi-empirical relations for calculating drag force, as the relations were developed from the drag force equation for an isolated particle without full consideration of the presence of surrounding particles (Zhu et al., 2007). In addition, for the cases where the fluid-particle interactions are intensive and crucial, DEM-CFD is intrinsically difficult to trace the fluid motion around each particle, thus provides an ambiguous description of fluid-particle interactions, unless very fine grids are used.

On the other hand, a fine-grid CFD, also known as the Direct Numerical Simulation (DNS), has been coupled with DEM for simulating small-scale fluid-particle systems (Hu, 1996; and Pan et al., 2002). However, the computational cost would be undesirably increased if a large-scale system needs to be modelled. Therefore, when dealing with the interaction between a local leakage and surrounding soils, an alternative numerical tool should be employed.

2.4.3 DEM coupled with lattice Boltzmann method (LBM)

The Lattice Boltzmann Method (LBM) originated from the late 1980s (McNamara and Zanetti, 1988). It has been regarded as an alternative to the conventional macroscopic fluid models (Brenner 2004), and used for a wide range of applications, including particulate suspensions (Ladd and Verberg, 2001), multiphase flows (Premnath et al., 2005), energy transport problems (Chen et al., 1995), and turbulent flows (Hou et al., 1996).

Unlike DFF and CFD, LBM is based on microscopic kinetic models. It is derived from the Boltzmann equation, which is a relatively rigorous description of the transport phenomena. LBM is originated from the idea that the Boltzmann equation is discretised in space, time, and velocity field. Such an idea gave birth to a numerical algorithm known as the Lattice Gas Automata (LGA) (Hardy et al., 1976), which was the

precursor to LBM. After one decade, the macroscopic Navier-Stokes equation was successfully recovered from LGA with a symmetrical lattice (Frisch et al., 1986). Although this algorithm was promising, it may be subject to statistical noise, resulting from a set of Boolean variables used. To avoid the noisy nature, LBM replaced the particle occupation variables (Boolean variables) by density distribution functions (McNamara and Zanetti, 1988), which were real numbers between 0 and 1. Thereafter, simplification and enhancement have been made to LBM implementations (Higuera and Jiménez, 1989; and Higuera et al., 1989). Among those, the BGK model proposed by Qian (1990) and Chen et al. (1991) has been regarded very efficient and flexible (Chen and Doolen, 1998), due to a simple linear collision operator adopted. Therefore, this model has been widely employed in the LBM simulations since its origin, as recognised from literature.

In LBM, the fluid domain is usually divided into a regular lattice. Fluid is considered as packets of micro-particles residing on the lattice nodes. Those fluid particles are assumed to move with prescribed discrete velocities in every calculation cycle, so that configuration of fluid particles varies cycle by cycle, leading to a changing flow field. Due to the microscopic nature of LBM theory, a localised flow field can be simulated with fine resolution. Moreover, as pointed out by Han et al. (2007b), LBM prevails over the conventional macroscopic fluid models, in that it avoids solving the Navier-Stokes equations but involves only simple local operations. This advantage leads to a higher

efficiency of LBM. For instance, when simulating a homogeneous and isotropic turbulence, it was noted that more than half of CPU time could be saved by LBM compared with CFD when a same grid size is adopted (Satofuka and Nishioka, 1999). Due to this advantage, a detailed description of fluid-particle interactions can be efficiently provided when LBM coupled with DEM, with large-sized solid particles merged into the fine lattice. Hence, it is recognised that the coupled DEM-LBM technique would be promising for this thesis, as the localisation phenomenon along with the intensive fluid-particle interactions can be simulated. A more detailed review of DEM-LBM applications is therefore presented in Section 2.5.

2.4.4 DEM coupled with smoothed particle hydrodynamics (SPH)

Among literatures, an alternative fluid model that has been coupled with DEM is the Smoothed Particle Hydrodynamics (SPH) model. SPH is one of the Mesh-free Particle Methods (Liu and Liu, 2003), in which the Eulerian grid is not adopted. SPH treats a fluid system as a finite set of particles, and each particle represents a parcel of fluid domain. Fluid information is carried by those fluid particles. The Navier-Stokes equations are rewritten by the SPH particle approximation (Bui et al., 2007), which is given through an interpolation function at a particular fluid particle. Due to its Lagrangian nature, SPH is regarded advantageous over the Eulerian models for identifying the fluid phase and to apply complicated geometries (Crespo, 2008). For this

reason, among literatures, SPH has been coupled with DEM as a favourable tool to simulate the solid-liquid mixtures, such as fluid flows through granular materials (Potapov et al., 2001; and Li et al., 2007).

However, as stated in Crespo (2008), computations using SPH are typically slower compared with other grid-based models. In addition, Li (2012) has pointed out that the macroscopic viscosity is difficult to be applied in SPH due to the discrete description of fluid. Besides, the implementation of turbulence modelling in SPH is also complicated, although attempts have been made by Rogers and Dalrymple (2004). Therefore, compared with DEM-LBM, the coupled DEM-SPH technique is considered uneconomical for simulating the leakage-soil interaction.

2.5 Review of DEM-LBM Simulations

As stated in Section 2.4.3, it has been identified that the coupled DEM-LBM technique would be promising to efficiently describe the physical behaviour of a localised flow and intensive fluid-particle interactions. This technique was firstly proposed by Cook et al. (2000), when they conducted simulations on particle-laden fluids. Validations were carried out using only a few discs and n-sided polygons in sedimentation tests, and the correct phenomenological behaviour was obtained. Further, a quantitative comparison with the analytical solution was performed by simulating a

cylindrical Couette flow (Cook et al., 2004), which demonstrated the capability of this technique in accurately computing fluid flow and particle forcing.

More recently, another group of researchers (Han et al., 2007b; and Feng et al., 2007) incorporated a simple Large Eddy Simulation (LES) model into DEM-LBM, in order to achieve turbulence modelling. A larger number of moving particles were used to simulate a two-dimensional transport problem. It was found that the coupled technique with LES turbulence model was robust up to a Reynolds number of around 56,000. Their work was then extended to three dimensions, and validations were conducted against experimental data for a vacuum dredging system (Feng et al., 2010). Good overall correspondence was identified from the results. Besides, Mansouri et al. (2009) applied DEM-LBM to a three-dimensional model of sand boiling, and the critical hydraulic gradient measured from numerical test was found to be close to that given by classical soil mechanics. Moreover, the coupled technique was further used to obtain permeability of a cemented granular material (Mansouri et al., 2010), again, the numerical results agreed well with the existing classical solutions.

In the fluid-particle systems modelled by DEM-LBM, the interactions between the solid and fluid phases can be treated well with appropriate boundary conditions. From literature, a widely-used boundary condition in LBM is the bounce-back rule (Wolfram, 1986), because it is easy to be implemented, especially for boundaries with arbitrary

shapes (Han et al., 2007b). However, the bounce-back rule is not suitable for moving boundaries (Noble et al., 1995), such as moving solid particles. In order to overcome such a drawback, Ladd (1994) suggested a modified version of the bounce-back rule, in which a term relevant to the velocity of solid particle was included. The fluid-induced force on the solid particle was calculated according to the collision rule. Nevertheless, undesirable oscillation was observed when the solid particle was moving with a relatively large velocity (Ladd and Verberg, 2001), and this was mainly attributed to the definition of boundary nodes which kept changing in an 'on-off' fashion (Han et al., 2007b). In an effort to avoid the oscillation, researchers adopted an Immersed Moving Boundary (IMB) scheme for the inter-phase treatment (Noble and Torczynski, 1998). Through a local solid/fluid ratio, the standard lattice Boltzmann equation was modified, and a more precise lattice representation of solid particles was obtained (Feng et al., 2007). Hence, it is possible to acquire a smooth solution to the local flow and fluid-induced force. Since in the leakage-soil interaction, soil particles could undergo quick movements with the leaking fluid, the IMB scheme is adopted in this thesis. The detailed implementation is presented in Section 3.4.1.

2.6 Summary

Although the leakage-induced accidents have been reported all over the world, where large deformation of surrounding soils are caused by leaking fluid from a buried

pipe, not many literatures have been published regarding its mechanism. Laboratory works have identified three failure modes in soils when subjected to a local leakage, which are dependent on pressure settings and flow rate. A two-dimensional experimental study has recognised that internal fluidisation is the underlying mechanism, which was characterised by pore pressure build-up, an uplift mechanism of the above grains, and an internal fluidised zone in the form of a cavity. In addition, the localisation nature in the flow was also found from the experimental results. However, due to lack of transparency and limited ability of data acquisition, numerical simulations are expected in order to achieve a deeper understanding of the problem, including the spatial distribution and time evolution of pore pressures, a full knowledge of different bed regimes, and the post-fluidisation response.

Compared with the conventional continuum models, the Discrete Element Method (DEM) is more promising to analyse the behaviour of a granular material and to some extent, particles with cohesion, especially those involving local large displacements. With the aid of the soft-sphere DEM, complete information can be obtained for each particle with consideration of multiple collisions. From literature, it is recognised that the soft-sphere DEM has been successfully applied to various geotechnical applications, including reproducing laboratory tests, rock mechanics problems, and physical behaviour of clayey soils.

Since the origin of DEM, many different developments have been made on the DEM programs. Although irregular-shaped particles have been used to consider the interlock effects of granular soils, the implementation costs more compared with circular or spherical particles. In this thesis, as fluidisation acts as the predominant phenomenon, the shear resistance contributed from particle interlock is identified to be less important. Therefore, only circular particles are adopted for the sake of simplicity as a first major attempt. From literature, it can be seen that different contact models have also been employed in the development of DEM code. Among those, an auto-adhesive contact theory based on the JKR model is chosen as a promising candidate in this thesis, which can be adopted to compute the inter-particle adhesion force, as an early attempt to explore the mechanical effect of soil cohesion.

In order to explicitly consider the pore fluid, DEM has been coupled with various fluid models. Among literatures, several categories of the fluid models can be identified: the Darcy Fluid Flow (DFF) model; the Computational Fluid Dynamics (CFD) model; the model by the Lattice Boltzmann Method (LBM); and the mesh-free model by the Smoothed Particle Hydrodynamics (SPH). When DEM coupled with DFF or CFD, the fluid domain is usually divided into coarse cells, of which the size is larger than an individual particle. The fluid equations (i.e. the Laplace equation or the Navier-Stokes equations) are computationally solved at the cell level, with the pore volume fraction and permeability updated from DEM solutions. The drag force exerted on an individual

particle is thereby calculated from semi-empirical relations. However, DEM-DFF is not suitable for the modelling of fluid flows with high Reynolds number. Moreover, due to the coarse grids adopted, it is intrinsically difficult for both DEM-DFF and DEM-CFD to trace the fluid motion around each particle, thus provides an unsatisfactory description of fluid-particle interactions.

The coupled DEM-SPH has been applied to the solid-liquid mixtures, such as fluid flows through granular materials. Although SPH is regarded advantageous over most Eulerian models to identify the fluid phase and to apply complicated geometries, it is computationally more expensive than grid-based models. In addition, it is difficult to apply the macroscopic viscosity and turbulence implementations in SPH due to its discrete description of fluid. Therefore, DEM-SPH is considered not suitable for simulating the leakage-soil interaction, especially in the case that turbulence phenomenon is involved at the vicinity of the leak.

From literature, DEM-LBM has been identified as an alternative technique for simulating fluid-particle systems. Unlike DFF, CFD and SPH, LBM is based on the microscopic kinetic models. With the same grid size being adopted, it has been recognised that LBM is of higher efficiency compared with the conventional CFD method. Furthermore, due to its microscopic nature, a detailed description of fluid-particle interactions can be efficiently obtained when coupled with DEM, with large-sized solid particles merged

into the fine lattice. The Immersed Moving Boundary (IMB) scheme was proposed for the inter-phase treatment in DEM-LBM. Modified by a local solid/fluid ratio, LBM is capable of providing a more precise lattice representation of solid particles. Researchers have demonstrated that the DEM-LBM results agree well with experimental data and analytical solutions qualitatively and quantitatively. Moreover, incorporated with the Large Eddy Simulation (LES), DEM-LBM is capable to achieve robust turbulence modelling. For the above reasons, it is recognised that the coupled DEM-LBM technique would be promising for this thesis, in which the localisation and turbulence phenomenon, along with the intensive fluid-particle interactions are expected to be simulated efficiently.

CHAPTER 3: THE COUPLED DEM-LBM TECHNIQUE

3.1 Introduction

Although the coupled DEM-LBM technique is regarded promising, no open source code has been found so far. A two-dimensional DEM-LBM code, named *FPS-BHAM*, is therefore developed in order to carry out numerical simulations in this study. In *FPS-BHAM*, DEM considers the soil as an assembly of circular particles; and LBM is used for the modelling of fluid flow. The Immersed Moving Boundary (IMB) scheme, as stated in Section 2.4, is adopted to resolve the interactions between fluid and soil particles. The relevant computational algorithms and implementations in *FPS-BHAM* are outlined in Sections 3.2-3.4. In Section 3.5, the flow chart of complete calculation process is given to show how a DEM-LBM simulation runs for this thesis. Finally, a summary of the chapter is given in Section 3.6.

3.2 Soft-Sphere DEM

3.2.1 Computational algorithm

The soft-sphere DEM, which is adopted in this thesis, is a Lagrangian method which performs analysis at the particle level. Between any two particles in contact, a slight overlap is allowed. The contact is viewed as a dynamic process in which contact forces accumulate or dissipate over time. Contact forces can be subsequently obtained through

the deformation history at the contact. The motion of a single particle is governed by the Newton's second law in the form of the following equations,

$$m\frac{d^2\mathbf{x}}{dt^2} = \mathbf{F}_c + \mathbf{F}_b + \mathbf{F}_h \tag{3.1}$$

$$I\frac{d\boldsymbol{\omega}}{dt} = \mathbf{T}_c + \mathbf{T}_h \tag{3.2}$$

where $\mathbf{F}_c$ denotes the total contact force, calculated by summing up all the contact forces applied to an individual particle. $\mathbf{T}_c$ is the torque generated by the contact force. $\mathbf{F}_b$ represents the body force, namely, the submerged gravity in this thesis. $\mathbf{F}_h$ and $\mathbf{T}_h$ refer to the force and torque induced by fluid flows, respectively. Their values are obtained through the fluid-particle two-way coupling (see Section 3.4.1). Besides, m, $\frac{d^2\mathbf{x}}{dt^2}$, I, and $\frac{d\boldsymbol{\omega}}{dt}$ represent mass, translational acceleration, moment of inertia, and angular acceleration of particle, respectively.

In DEM, a time step has to be chosen sufficiently small so that the propagation of the disturbances cannot go further beyond the neighbouring particles, and therefore, the particle velocities and accelerations are assumed to be constant within a single time step (Cundall and Strack, 1978). Thus, with the accelerations computed from Eqns.(3.1) and (3.2) for each particle at each time step, particle velocities are integrated using a central difference scheme, and the locations are updated as below,

$$\mathbf{x}^t = \mathbf{x}^{t-\Delta t_{DEM}} + \Delta t_{DEM} \cdot [\mathbf{v}^t \cdot (1 - \frac{c}{m}\frac{\Delta t_{DEM}}{2}) + \mathbf{F}^t \cdot \frac{\Delta t_{DEM}}{m}] / (1 + \frac{c}{m}\frac{\Delta t_{DEM}}{2}) \tag{3.3}$$

$$\boldsymbol{\theta}^{t} = \boldsymbol{\theta}^{t-\Delta t_{DEM}} + \Delta t_{DEM} \cdot [\boldsymbol{\omega}^{t} \cdot (1 - \frac{c'}{I}\frac{\Delta t_{DEM}}{2}) + \mathbf{T}^{t} \cdot \frac{\Delta t_{DEM}}{I}] / (1 + \frac{c'}{I}\frac{\Delta t_{DEM}}{2}) \quad (3.4)$$

where $\mathbf{x}$ and $\boldsymbol{\theta}$ represent components of location and angular rotation of a particle. $\mathbf{F}$ and $\mathbf{T}$ are the total force and torque applied to the particle. c and c' are the global damping which are taken to be proportional to mass and inertia, respectively. Δt_{DEM} is the DEM time step, and its choice is explained in Section 3.4.2. The superscripts t and $t - \Delta t_{DEM}$ represent the quantities at the current and previous time steps, respectively.

The normal and tangential components of the total contact force $\mathbf{F}_c$ can be determined by,

$$\mathbf{F}_n^t = \mathbf{F}_n^{t-\Delta t_{DEM}} + k_n \Delta \boldsymbol{\alpha} \quad , \quad \mathbf{F}_t^t = \mathbf{F}_t^{t-\Delta t_{DEM}} + k_t \Delta \boldsymbol{\delta} \quad (3.5)$$

where $\Delta\boldsymbol{\alpha}$ and $\Delta\boldsymbol{\delta}$ are the relative normal and tangential displacement increments within a DEM calculation cycle. k_n and k_t are the normal and tangential contact stiffnesses, which are computed by algorithms based on contact theories (see Section 3.2.2).

3.2.2 Contact force calculations

The contact force calculations from a well-established code *TRUBAL*, which is based on the contact theories stated in Thornton (1991), are directly transferred into *FPS-BHAM* for this thesis. This sub-section outlines the main calculation procedure in the code. For

the ease of explanation, some basic variables and their expressions are firstly defined in the following section.

As for two circular particles *A* and *B* in contact, their radii are denoted as R_A and R_B, masses as m_A and m_B, Young's modulus as E_A and E_B, shear modulus as G_A and G_B, and Poisson's ratios as ν_A and ν_B. The effective contact radius R^* is obtained from, (see e.g. Yang, 2009)

$$\frac{1}{R^*} = \frac{1}{R_A} + \frac{1}{R_B} \tag{3.6}$$

The effective mass m^* is obtained from,

$$\frac{1}{m^*} = \frac{1}{m_A} + \frac{1}{m_B} \tag{3.7}$$

The effective contact Young's modulus E^* is obtained from,

$$\frac{1}{E^*} = \frac{1-\nu_A^{\,2}}{E_A} + \frac{1-\nu_B^{\,2}}{E_B} \tag{3.8}$$

The effective contact shear modulus G^* is obtained from,

$$\frac{1}{G^*} = \frac{2-\nu_A}{G_A} + \frac{2-\nu_B}{G_B} \tag{3.9}$$

The relative approach between the two particles in contact (Figure 3.1) is expressed as

$$\boldsymbol{\alpha} = (R_A + R_B - D)\cdot \mathbf{n} \tag{3.10}$$

$$\alpha = R_A + R_B - D \tag{3.11}$$

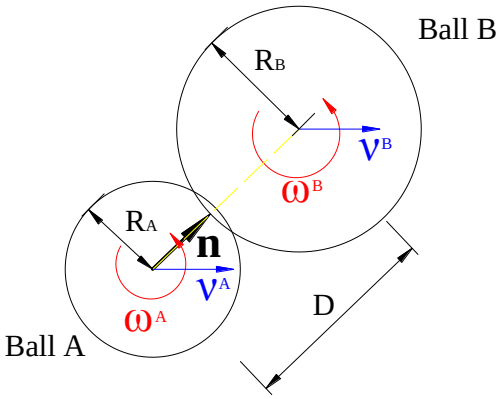

Figure 3.1 Two particles in contact

where D is the centre-to-centre distance and $\mathbf{n}$ is the unit vector pointing from centre of A to centre of B. The relative normal and tangential displacement increments are obtained from,

$$\Delta\alpha = \left(\mathbf{v}^B - \mathbf{v}^A\right)\cdot\mathbf{n}\cdot\Delta t_{DEM} \tag{3.12}$$

$$\Delta\boldsymbol{\delta} = \left(\mathbf{v}^B - \mathbf{v}^A\right)\Delta t_{DEM} - \Delta\alpha\mathbf{n} - \left(\boldsymbol{\omega}^A\times\mathbf{n}\right)R_A\Delta t_{DEM} - \left(\boldsymbol{\omega}^B\times\mathbf{n}\right)R_B\Delta t_{DEM} \tag{3.13}$$

Hence, the tangential displacement is calculated by,

$$\boldsymbol{\delta}^{t+\Delta t} = \boldsymbol{\delta}^t + \Delta\boldsymbol{\delta} \tag{3.14}$$

During each DEM time step, the tangential force and displacement are re-orientated due to the rotation of the contact plane. The variables are adjusted as below,

$$\begin{aligned}\mathbf{F}_t^{re\text{-}oriented} &= \boldsymbol{\Omega}\times\mathbf{F}_t\\ \boldsymbol{\delta}^{re-orientated} &= \boldsymbol{\Omega}\times\boldsymbol{\delta}^{old}\end{aligned} \tag{3.15}$$

where $\boldsymbol{\Omega}$ is the rotation of the contact plane given by,

$$\boldsymbol{\Omega} = \frac{\mathbf{n}}{D}\times\left((\mathbf{v}^B - \mathbf{v}^A)\Delta t_{DEM} - \Delta\alpha\mathbf{n}\right) \tag{3.16}$$

If the resultant tangential force satisfies the sliding criterion, sliding is assumed to occur and the tangential force is reset to the limiting value $\mu \cdot F_n$ (μ is the inter-particle friction coefficient).

The Hertz theory (see Johnson, 1985) is used to determine the normal contact stiffness,

$$k_n = 2E^* a_1 \tag{3.17}$$

where a_1 is the radius of the contact area calculated as follow,

$$a_1 = \sqrt{\alpha R^*} \tag{3.18}$$

The tangential contact stiffness is determined by Thornton and Randall (1988) based on the theory of Mindlin and Deresiewicz (1953). By adopting an incremental approach, k_t can be calculated using the newly updated F_n and a_1. The expression for k_t is shown as follows (Thornton and Yin, 1991),

$$k_t = 8G^* a_1 \theta \pm \mu(1-\theta)\frac{\Delta F_n}{\Delta \delta} \tag{3.19}$$

$$\theta = \left(1 - \frac{\left(F_t + \mu \Delta F_n\right)}{\mu F_n}\right)^{1/3} \qquad \Delta\delta > 0 \quad (loading) \tag{3.20}$$

$$\theta = \left(1 - \frac{\left(F_t^* - F_t + 2\mu \Delta F_n\right)}{2\mu F_n}\right)^{1/3} \qquad \Delta\delta < 0 \quad (unloading) \tag{3.21}$$

$$\theta = \left(1 - \frac{\left(F_t - F_t^{**} + 2\mu \Delta F_n\right)}{2\mu F_n}\right)^{1/3} \qquad \Delta\delta > 0 \quad (reloading) \tag{3.22}$$

and the negative sign in Eqn.(3.19) is only taken during unloading. The forces F_t^* and F_t^{**} define the load reversal points and need to be continuously updated,

$$F_t^* = F_t^* + \mu\Delta F_n \tag{3.23}$$

$$F_t^{**} = F_t^{**} - \mu\Delta F_n \tag{3.24}$$

If $|\Delta\delta| < \frac{\mu\Delta F_n}{8G^* a_1}$ with $\Delta F_n > 0$, let θ=1 until the condition $\sum 8G^* a_1 \Delta\delta > \mu\sum\Delta F_n$ is satisfied.

In order to account for inter-particle adhesion, the JKR model (Johnson et al., 1971) has been incorporated into the Hertz model to determine the normal contact stiffness (Thornton and Yin, 1991),

$$k_n = 2E^* a_2 \left(\frac{3 - 3\sqrt{\frac{a_3^3}{a_2^3}}}{3 - \sqrt{\frac{a_3^3}{a_2^3}}} \right) \tag{3.25}$$

where

$$a_2 = \left(\frac{3R^* F'}{4E^*} \right)^{1/3} \tag{3.26}$$

$$a_3 = \left(\frac{3R^* F_c}{4E^*} \right)^{1/3} \tag{3.27}$$

and F' is regarded to be the effective normal force,

$$F' = F_n + 2F_c \pm \sqrt{4F_n F_c + 4F_c^2} \tag{3.28}$$

If the particles are leaving each other, the negative sign is taken in Eqn.(3.28). F_c is the so called 'pull-off' force indicating the maximum tensile force required to separate two adhesive particles in contact. It is given by,

$$F_c = 3.0\pi\Gamma R^* \tag{3.29}$$

where Γ is the surface energy of each solid particle in contact. Accordingly, in order to examine the effect of particle surface energy on the bed response to the pipe leakage (see Section 7.4), values of Γ were selected according to the following relationship,

$$F_c = K\overline{mg} \tag{3.30}$$

where K indicates the ratio of inter-particle adhesion force to average particle weight.

In the presence of tangential interactions, it is assumed that a peeling mechanism takes place initially when a tangential force is applied (Thornton, 1991). During this peeling process, the radius of the contact area reduces to

$$a_4 = \left(\frac{3R^*}{4E^*} \left(F_n + 2F_c \pm \sqrt{4F_nF_c + 4F_c^2 - \frac{F_t^2 E^*}{4G^*}} \right) \right)^{1/3} \tag{3.31}$$

If the particles are leaving each other, the negative sign is taken in Eqn.(3.31). The corresponding tangential stiffness is given by

$$k_t = 8G^* a_4 \tag{3.32}$$

The peeling process terminates if the tangential force reaches a critical value of

$$F_{tc} = 4\left(\frac{G^*}{E^*}\left(F_n F_c + F_c^2\right)\right)^{1/2} \tag{3.33}$$

After the tangential force reaches to its critical value, sliding immediately happens if F_{tc} is greater than the sliding force F_{slc},

$$F_{slc} = \mu F'\left(\frac{2F' + F_n}{3F'}\right)^{3/2} \quad (F_n < -0.3F_c) \tag{3.34}$$

$$F_{slc} = \mu\left(F_n + 2F_c\right) \quad (F_n \geq -0.3F_c) \tag{3.35}$$

and the tangential force is then reset to F_{slc}. Otherwise, it undergoes a smooth transition to sliding. During this transition process, the radius of the contact area is given by,

$$a_5 = \left(\frac{3R^*}{4E^*}\left(F_n + 2F_c\right)\right)^{1/3} \tag{3.36}$$

and the corresponding tangential stiffness is calculated by Eqns.(3.19)-(3.22) with F_n replaced by $F_n + 2F_c$, and a_1 replaced by a_5.

In order to account for the energy dissipation due to elastic wave propagation, dashpot forces are introduced and added to the resultant force on a particle. The normal and tangential components of the dashpot force are given by (see e.g. Yang, 2009),

$$F_{nd} = 2\beta\sqrt{m^* k_n}\alpha / \Delta t_{DEM} \tag{3.37}$$

$$F_{td} = 2\beta\sqrt{m^* k_t}\delta / \Delta t_{DEM} \tag{3.38}$$

where β is a contact damping factor.

3.3 LBM for Fluid Flow Modelling

3.3.1 Implementations

In LBM, the fluid domain is divided into a square lattice with unity spacing. Fluid is assumed as packets of micro-particles residing on each lattice node. The D2Q9 model (Feng et al., 2007) is adopted in this thesis, in which the velocity field is discretised into nine prescribed vectors (see Figure 3.2). In a unity time step, fluid particles are allowed either to remain at their current locations (which is referred to the zero velocity $\mathbf{e}_0$), or to travel to their adjacent nodes with velocities $\mathbf{e}_i \quad (i = 1,...8)$.

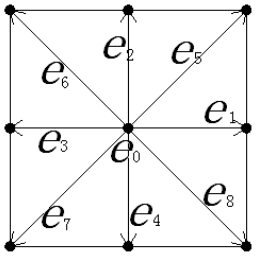

Figure 3.2 Nine prescribed velocities in a D2Q9 model

As demonstrated in Figure 3.2, the prescribed velocities in a D2Q9 model are defined as,

$$\begin{aligned} &\mathbf{e}_0 = (0,0); \\ &\mathbf{e}_i = C(\cos\{\pi(i-1)/2\}, \sin\{\pi(i-1)/2\}) \quad (i = 1,2,3,4); \\ &\mathbf{e}_i = \sqrt{2}C(\cos\{\pi(2i-9)/4\}, \sin\{\pi(2i-9)/4\}) \quad (i = 5,6,7,8); \end{aligned} \tag{3.39}$$

where C refers to the lattice speed, which is defined as the ratio of the unity lattice spacing Δh to LBM time step Δt_{LBM},

$$C = \Delta h / \Delta t_{LBM} \tag{3.40}$$

C is also related to the fluid speed of sound C_s as below,

$$C = \sqrt{3}C_s \tag{3.41}$$

Rather than describing a fluid flow by density, pressure, and flow rate, the primary variables in LBM are the density distribution functions f_i, along with the prescribed velocities $\mathbf{e}_i$. The governing equation for the notable lattice Boltzmann BGK model is given below,

$$f_i(\mathbf{x}+\mathbf{e}_i\Delta t_{LBM}, t+\Delta t_{LBM}) = f_i(\mathbf{x},t) - \frac{1}{\tau}[f_i(\mathbf{x},t) - f_i^{eq}(\mathbf{x},t)] \quad (i=0,...,8) \tag{3.42}$$

where f_i represents the probable quantity of micro-particles at a lattice node moving along the i^{th}-direction with velocity $\mathbf{e}_i$ at a particular time. τ is a dimensionless relaxation time, and f_i^{eq} are a set of distribution functions at which the systems are defined as the equilibrium. The values of the equilibrium distribution functions are given by,

$$\begin{aligned} f_i^{eq} &= t_i\rho_f[1+3(\mathbf{e}_i\cdot\mathbf{u}) + \frac{9}{2}(\mathbf{e}_i\cdot\mathbf{u})^2 - \frac{3}{2}\mathbf{u}\cdot\mathbf{u}] \\ t_0 &= \frac{4}{9}; \quad t_i = \frac{1}{9}, (i=1,2,3,4); \quad t_i = \frac{1}{36}, (i=5,6,7,8). \end{aligned} \tag{3.43}$$

where ρ_f is the fluid density, and $\mathbf{u}$ is the flow velocity.

Seen from Eqns.(3.42) and (3.43), a Eulerian flow field is defined by the configurations of micro-particles. Within each LBM time step, the configurations undergo two phases of computations. Firstly, the micro-particles encounter one another at node $\mathbf{x}$, and change their original directions and velocities by collision. This process is referred to the

'collision phase'. The right hand side of Eqn.(3.42) calculates the post-collision distribution. Thereafter, the updated distribution at node $\mathbf{x}$ is transferred to the adjacent nodes along the i^{th}-direction, so as to give an updated description of the flow field. This is denoted as the 'streaming phase'. Such an implementation is repeated cycle by cycle in LBM, and the macroscopic fluid variables can also be solved through the following relationships,

$$\rho = \sum_{i=0}^{8} f_i \tag{3.44}$$

$$\Delta p = \frac{C^2}{3}\Delta\rho \tag{3.45}$$

$$\mathbf{u} = \frac{\sum_{i=0}^{8} f_i \mathbf{e}_i}{\rho} \tag{3.46}$$

where Δp and $\Delta\rho$ are the changes in pressure and density values, respectively.

However, there has been a main difficulty in applying LBM to a fluid with low viscosity (Han et al., 2007b). This is resulted from the following equation, which needs to be satisfied in the LBM computations:

$$\upsilon = \frac{1}{3}(\tau - \frac{1}{2}) \cdot \Delta h \cdot C \tag{3.47}$$

where υ is the kinematic viscosity of fluid. For a fluid with low viscosity, such as water, the production of Δh and $(\tau - \frac{1}{2})$ is required to be small. A small value of Δh may induce an unnecessarily large scale simulation, which adversely increases the computational cost. While making τ be very close to 0.5 may result in numerical

instability. Therefore, it is essential to incorporate a turbulence model into LBM.

Han et al. (2007b) applied the concept of Large Eddy Simulation (LES) to LBM in their DEM-LBM simulations. In the implementations, LES directly resolves the large eddies, and simulates the small ones using a sub-grid model. Through a filtered form of the LBM equation, solutions at the resolved scale are obtained,

$$\tilde{f}_i(\mathbf{x}+\mathbf{e}_i\Delta t_{LBM}, t+\Delta t_{LBM}) = \tilde{f}_i(\mathbf{x},t) - \frac{1}{\tau_{total}}[\tilde{f}_i(\mathbf{x},t) - \tilde{f}_i^{eq}(\mathbf{x},t)] \quad (i=0,...,8) \qquad (3.48)$$

where $\tilde{f}_i$ are filtered density distribution functions, which reflect the probable quantity of micro-particles at the resolved scale which are travelling along the i^{th}-direction. $\tilde{f}_i^{eq}$ are a set of filtered distribution functions at which the systems are defined to be at the equilibrium. The effect of the unresolved scale (i.e. the sub-grid scale) is principally responsible for energy dissipation through viscous forces. It is considered by a relaxation time τ_t, which corresponds to the turbulence viscosity υ_t as

$$\tau_t = \frac{3\upsilon_t}{C^2\Delta t_{LBM}} \qquad (3.49)$$

τ_t is then added to τ which corresponds to the original fluid viscosity, so as to give a total relaxation time that takes both resolved and unresolved scales into account,

$$\tau_{total} = \tau + \tau_t \qquad (3.50)$$

The standard Smagorinsky sub-grid model (1963) is included, and the turbulence

viscosity is computed as,

$$\upsilon_t = (S_c \Delta h)^2 \bar{S}; \qquad \bar{S} = \frac{\bar{Q}}{2\rho C_s{}^2 \tau_{total}};$$
$$\bar{Q} = \sqrt{2\sum_{i,j} \tilde{Q}_{ij}\tilde{Q}_{ij}}; \quad \tilde{Q}_{ij} = \sum_{\alpha=0}^{8} e_{\alpha i} e_{\alpha j} (\tilde{f}_\alpha - \tilde{f}_\alpha^{eq}) \tag{3.51}$$

where S_c is the Smagorinsky constant. $\bar{S}$ relates to the filtered strain rate tensor, and $\tilde{Q}_{ij}$ are the second-order moments of the non-equilibrium distribution functions. From Eqns.(3.49)-(3.51) and Eqn.(3.41), the total relaxation time is obtained as follow,

$$\tau_{total} = \frac{1}{2}[\tau + \sqrt{\tau^2 + \frac{18\Delta h \cdot S_c^2}{\rho \cdot C^3}\bar{Q}}] \tag{3.52}$$

3.3.2 Boundary conditions

This sub-section illustrates boundary conditions used in this thesis. An example of a left boundary node is used for the ease of illustration. As shown in Figure 3.3, the density distribution functions f_0, f_2, f_3, f_4, f_6, and f_7 can be determined after the streaming phase, while f_1, f_5, and f_8 remain unknown. Therefore, it is necessary to determine the values of f_1, f_5, and f_8 so that the prescribed boundary conditions can be applied.

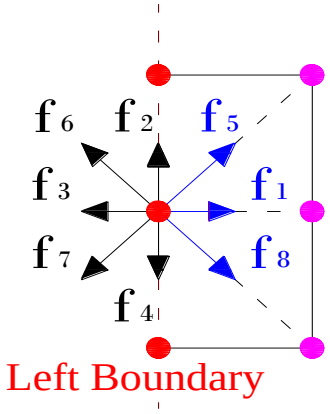

Figure 3.3 A typical lattice node on the left boundary

For a stationary wall boundary, the widely-used bounce-back rule (as stated in Section 2.4) is adopted. It is assumed that there is no tangential velocity along the fluid-wall interface (i.e. no-slip boundary condition). The wall is located half spacing away from the boundary nodes (see Figure 3.4), and the micro-particles coming from the internal nodes are regarded to be bounced back along their original directions:

$$f_{-i}(\mathbf{x}, t + \Delta t_{LBM}) = f_i(\mathbf{x}, t_+) \tag{3.53}$$

where *-i* denotes the opposite direction of *i*. $f_i(\mathbf{x}, t_+)$ represents the post-collision distribution.

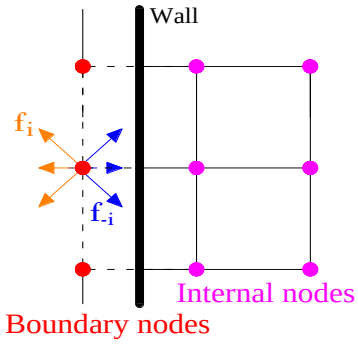

Figure 3.4 Bounce-back rule

Hence, in a left boundary node as shown in Figure 3.3, there are

$$f_1 = f_3, \quad f_5 = f_7, \quad f_8 = f_6 \tag{3.54}$$

For a pressure/density boundary condition, the pressure/density values have to be specified at all boundary nodes. Suppose the velocity along *y*-direction is zero in a pressure/density inlet problem, Eqns.(3.44) and (3.46) lead to the following relationships:

$$f_1 + f_5 + f_8 = \rho_b - (f_0 + f_2 + f_3 + f_4 + f_6 + f_7) \tag{3.55}$$

$$f_5 - f_8 = -f_2 + f_4 - f_6 + f_7 \tag{3.56}$$

where ρ_b is the specified density at the boundary node. Nevertheless, in order to determine the three unknowns f_1, f_5, and f_8, one more equation is required to get a unique solution.

A non-equilibrium bounce-back assumption, proposed by Zou and He (1997), is employed to close the above equation system. It is assumed that the non-equilibrium part of the density distribution is bounced back along the normal direction. In the case shown in Figure 3.3, there is

$$f_1 - f_1^{eq} = f_3 - f_3^{eq} \tag{3.57}$$

Hence,

$$f_1 = f_3 + \frac{2}{3}\rho_b u_x \tag{3.58}$$

From Eqns.(3.55) and (3.46), the velocity in the *x*-direction is obtained as follows,

$$u_x = 1 - \frac{f_0 + f_2 + f_4 + 2(f_3 + f_6 + f_7)}{\rho_b} \tag{3.59}$$

Combined the above equation with Eqns.(3.55) and (3.56), f_1, f_5, and f_8 can be uniquely determined.

As for a velocity inlet boundary condition, u_x is specified at the boundary node instead of ρ_b. The determination of f_1, f_5, and f_8 is similar to that of the pressure/density boundary condition. And the equation system is derived as follows,

$$\begin{aligned} &f_1 + f_5 + f_8 = \rho_b u_x + (f_3 + f_6 + f_7); \\ &f_5 - f_8 = -f_2 + f_4 - f_6 + f_7; \\ &f_1 = f_3 + \frac{2}{3}\rho_b u_x; \\ &\rho_b = \frac{f_0 + f_2 + f_4 + 2(f_3 + f_6 + f_7)}{1 - u_x}. \end{aligned} \tag{3.60}$$

3.4 Two-Way Coupling

3.4.1 Interactions between fluid and solid particles

In order to describe the interactions between fluid and solid particles in the context of LBM, it is necessary to have the solid particles firstly mapped onto the LBM Eulerian lattice. The lattice representation of a circular particle is illustrated in Figure 3.5. The nodes connected to each other across the particle boundary are denoted as boundary

nodes. The link connecting one boundary node interior to the particle and the other one exterior to the particle are denoted as a boundary link. Drawing across all the middle points of boundary links generates the particle surface on basis of the LBM lattice. It is clear that due to such a stepwise lattice representation, a smooth solution may be difficult to acquire unless a sufficiently fine lattice is adopted.

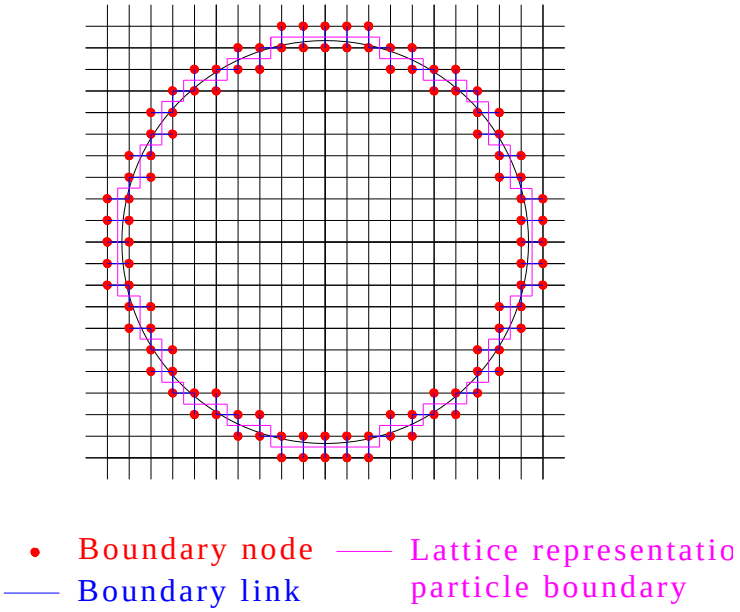

Figure 3.5 Stepwise lattice representation of a circular solid particle

In order to cope with the problem mentioned above, the Immersed Moving Boundary (IMB) scheme is employed. In IMB, a nodal cell (see Figure 3.6) is introduced for each lattice node, with its size identical to a lattice square. The node is located at the centre of the cell. The volume fraction of the nodal cell covered by a solid particle is represented by the local solid/fluid ratio λ.

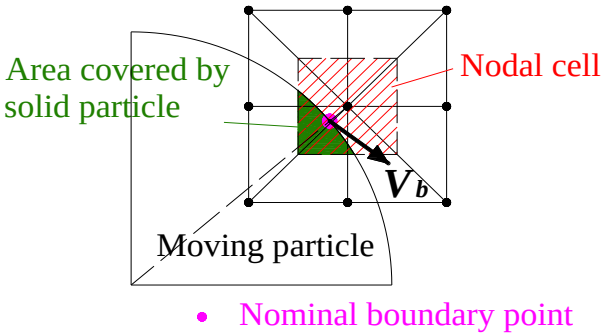

Figure 3.6 A nodal cell and the fractional area covered by a solid particle

The standard LBM equation (see Eqn.(3.42)) is then modified by λ as

$$f_i(\mathbf{x}+\mathbf{e}_i\Delta t_{LBM}, t+\Delta t_{LBM}) = f_i(\mathbf{x},t) - \frac{1}{\tau}(1-\lambda)[f_i(\mathbf{x},t) - f_i^{eq}(\mathbf{x},t)] + \lambda\Omega_i^s$$
$$(i = 0,...,8) \qquad (3.61)$$
$$\Omega_i^s = f_{-i}(\mathbf{x},t) - f_i(\mathbf{x},t) + f_i^{eq}(\rho,\mathbf{u}_b) - f_{-i}^{eq}(\rho,\mathbf{u})$$

where Ω_i^s represents the bounce-back of the non-equilibrium part of the distribution functions. $\mathbf{u}_b$ is the velocity of the particle at the nominal boundary point (see Figure 3.6).

If $\lambda = 0$, it can be identified that Eqn.(3.61) recovers the standard LBM equation (i.e. Eqn.(3.42)). This indicates a nodal cell fully filled with fluid. While if $\lambda = 1$, the second term on the right hand side of Eqn.(3.61) vanishes, and the post-collision distribution is calculated as if the cell is purely covered by solid. In general, λ varies between 0 and 1, and the influence of the moving solid particle on the local fluid flows are taken into account.

On the other hand, the fluid-induced force and torque acted on the solid particle are also

obtained through the summations as follow,

$$\mathbf{F}_h = C\Delta h(\sum_m B_m \sum_i \Omega_i^s \mathbf{e}_i) \tag{3.62}$$

$$\mathbf{T}_h = C\Delta h \sum_m (\mathbf{x}_m - \mathbf{x}_s) \times (B_m \sum_i \Omega_i^s \mathbf{e}_i) \tag{3.63}$$

where the summations are performed over all the boundary nodes. $\mathbf{x}_m$ is the location of lattice node m. $\mathbf{x}_s$ denotes the location of the nominal boundary point. After $\mathbf{F}_h$ and $\mathbf{T}_h$ are computed, they are used to update the total particle force and torque in Eqns.(3.1) and (3.2) for DEM calculation. In such a way, the description of interactions between fluid and solid phases is numerically accomplished.

3.4.2 Sub-cycling

Normally, the time step used in LBM is stated to be larger than that in DEM (Feng et al., 2007). Δt_{DEM} shall be taken as a fraction less than a critical time step so as to achieve numerical stability (Cundall and Strack, 1978). As for the contact model used in this thesis, the critical time step is given according to the Rayleigh wave speed of force transmission (see e.g. Yang, 2009),

$$\Delta t_c = \frac{\pi R_{ave}}{(0.8766 + 0.1631\nu)} \sqrt{\frac{\rho_p}{G}} \tag{3.64}$$

where R_{ave} is the averaged particle radius, and ρ_p is the particle density. G and ν are shear modulus and Poisson's ratio of the particle, respectively.

While in LBM, the lattice speed C is determined firstly. In an effort to guarantee a good

approximation of an incompressible fluid, the following relationship is required to be satisfied, as recommended by Han et al (2007b):

$$Ma = \frac{u_{\max}}{C} << 1 \tag{3.65}$$

Afterwards, the lattice spacing and time step are chosen using Eqns.(3.40) and (3.47).

Due to the inconsistency between Δt_{DEM} and Δt_{LBM}, Feng et al. (2007) proposed a sub-cycling scheme to ensure an overall stable solution for the coupling technique. In this scheme, Δt_{DEM} is replaced by a slightly smaller value Δt^*_{DEM},

$$\begin{aligned} \Delta t^*_{DEM} &= \frac{\Delta t_{LBM}}{N} \\ N &= \text{int}[\frac{\Delta t_{LBM}}{\Delta t_{DEM}}] + 1 \end{aligned} \tag{3.66}$$

Eqn.(3.66) results in a sub-cycling time integration for DEM: within one LBM cycle, N sub-cycles of DEM calculations are conducted, with the fluid-induced force and torque kept constant.

3.4.3 Unit systems

Unlike the DEM calculations in which physical units can be directly applied, the LBM computations adopt the lattice unit (*l.u.*) system. Hence, conversions between physical units and lattice units are necessary for all relevant variables. Similar to the base

units (such as metre for length, kilogram for mass, and second for time) in physical unit system, there are three base units (*ll.u.* for length, *ρl.u.* for density, and *tl.u.* for time) defined in the lattice unit system as well:

Length unit: $1ll.u. = \Delta h$

Density unit: $1\rho l.u. = \rho_w = 1000kg/m^3$

Time unit: $1tl.u. = \Delta t$

According to the above base units, all relevant variables in physical units can be conversed to those in lattice units. A complete list regarding the conversions can be found in Feng et al. (2007).

3.4.4 Hydraulic radius

In the fluid-particle two-way coupling, a hydraulic radius R_h, rather than the actual radius of a particle R, is adopted for a cylinder to give an equivalent drag force to a sphere:

$$\frac{\mathbf{F}_D(cylinder)}{\mathbf{F}_D(sphere)} = \frac{\frac{1}{2}\rho \mathbf{v}_r{}^2 A(cylinder) C_d(cylinder)}{\frac{1}{2}\rho \mathbf{v}_r{}^2 A(sphere) C_d(sphere)} = \frac{C_d(cylinder)}{C_d(sphere)} \cdot \frac{R_h / R}{0.25\pi} = 1 \qquad (3.67)$$

Hence,

$$\frac{R_h}{R} = 0.25\pi \cdot \frac{C_d(sphere)}{C_d(cylinder)} \qquad (3.68)$$

where $\mathbf{F}_D$ denotes the drag force applied to a particle. $\mathbf{v}_r$ is the speed of particle relative to fluid. A is the reference area. C_d is the drag coefficient only related to particle Reynolds number, and is taken as 0.44 according to Zhu et al. (2007).

Therefore,

$$\frac{R_h}{R} \approx 0.8 \tag{3.69}$$

It can be seen that the hydraulic radius is smaller than the actual radius of a particle. In a two-dimensional simulation, no fluid paths exist through the particle assembly, which is regarded unrealistic. However, such situation can be addressed by adopting the hydraulic radius, as also reported in Boutt et al. (2007).

3.5 Flow Chart of Complete DEM-LBM Calculations in *FPS-BHAM*

The complete DEM-LBM calculation process in *FPS-BHAM* is demonstrated through the flow chart shown in Figure 3.7.

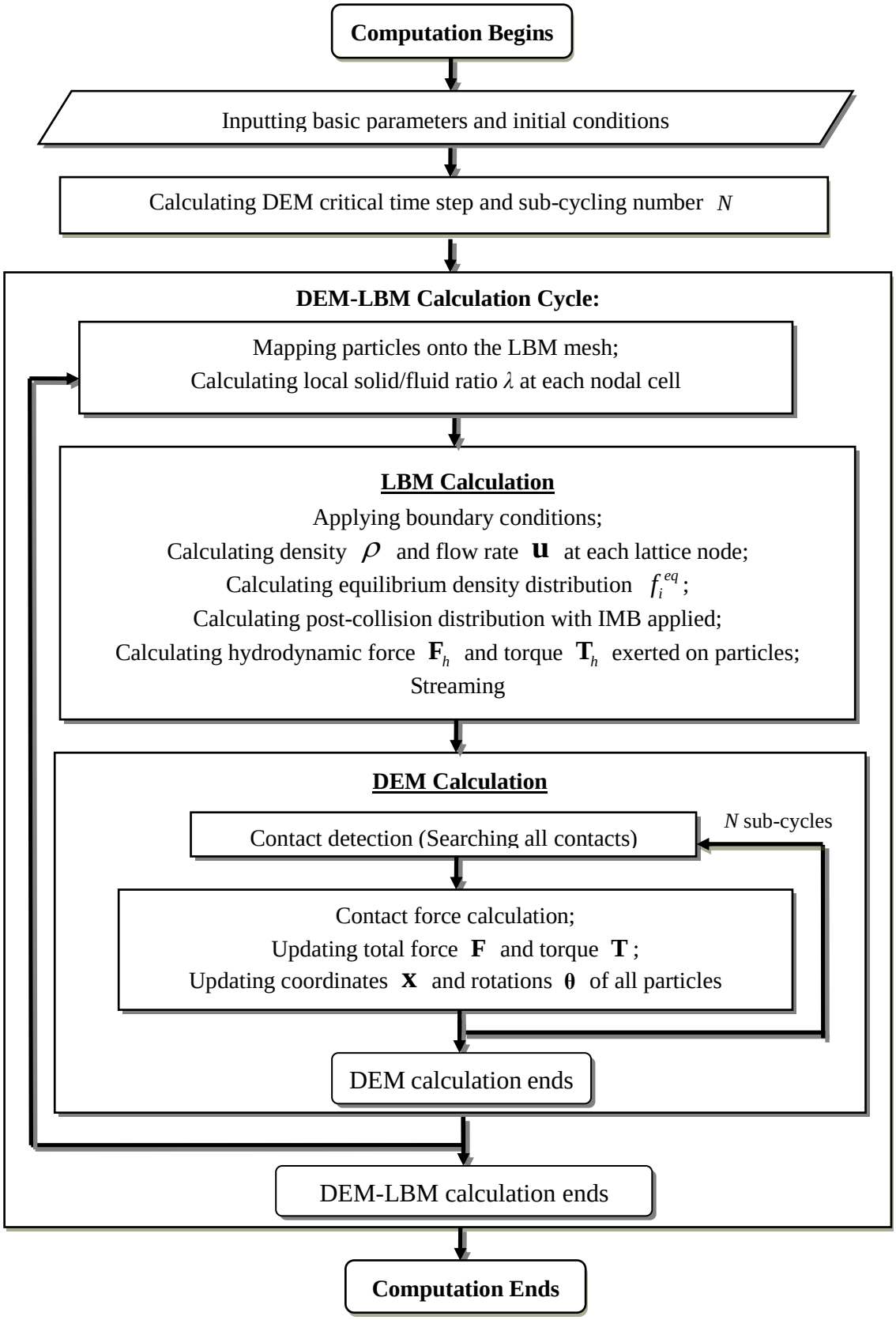

Figure 3.7 Flow chart of the coupled DEM-LBM computation in *FPS-BHAM*

In the beginning of computations, basic parameters of solid particle and fluid properties are input and initial boundary conditions are set up. The time steps in DEM and LBM calculations are then determined, giving the sub-cycling number N (see Eqn.(3.66)). The DEM-LBM computations start from mapping particles onto the LBM Eulerian lattice. The local solid/fluid ratio is calculated at each nodal cell. Afterwards, LBM begins to compute. In each LBM calculation cycle, the lattice Boltzmann equation is solved with LES and IMB incorporated (see Eqns.(3.48) and (3.61)). The fluid-induced force and torque acted on each solid particle are also obtained from Eqns.(3.62) and (3.63), and regarded constant when applied to the N sub-cycles of DEM calculation. Once DEM begins to run, contact detection is firstly conducted to search for all particle/particle and particle/wall contacts. The contact force is then calculated once a contact is identified. Afterwards, total force and torque applied to each particle can be determined, and the particle location and rotation are updated by Eqns. (3.3) and (3.4). They are then used for contact detection in the following DEM sub-cycle, or for particle mapping in the following DEM-LBM cycle. The same computations as stated above are repeated cycle by cycle till the end of computation.

3.6 Summary

A DEM-LBM computer program *FPS-BHAM* is developed in order to capture the behaviour of a fluid-particle system in a scenario of a pipe leakage problem. This chapter outlines the main computational elements involved in the implementations. *FPS-BHAM* uses DEM to describe the solid phase by tracing particle motions, and employs LBM to simulate fluid flows. The contact force calculation from a well-established code *TRUBAL* is directly transferred into *FPS-BHAM*. Besides, with the aid of the IMB scheme, not only the influence of a moving particle on local fluid flows can be described, but the fluid-induced force and torque applied to the solid particle can be determined.

In *FPS-BHAM*, calculations are performed cycle by cycle. Within every calculation cycle, particles are firstly mapped onto the LBM lattice. The lattice Boltzmann equation is solved with IMB scheme being employed. Afterwards, a number of DEM sub-cycles are conducted, with the fluid-induced force and torque being kept constant in a single DEM-LBM cycle. The force and torque are then added to the DEM formulas to update particle location and rotation, and prepare for computation in the next calculation cycle. All variables used in the DEM-LBM implementations are conversed into lattice units. Moreover, a hydraulic radius that is smaller than the actual particle radius is adopted when solving the fluid-particle interactions. This is intended to build up fluid paths through the particle assembly in a two-dimensional simulation.

CHAPTER 4: CODE VERIFICATION

4.1 Introduction

In order to check if all the algorithms in *FPS-BHAM* have been correctly implemented, code verification is necessary before performing numerical studies of the pipe leakage problem. As stated in Chapter 3, the development of *FPS-BHAM* consists of the following main elements:

(i) establishing the DEM calculation process, including the incorporation of the contact force calculation subroutines from *TRUBAL*;

(ii) implementing the LBM computation with different boundary conditions; and

(iii) applying the IMB scheme to the LBM computation.

In this chapter, verification through a series of simple tests is conducted in order to examine the DEM calculations, the LBM implementations, and the incorporation of IMB. The results are demonstrated in Sections 4.2-4.4, respectively. A brief summary is finally given in Section 4.5.

4.2 Particle Collision Using DEM

As the contact force calculation subroutines in *FPS-BHAM* are directly transferred from the well-established *TRUBAL*, it is reasonable to compare the DEM results from

FPS-BHAM and from *TRUBAL*. In this section, tests on particle-wall and particle-particle collisions are carried out, with both non-adhesive and adhesive particles being used.

4.2.1 Particle-wall collision

As shown in Figure 4.1, a non-adhesive particle drops from a height of 5m with zero initial velocity and collides with a horizontal wall located at the ground. The particle is placed in a force field of 1.0N along x-axis and -9.81N along y-axis. The particle has a radius of 1.0m and density of 2700kg/m^3. Other DEM parameters used in the test is listed in Table 4.1.

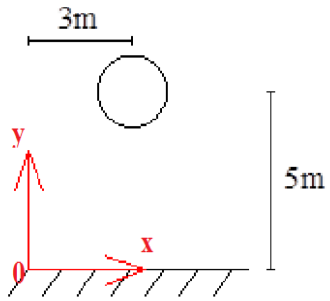

Figure 4.1 Test setup of a particle-wall collision

Table 4.2 records the particle location at 1.0s (10,000 DEM time steps), which is a short time after colliding with the wall. The results are compared with those from *TRUBAL* in Table 4.2 as well.

Table 4.1 DEM parameters used in particle-wall collision test

Particle Young's modulus	689.5 MPa
Particle Poisson's ratio	0.3
Particle surface energy	0.0 J/m^2
Particle friction coefficient	0.3
Global damping factor	0.01
Particle-wall contact damping factor	0.032
DEM time step	1×10^{-4} s

Table 4.2 Computational results: location of a non-adhesive particle at 1.0s (10,000 DEM time steps)

	FPS-BHAM	*TRUBAL*	Relative Difference
x-coordinate	3.47868799681111	3.478647	1.2×10^{-5}
y-coordinate	1.50291630562420	1.503515	4.0×10^{-4}
Rotation	-4.924805065012636E-002	-4.9541231E-02	4.7×10^{-5}

The difference in the computational outcome is thought to be resulted from two main reasons. Firstly, the round-off error exists as the double-precision data type is adopted in *FPS-BHAM*, while only the single-precision type is adopted in *TRUBAL*. Moreover, in *FPS-BHAM*, the particle location is updated at the end of each DEM cycle following the total force calculation. However, in *TRUBAL*, the particle location is updated in the

beginning of each cycle, using the total force obtained from the previous cycle. Therefore, there exists one-cycle difference in the total force, and hence results in subtle error in the particle location after a number of cycles.

In the second test, an adhesive particle is adopted to collide with the wall. The same set of DEM parameters is used except the particle surface energy value given as 5.0J/m^2. Table 4.3 shows the comparison between the results from different codes.

Table 4.3 Computational results: location of an adhesive particle at 1.0s (10,000 DEM time steps)

	FPS-BHAM	*TRUBAL*	Relative Difference
x-coordinate	3.47872202336254	3.478651	2.0×10^{-5}
y-coordinate	1.49850369704832	1.499619	7.4×10^{-4}
Rotation	-4.916298427281438E-002	-4.9533658E-02	5.9×10^{-5}

Compared Table 4.3 with Table 4.2, it is seen that the relative difference is larger with the presence of particle adhesion. This is probably because more computations are involved in the auto-adhesive elastic contact model (see Section 3.2.2), and thereby increase the round-off error during computations. In spite of this, it can be seen that effectively the same DEM results are still obtained from *FPS-BHAM*.

4.2.2 Particle-particle collision

In order to examine the accuracy of DEM calculation on a particle-particle collision, an example of two particles is adopted in this sub-section. As shown in Figure 4.2, Particle A drops from a height of 5m with zero initial velocity and collides with Particle B which is resting on the horizontal wall. Both particles have non-zero surface energy values and placed in a force field of -9.81N along y-axis. Particle A has a radius of 1.0m and density of 2700kg/m^3, and Particle B has a radius of 1.5m and density of 5000kg/m^3. Other DEM parameters used in the test is listed in Table 4.4. Locations of both particles at 1.0s (10,000 time steps) are listed and compared in Table 4.5.

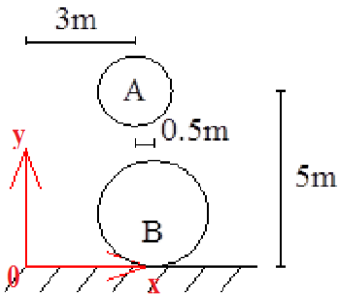

Figure 4.2 Test setup of a particle-particle collision

Table 4.4 DEM parameters used in particle-particle collision test

	Particle A	Particle B	Wall
Young's modules	689.5 MPa	889.5 MPa	1089.5 MPa
Poisson's ratio	0.3	0.31	0.32
Surface energy	5.0 J/m^2	5.0 J/m^2	5.0 J/m^2
Friction coefficient	0.3	0.4	0.5
Global damping factor	0.01	0.01	0.01
Particle-particle contact damping factor	0.016	0.016	0.016
Particle-wall contact damping factor	0.032	0.032	0.032
Time step	1×10^{-4} s		

Again, the relative difference shown in Table 4.5 is attributed to the round-off error and the one-cycle difference in the DEM computation procedure. After all, *FPS-BHAM* provides valid DEM results for particle-wall and particle-particle collisions with both non-adhesive and adhesive particles, as indicated by all the tests reported in this whole section.

Table 4.5 Computational results: particle locations at 1.0s (10,000 DEM time steps)

	FPS-BHAM	*TRUBAL*	Relative Difference
Particle A: x-coordinate	2.37865248309718	2.377825	3.5×10^{-4}
Particle A: y-coordinate	3.69968790405553	3.707772	2.2×10^{-3}
Particle A: Rotation	0.532251228249104	0.5343704	3.4×10^{-4}
Particle B: x-coordinate	3.56397902181272	3.560187	1.1×10^{-3}
Particle B: y-coordinate	1.47691041564697	1.476991	5.5×10^{-5}
Particle B: Rotation	-3.489849718559125E-002	-3.6935519E-02	3.2×10^{-4}

4.3 Fluid Flow Using LBM

In this section, numerical tests are carried out using *FPS-BHAM* on a Poiseuille flow with velocity and pressure boundaries. The results are compared with the analytical solutions. The aim of this is mainly to verify whether the LBM computations are correctly implemented with different boundary conditions.

4.3.1 Poiseuille flow with a velocity boundary

A flow channel is set up using *FPS-BHAM* with a length of 200*ll.u.* (for details of the lattice unit system, please refer to Section 3.4.3). Two parallel walls are fixed at the top and bottom boundaries with a separation of 100*ll.u.*. A velocity inlet is given at the left boundary, and its profile fits the analytical expression as,

$$u_x = u_{\max}[1-(\frac{y-Y/2}{Y/2})^2] \tag{4.1}$$

where Y is the width of channel, and $u_{\max}$ is the maximum fluid velocity at boundary. In this test, $u_{\max} = 0.01 l.u.$, giving the Mach number of 0.01. According to Han et al. (2007b), this would guarantee a sufficiently accurate result for an incompressible fluid. The bounce-back rule is applied to the top and bottom boundaries so as to achieve the no-slip condition for stationary walls. The velocity boundary based on the scheme proposed by Zou and He (1997) (see Section 3.3.2) is applied to the left boundary, and the zero excess pressure boundary is applied to the right one.

After the test begins, the fluid flow in the channel is developing until a steady state is reached. The numerical results at the steady state are compared with the analytical solution in Eqn.(4.1). During each LBM cycle, the global velocity error is calculated over all the lattice nodes in the computational domain by (Cook et al., 2004),

$$E_v = \frac{\sqrt{\Sigma \left| u_{LBM} - u_{analytical} \right|^2}}{\sqrt{\Sigma \left| u_{analytical} \right|^2}} \tag{4.2}$$

where the subscripts *LBM* and *analytical* indicate values given by LBM and the analytical expression, respectively. After a sufficient period (around 43,000 LBM calculation cycles), the difference in the global error between two successive time steps converges to 2×10^{-5}, indicating that steady state is reached (see Figure 4.3). The final global error is found to be 0.48%.

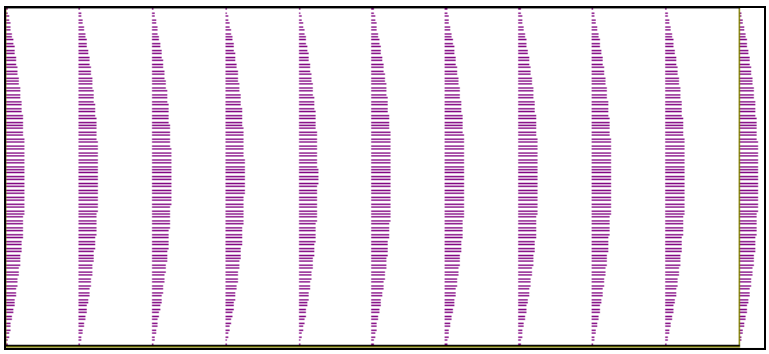

Figure 4.3 LBM results with a velocity boundary: velocity profile in Poiseuille flow

4.3.2 Poiseuille flow with pressure boundaries

In order to examine the capability of *FPS-BHAM* in simulating fluid flows with pressure boundary condition, in the test reported here, the pressure boundary scheme proposed by Zou and He (1997) (see Section 3.3.2) is adopted. A fluid channel has a length of 100*ll.u.* and a width of 25*ll.u.*. The bounce-back rule is applied to the paralleled top and bottom boundaries so as to achieve the no-slip condition for the stationary walls.

The fluid has an initial density of $1.0\rho l.u$ and zero velocity over the domain, except that two different density values are specified at the left and right boundaries:

$$\rho_{in} = 1.0005\rho l.u.; \quad \rho_{out} = 0.9995\rho l.u. \tag{4.3}$$

which corresponds to pressure values according to Eqn.(3.44):

$$p_{in} = \frac{1.0005}{3} l.u.; \quad p_{out} = \frac{0.9995}{3} l.u. \tag{4.4}$$

Therefore, a flow between the two walls is driven under the constant pressure drop along the channel.

In the test, the LBM dimensionless relaxation time $\tau = 0.8$. From Eqn.(3.46), the kinematic viscosity of the fluid is obtained:

$$\upsilon = \frac{1}{3}(\tau - \frac{1}{2}) \cdot \Delta h \cdot C = 0.1 l.u. \tag{4.5}$$

Hence, the dynamic viscosity is calculated as,

$$\mu_f = \upsilon \cdot \rho_0 = 0.1 \cdot 1.0 = 0.1 l.u. \tag{4.6}$$

The exact solution to the pressure-driven flow at the steady state is shown as,

$$u = \frac{1}{2\mu_f} \frac{p_{out} - p_{in}}{L} y^2 - \frac{H}{2\mu_f} \frac{p_{out} - p_{in}}{L} y, \qquad y \in [0, H] \tag{4.7}$$

where L and H are the length and width of the domain, respectively. By substituting Eqns.(4.4) and (4.6) into Eqn.(4.7), the general expression of the analytical solution is obtained as

$$u = -\frac{5}{3} \times 10^{-5} y^2 + \frac{125}{3} \times 10^{-5} y \tag{4.8}$$

which indicates that velocity is zero at the walls and reaches the maximum in the middle. The Mach number is calculated as 0.0026, which is much smaller than 1.0 so that the incompressibility requirement is fulfilled (Han et al., 2007b).

Figure 4.4 shows the velocity profile at the steady state. The global velocity error is 2.34%, which is computed over all the lattice nodes in the computational domain.

Figure 4.4 LBM results with pressure boundaries: velocity profile in Poiseuille flow

From the results presented in this section, it can be seen that a correct implementation of LBM is accomplished with both velocity and pressure boundaries. However, the demand of simulating the pipe leakage problem would need to be met when a large amount of solid particles act as moving boundaries. Therefore, an examination of *FPS-BHAM* on its capability of modelling fluid flows with moving solid boundaries is necessary and demonstrated in the following section.

4.4 Fluid Flow with Moving Solid Boundaries

Two tests on the Couette flows are carried out using IMB in this section. A horizontal Couette flow adopts the value of 0.5 for the solid/fluid ratio λ at all the wall boundary nodes. While a cylindrical Couette flow suffers various solid/fluid ratios at the boundary nodes, and hence the sophisticated calculation for the solid/fluid ratio in *FPS-BHAM* can be verified as well.

4.4.1 Plane Couette flow

Firstly, a plane Couette flow between two parallel walls is modelled. The bottom wall is fixed, while the top wall is translating horizontally with a constant velocity $u_0 = 0.1 l.u.$. Fluid domain is divided into a 300×50 lattice grid. IMB is applied to both the top and bottom walls. The fluid has an initial zero velocity over the whole domain. A flow is driven by the top wall through viscous force. The analytical solution to the plane Couette flow at the steady state is shown as,

$$u = u_0 \cdot \frac{y}{H}, \quad y \in [0, H] \tag{4.9}$$

where H is the width of the domain.

After the test begins, fluid velocities are gradually developed until the steady state is reached after a sufficiently long time (around 20,000 LBM time steps), when the global velocity error convergences to 1.6%. The velocity profile at the steady state is shown in

Figure 4.5.

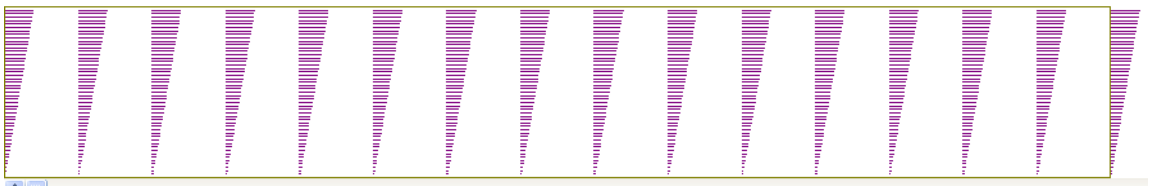

Figure 4.5 LBM results with IMB: velocity profile in plane Couette flow

4.4.2 Cylindrical Couette flow

In the second test, a cylindrical Couette flow between two concentric circular walls is modelled. The outer wall has a radius of $60ll.u.$ and the inner one of $40ll.u.$. Both walls are rotating yet with different angular speeds of $0.0001rad/s$ and $0.0002rad/s$, respectively. The fluid domain is divided into a 160×160 lattice grid, and IMB is applied to the two rotating walls. A flow is thereby driven through viscous force. The analytical solution to the fluid velocity between the two walls at the steady state is expressed as,

$$u = Ar + \frac{B}{r} \tag{4.10}$$

where

$$A = \frac{\Omega_2 r_2^2 - \Omega_1 r_1^2}{r_2^2 - r_1^2}, \quad B = \frac{(\Omega_1 - \Omega_2) r_1^2 r_2^2}{r_2^2 - r_1^2} \tag{4.11}$$

in which Ω_1, r_1, Ω_2, and r_2 are the angular velocities and radii of the inner and outer walls, respectively.

Besides, at the steady state, the torque applied by the flow to a unit length of the inner wall is given analytically by

$$T = \frac{-4\pi\rho\upsilon(\Omega_1 - \Omega_2)r_1^2 r_2^2}{r_2^2 - r_1^2} \tag{4.12}$$

The numerical test starts with zero fluid velocity. The steady state is reached after around 5,000 LBM time steps, when the global velocity error and the torque relative error converge to 1.1% and 1.5%, respectively. The velocity profile at the steady state is shown in Figure 4.6.

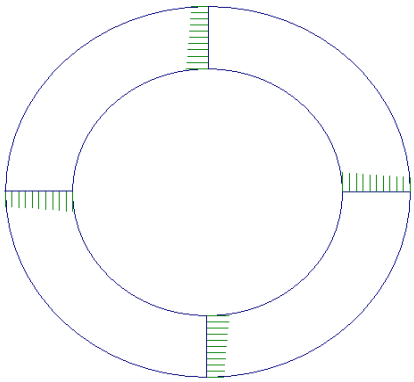

Figure 4.6 LBM results with IMB: velocity profile in cylindrical Couette flow

Results demonstrated in this section suggest that with IMB employed, *FPS-BHAM* is capable of providing valid solutions to fluid flow with moving solid boundaries. Besides, the torque generated on the moving boundary by fluid flow can also be effectively obtained.

4.5 Summary

Through simple tests on particle-wall and particle-particle collisions, the capability of *FPS-BHAM* in DEM calculations is examined by comparing the computational results with those from the well-established *TRUBAL* code. A subtle difference is observed and is attributed to round-off error and different DEM calculation procedures. In spite of the difference, *FPS-BHAM* provides valid results for tracing particle locations after contacts. Moreover, in order to verify whether the LBM computations are correctly implemented in *FPS-BHAM*, the Poiseuille flows with velocity and pressure boundaries, as well as the Couette flows with moving solid boundaries are tested, respectively. The results are validated against analytical solutions. It is found out that *FPS-BHAM* not only achieves valid solutions, but also effectively obtains the fluid-induced torque acted on the moving boundary. Code verification presented in this chapter indicates the potential capability of *FPS-BHAM* in simulating a fluid-particle system. Further validations are provided against experimental findings in Chapter 5, which helps to understand whether the numerical model is sufficient for the need of this research, i.e. to describe the localisation phenomenon, the intensive fluid-particle interactions, and the bed behaviour.

CHAPTER 5: ONSET OF FLUIDISATION

5.1 Introduction

Verified by simple tests in Chapter 4, *FPS-BHAM* can be regarded effective to provide description of particle and fluid behaviour with interactions between them. As the aim of this research is to achieve a deeper insight into the internal fluidisation induced by a leaking pipe, a granular bed subject to a locally injected fluid is tested in this chapter using *FPS-BHAM*. By comparing with experimental findings, the capability of *FPS-BHAM* in simulating localisation phenomenon and bed behaviour due to a local leakage is validated. Besides, with the aid of numerical simulation, a complete account for the regimes of bed behaviour under various flow rates can be obtained. Better knowledge and understanding of the onset of fluidisation as well as the cavity evolution can also be acquired. Using *FPS-BHAM*, this chapter provides an overview of different bed regimes with various flow rate, and reports on the numerical studies concerning the onset of fluidisation so that fluidising mechanism is explored. As for the understanding of the cavity evolution, analyses using the numerical data from parametric studies are performed and demonstrated in Chapter 7.

As stated in Section 2.2, an investigation into the fundamentals underlying a granular bed subject to a locally injected fluid has been successfully performed using physical experiments by Alsaydalani (2010). Therefore, it would be worth considering a similar

sample model using *FPS-BHAM* and carrying out numerical simulations for a comparable study. For this reason, in Section 5.2, the setup of the experimental model by Alsaydalani (2010) is briefly introduced before illustrating the numerical model. Observations of bed behaviour and monitoring of excess pressures are demonstrated in Section 5.3, which indicates different bed regimes under various controlled flow rates. Comparable studies with findings from previous research are conducted in Section 5.4, implying the numerical model can adequately describe the localisation phenomenon and the onset of fluidisation. Thereafter, theoretical analysis on the fluidising mechanism is carried out in Section 5.5, and the measured results from numerical tests are validated against the predicted ones from the analytical solution. Finally, the main findings in this chapter is summarised in Section 5.6.

5.2 Model Setup

5.2.1 Experimental model

A two-dimensional experimental study (Alsaydalani, 2010) was conducted on a sand bed contained in a tank. It was connected to an inlet water pipe through a slot-shaped orifice. During the test process, the sand bed was fully submerged under water. A schematic diagram of the experimental setup is reproduced in Figure 5.1. The bed had dimensions of 600mm in length and 300mm in height. With progressively increased flow rate, internal fluidisation was identified. Observations in the soil bed were made with the

aid of Particle Image Velocimetery (PIV) which was a widely-used image analysis technique. Pore pressures were also monitored using standpipes attached to the centre line of the tank.

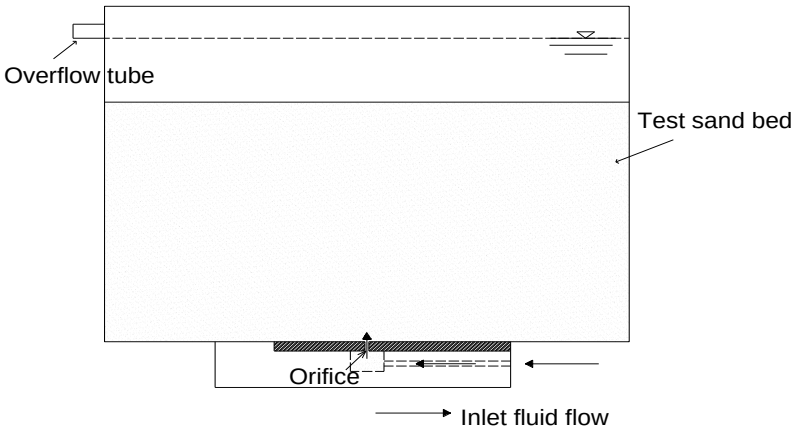

Figure 5.1 Schematic diagram of the experimental setup

In order to conduct a comparable study with the experimental findings, a similar numerical model is built up in this chapter. An illustration of this model is given in the following sub-section.

5.2.2 Numerical model

A two-dimensional numerical model is constructed using *FPS-BHAM* to re-establish a granular bed submerged under water (see Figure 5.2). The bed consists of 9,997 circular particles with a uniform size distribution. Their diameters are 3.0mm, 4.0mm, 5.0mm and 6.0mm, respectively. It shall be noted the particles are much larger than real soil particles,

and the reason for adopting them is to dramatically reduce the computational cost. Non-adhesive particles are adopted in all tests presented in this chapter as sand was used in the experiment. The bed is packed by dropping particles freely and settling them down for a sufficient period. The resulting dimensions are of 600mm in length and 290mm on average in height. As shown in Figure 5.2, the particles are coloured in layers so that the deformation in the bed due to the injected fluid can be clearly identified. The whole computational domain is divided into a 600×400 lattice grid, and hence the bed is fully submerged. An orifice with a width of 3mm is located in the middle of the base, connected with an inlet pipe which spans half length of the bed, so as to obtain a locally injected fluid. During each test, a constant flow rate is applied as a controlled condition, which ranges from 0.25 l/s to 6.0 l/s among tests. Other parameters used in this chapter are listed in Table 5.1.

Although the particle size, the orifice width, and the flow rate are not directly comparable to the experimental model used by Alsaydalani (2010), it is recognised that a consistent mechanism underlying the onset of fluidisation is still achievable. In an effort to demonstrate the validity of the numerical model, the computational output is compared with experimental findings in Sections 5.3-5.4, and with the analytical solution in Section 5.5.

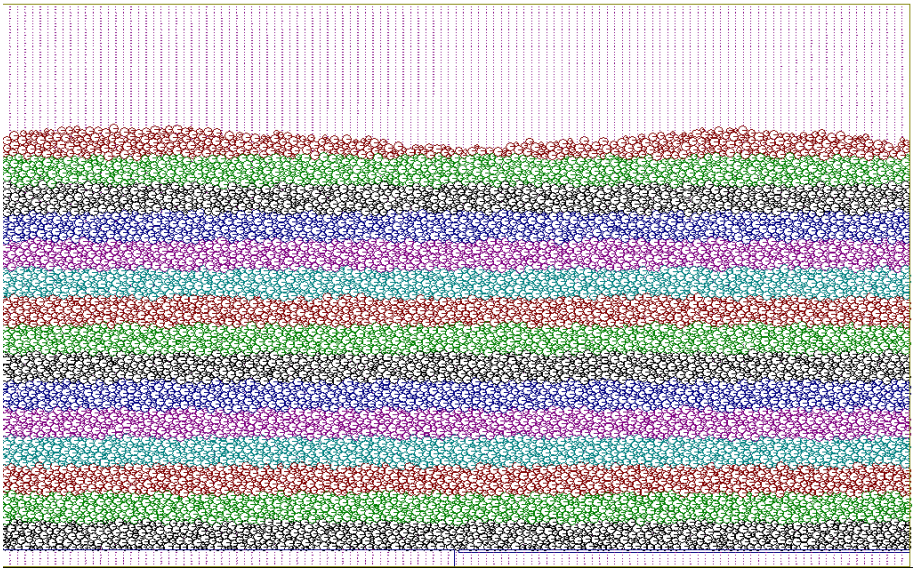

Figure 5.2 Sketch of the numerical setup

Table 5.1 Parameters used in the numerical tests

Parameters	Values
particle density (kg/m^3)	2700
friction coefficient in the DEM calculation	0.3
particle Young's modulus (MPa)	69
particle Poisson's ratio	0.3
DEM time step (s)	2.5×10^{-5}
fluid density (kg/m^3)	1000
kinematic viscosity of the fluid (m^2/s)	1.0×10^{-6}
lattice spacing (m)	1.0×10^{-3}
LBM time step (s)	1.0×10^{-4}
particle surface energy (N/m)	0.0

5.3 Observations from Numerical Results

5.3.1 Different regimes of bed behaviour

With the controlled flow rate varied from 0.25 l/s to 6.0 l/s, numerical results demonstrate different bed behaviours within an identical time period. Figure 5.3 is a diagrammatic representation showing the full transition of bed behaviour with the current model parameters. With a flow rate lower than 0.8 l/s, the particles in bed remain unmoved during the whole test period, making the bed appear as a fixed one. Hence, it is denoted as the 'fixed-bed regime'. If the applied flow rate is within the range of 0.8 l/s to 1.05 l/s, it is found a small cavity is generated and develops to a stable size. This is referred to 'stable-cavity regime'. However, if a higher flow rate beyond this range is applied, not only a cavity is generated, but a continuous growth in its size is also observed. Therefore, it is named 'growing-cavity regime'. If a flow rate higher than 2.0 l/s is applied, the blow-out failure occurs within the test period, where a flow channel is open up to the bed surface, and is termed as 'blow-out regime'.

It is worth noting the bed behaviours obtained from numerical results are comparable to those from previous experimental studies. The fixed-bed regime is characterised as a motionless bed which was also observed by Zoueshtiagh and Merlen (2007). Besides, a steady seepage flow is achieved in this regime (see Section 5.3.2), which agrees with the statement that leaking fluid is permeating through soil (Royal et al., 2008). In addition, a

cavity generation was found by Royal et al. (2008) with a higher pressure, and identified as a local bump-shaped deformation at bed surface by Zoueshtiagh and Merlen (2007) with a higher flow rate. Such a vertical deformation is also seen from numerical output at the growing-cavity regime (see Figure 5.3). Furthermore, the blow-out regime was identified by the above experimental studies, for which Zoueshtiagh and Merlen (2007) found to be a local fluidisation at the bed surface, and Royal et al. (2008) claimed to be a ruptured bed with leaking fluid migrated up to the top surface.

Moreover, as transparency was provided by Perspex sheet in the experiments by Alsaydalani (2010), a locally fluidised zone with a stabilised size was also observed from his results. However, there was no further investigation into such a phenomenon; although this may be more dangerous to the infrastructures as it is difficult to identify from the surface above. Therefore, in Chapter 6, attempts will be made to understand and explore its underlying mechanism using numerical analysis.

In the following sub-sections, observations to the bed regimes are sequentially made. Each regime is characterised by the corresponding time evolutions of the excess pore pressures (presented as ‘p-t curves’ hereinafter) and cavity size (presented as ‘V-t curves’ hereinafter).

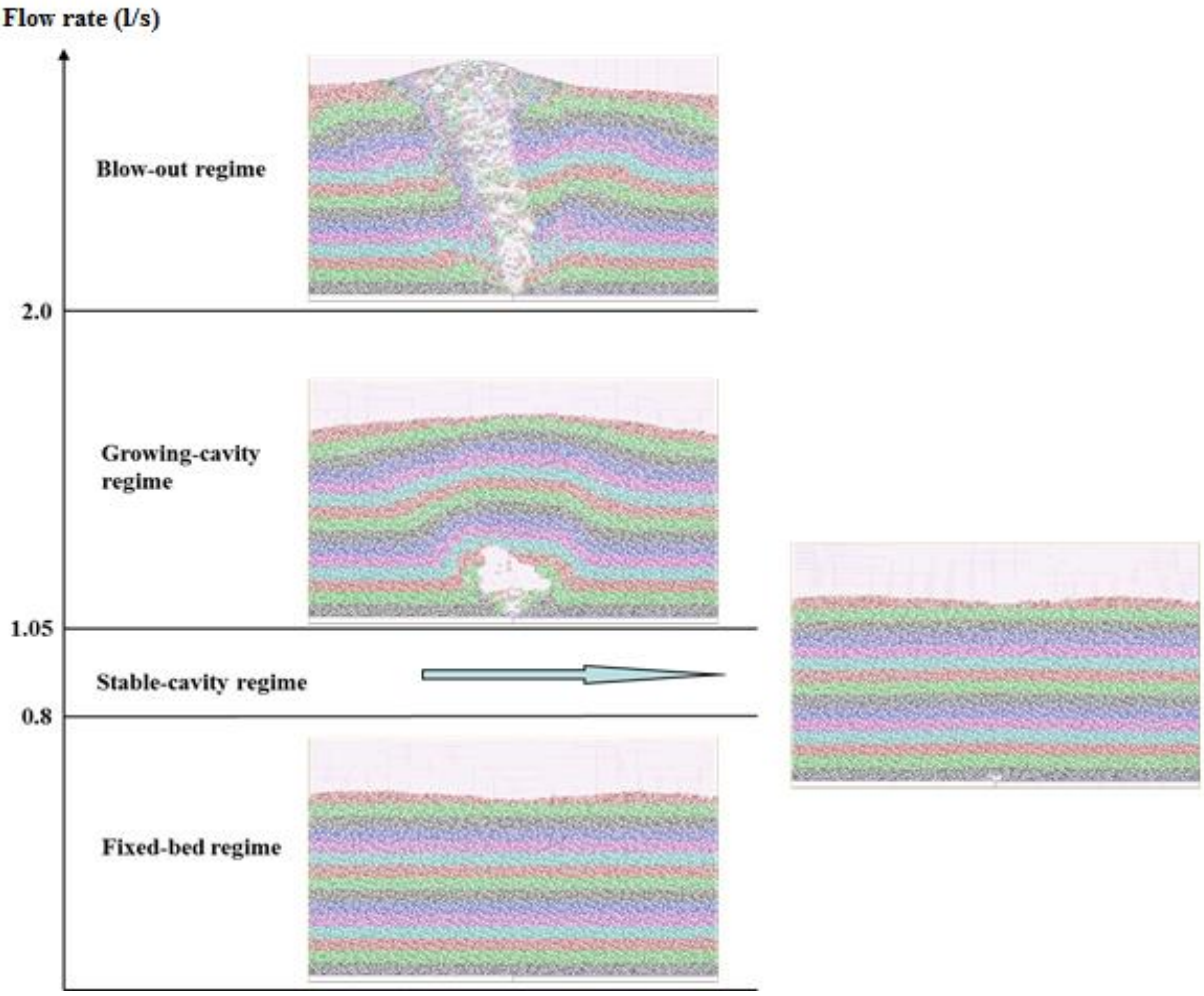

Figure 5.3 Diagrammatic representation showing the full transition of bed behaviour due to a locally injected fluid at different flow rates for the current model parameters (the snapshots are taken at t = 20s)

5.3.2 Fixed-bed regime

From the computational outcome using the current set of model parameters, when subjected to a flow rate below 0.8 l/s, no obvious changes in the particle configuration can

be observed during the whole test. The leaking fluid permeates freely through soil skeleton from the source of flow.

Figure 5.4 shows the time evolution of excess pore pressures at different heights directly above the orifice, i.e. the p-t curves. These heights are chosen to be explored as they are identical to those studied in the experimental work by Alsaydalani (2010). The excess pore pressure within the particle assembly is computed from the LBM density distribution functions at a corresponding fluid node using Eqns.(3.44) and (3.45). From Figure 5.4, it can be seen that all the pressures undergo an initial rise before they level off. A greater excess pressure is generated at a deeper location, where it is closer to the source of flow. The pressure at the orifice increases most rapidly and attains the highest value throughout the whole test. The p-t curves eventually level off, suggesting a steady seepage is achieved with no fluidisation initiated due to sufficiently small orifice pressure.

It is interesting to note that such an evolution pattern is comparable to that of a one-dimensional upward seepage through a single column of spheres (see Figure 5.5). However, a major difference exists in the vertical distribution of excess pore pressures (see Figure 5.6). In the one-dimensional upward seepage flow, the excess pore pressure is linearly distributed with height. While in the case of a locally injected fluid, the excess pore pressures change significantly close to the source of flow, but less so far from it. This

indicates the localisation nature of the locally injected fluid, which was also noted by Alsaydalani (2010) in his experimental results.

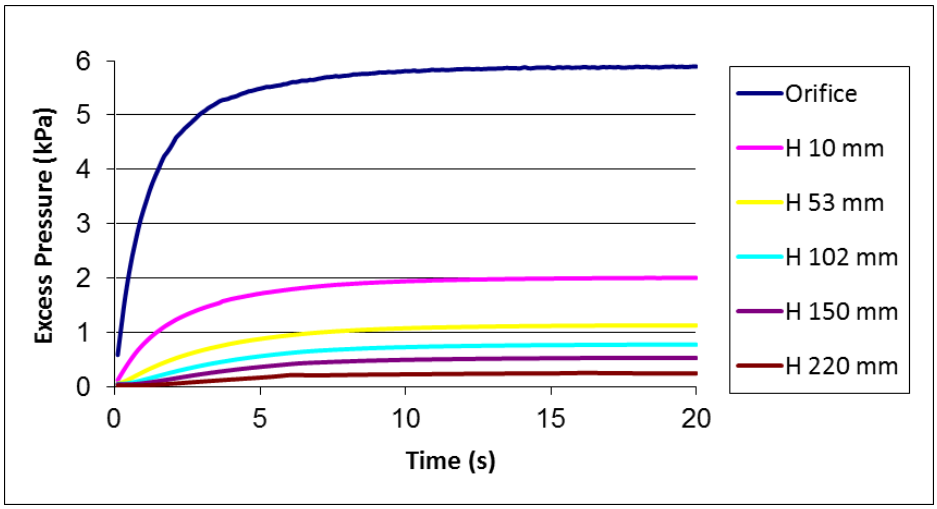

(a) Flow rate = 0.5 l/s

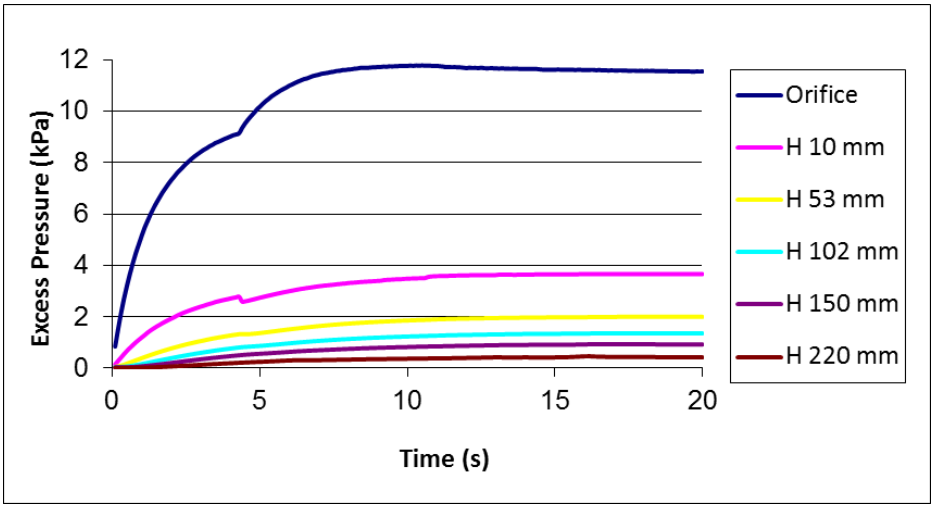

(b) Flow rate = 0.75 l/s

Figure 5.4 p-t curves at different heights directly above the orifice (fixed-bed regime)

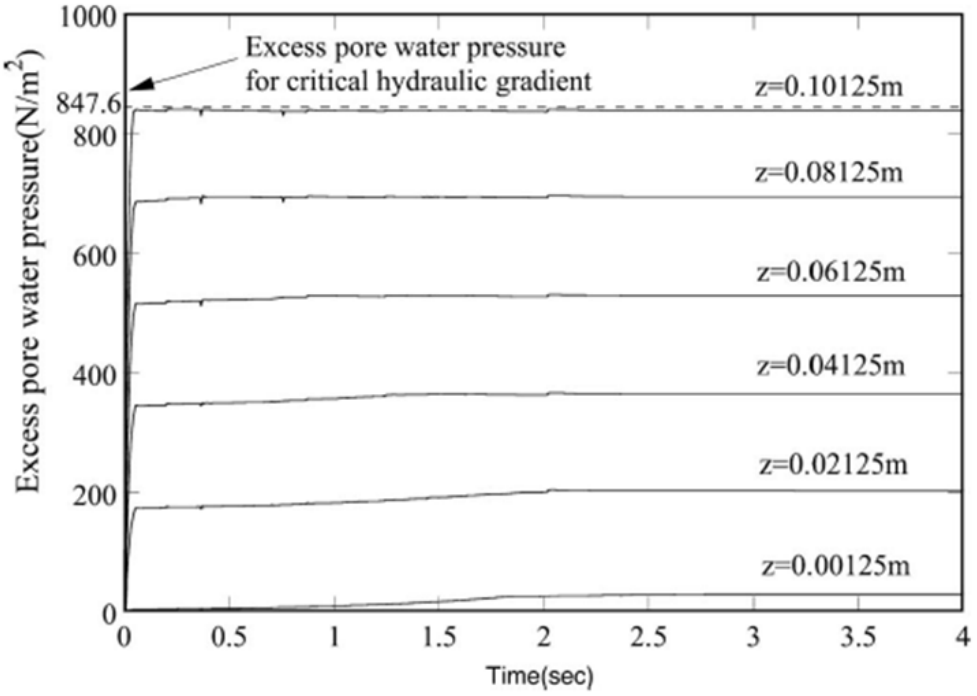

Figure 5.5 p-t curves for a one-dimensional upward seepage flow through a single column of spheres (Suzuki et al., 2007)

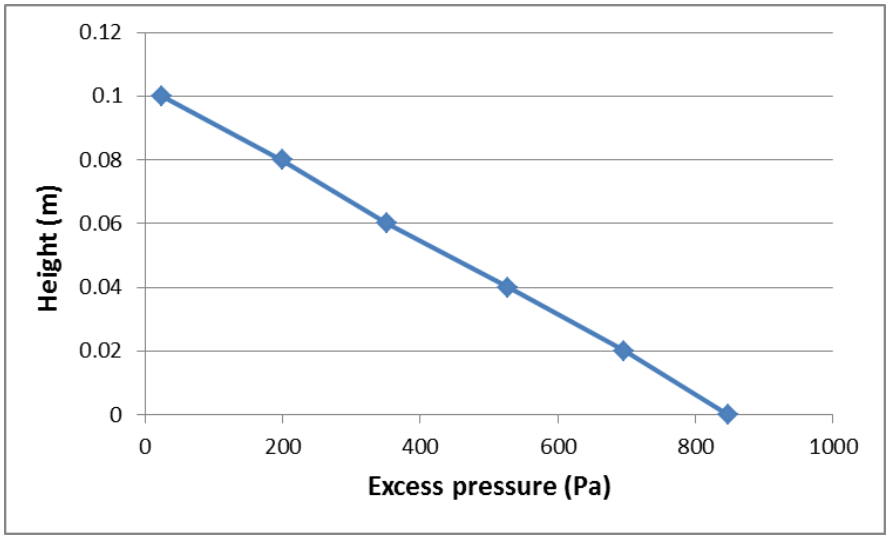

(a) One-dimensional upward seepage flow through a single column of spheres (data from Suzuki et al., 2007)

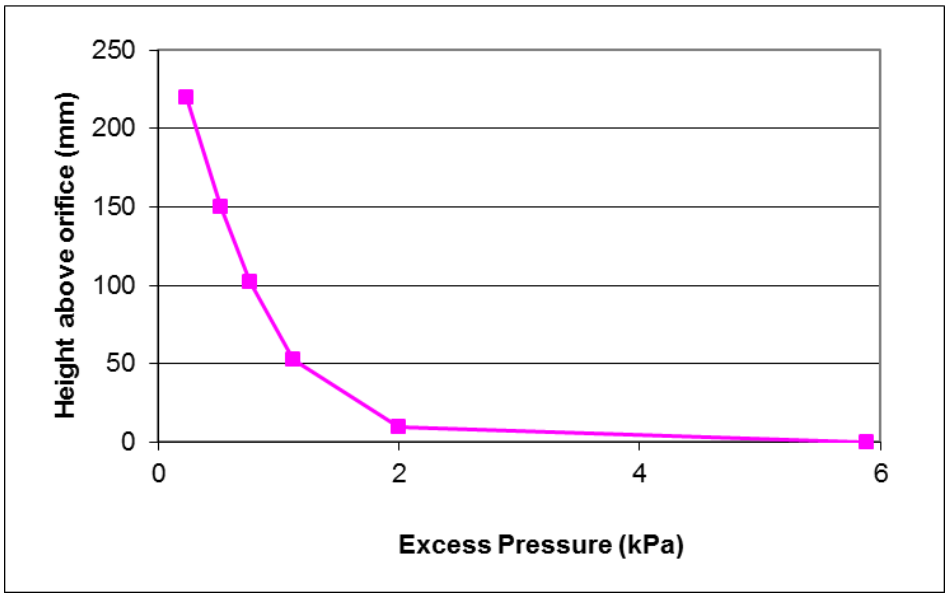

(b) A granular bed subject to a locally injected fluid with seepage mechanism, flow rate = 0.5 l/s

Figure 5.6 Vertical distribution of excess pore pressure in seepage flows

5.3.3 Stable-cavity regime

If greater flow rates are applied, the granular bed responds in a different way. At the beginning of the test, the particles remain immobile. However, as time evolves, soil above the orifice is suddenly lifted up by the incoming fluid, indicating the onset of fluidisation. This also induces a cavity formation at the vicinity of the orifice, and the bed humps in the middle (see Figure 5.3). It is noted that this has also been reported by Alsaydalani (2010) by measuring the vertical increments of the surface profile. Besides, Figures 5.7 and 5.10 demonstrate the corresponding p-t curves using the numerical results. Before fluidisation occurs, the pressures near the source of flow increase more rapidly than those further

away. After peak values are achieved, the pressures near the source of flow undergo a sharp reduction. This is mainly due to the sudden ‘unblocking’ of surrounding soil particles at the onset of fluidisation.

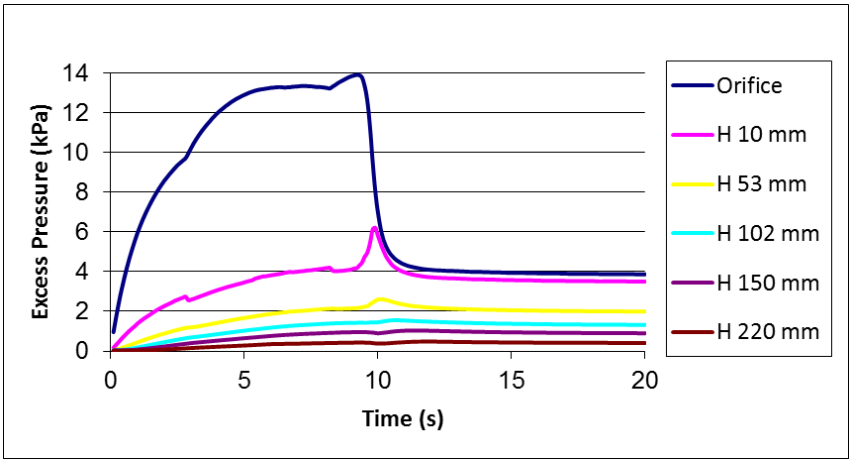

(a) Flow rate = 0.85 l/s

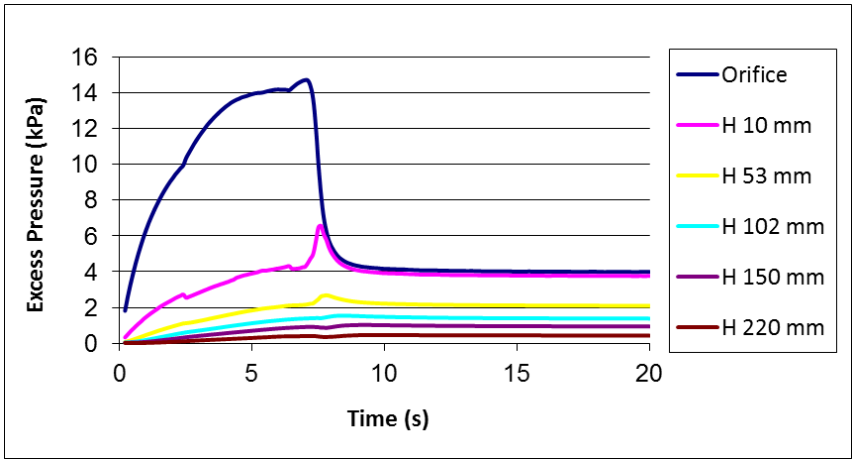

(b) Flow rate = 0.9 l/s

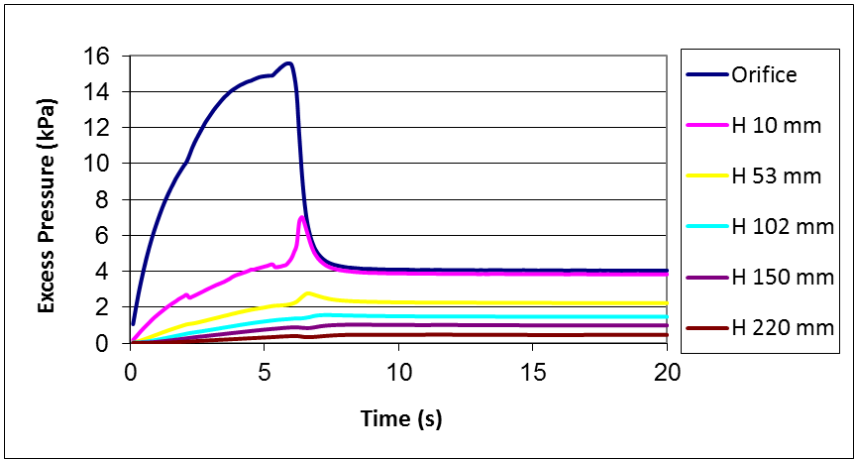

(c) Flow rate = 0.95 l/s

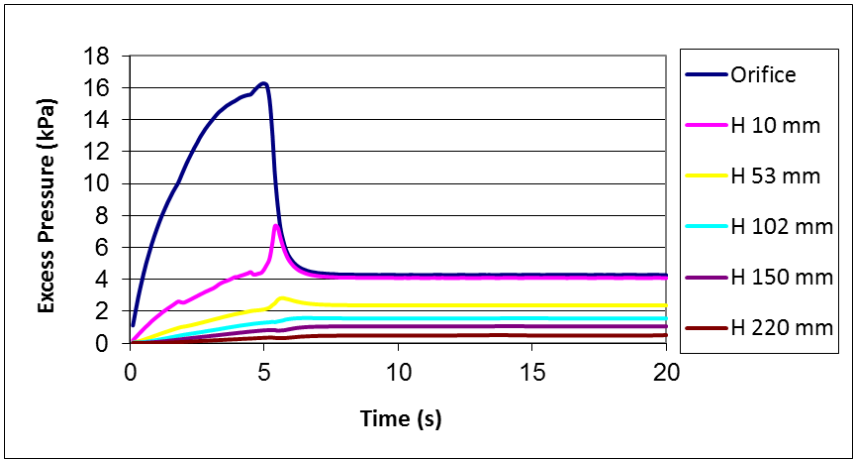

(d) Flow rate = 1.0 l/s

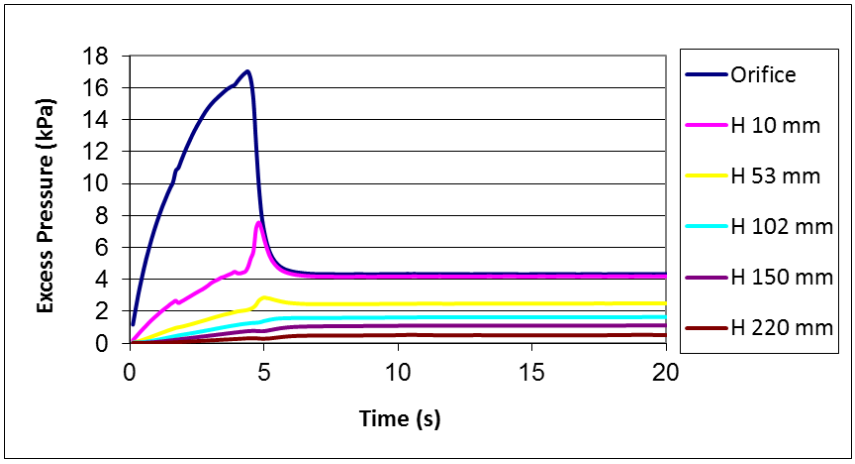

(e) Flow rate = 1.05 l/s

Figure 5.7 p-t curves at different heights directly above the orifice (stable-cavity regime)

Figures 5.8 and 5.9 show the time evolution of cavity size (i.e. V-t curves) with different flow rates applied. It is noted that the cavity reaches a larger size in response to a greater flow rate. Special attention is paid to a narrow range of flow rate between 0.85 l/s and 1.05 l/s where the cavity stops growing in a short period after its formation (see Figure 5.8). It is also worth noting that the V-t curve is closely related to the p-t curve at the orifice. For instance, in the case at a flow rate = 1.0 l/s, a cavity forms at around 4s after the test begins. It then grows gradually for another one second until a sudden increase in its size. Recognised from the corresponding p-t curves (see Figure 5.7(d)), the sudden increase starts at the point when the orifice pressure gets to its peak value. Thereafter, the cavity size is rapidly increased to approximately 440 mm^2 and then remains constant till the end of test. At the same time, the p-t curve for the orifice pressure levels off. From the observations on the particle configuration of the bed, a steady state is identified shortly after the cavity forms. Therefore, the soil bed is regarded to experience the 'stable-cavity regime'. The mechanism associated with this regime is further explored using numerical analysis, which is performed in Chapter 6.

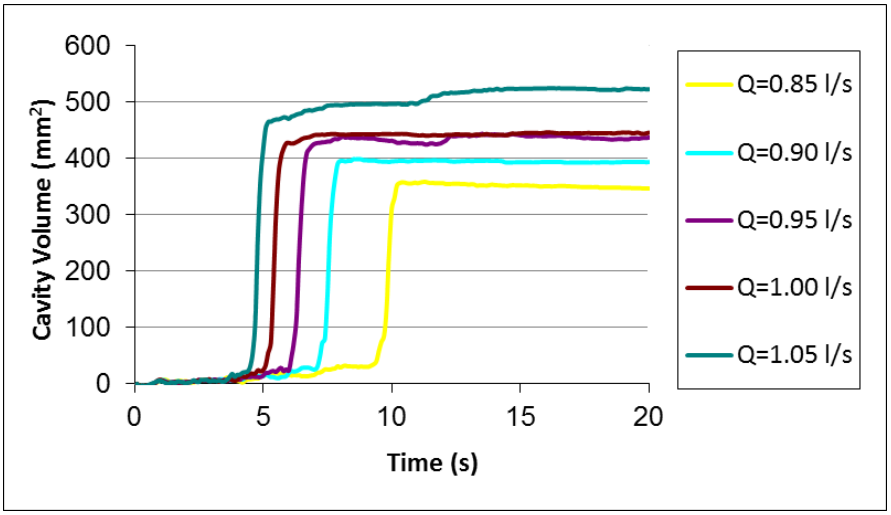

Figure 5.8 V-t curves with different flow rates applied (stable-cavity regime)

5.3.4 Growing-cavity regime

If the applied flow rate is greater than 1.05 l/s, a group of V-t curves indicating a continuously developing cavity are obtained from the numerical results, as shown in Figure 5.9. It is recognised that a greater flow rate leads to an earlier fluidisation and a quicker cavity development. Figure 5.10 also suggests a greater flow rate leads to a higher peak pressure value at the orifice. From Figures 5.9 and 5.10, it is again recognised that the V-t curve is closely related to the p-t curve at the orifice. Once a cavity forms, the p-t curve at the orifice initially undergoes a rapid but significant drop, which is associated with a sharp increase in the cavity size, as identified from the V-t curve. Thereafter, the orifice pressure declines smoothly. The smooth decline corresponds to a continuous cavity development, but at a lower rate (sees Figure 5.9). It is also noticeable that this rate of cavity growth is constant for each case within the test duration. Using the numerical

results obtained, a further analysis for quantifying this continuous cavity development is performed in Chapter 7.

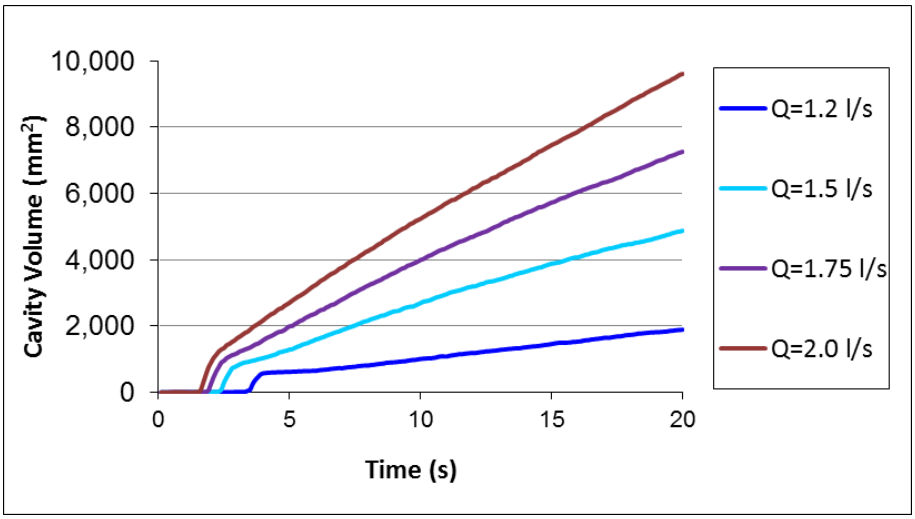

Figure 5.9 V-t curves with different flow rates applied (growing-cavity regime)

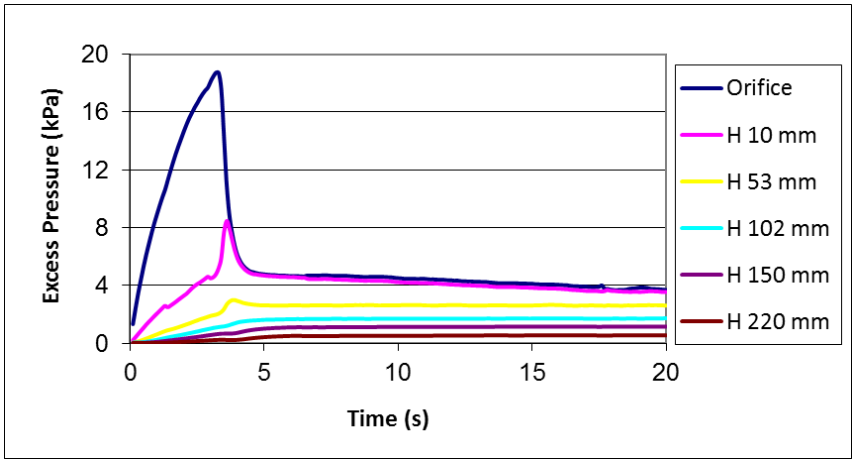

(a) Flow rate = 1.2 l/s

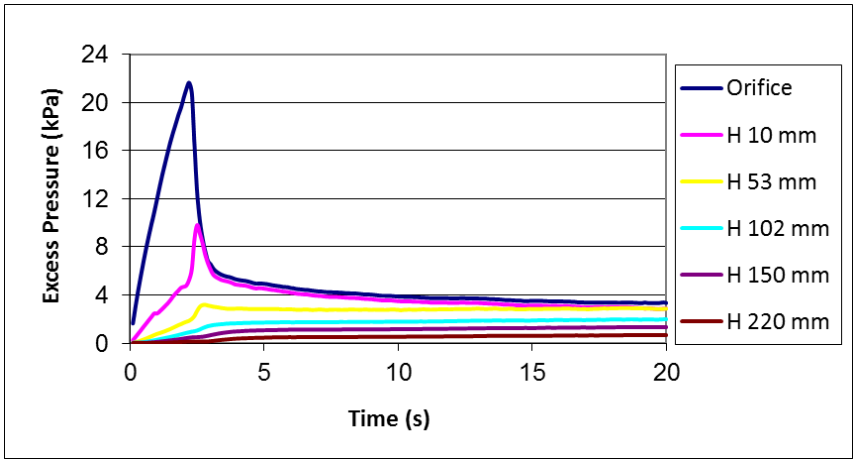

(b) Flow rate = 1.5 l/s

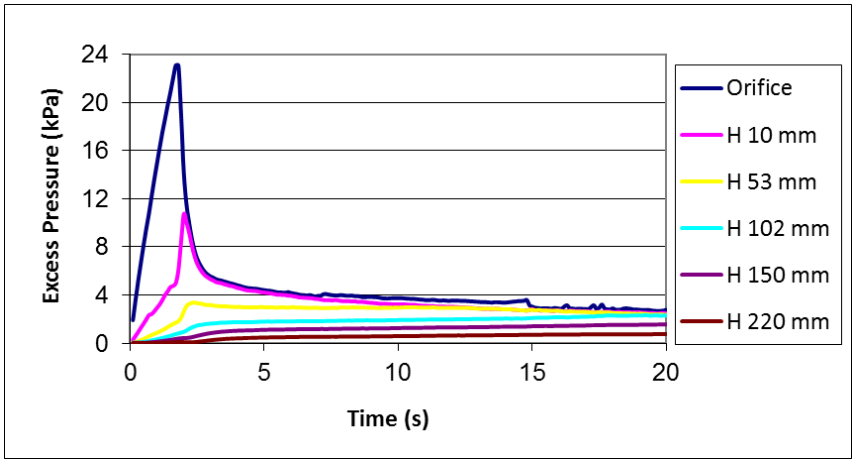

(c) Flow rate = 1.75 l/s

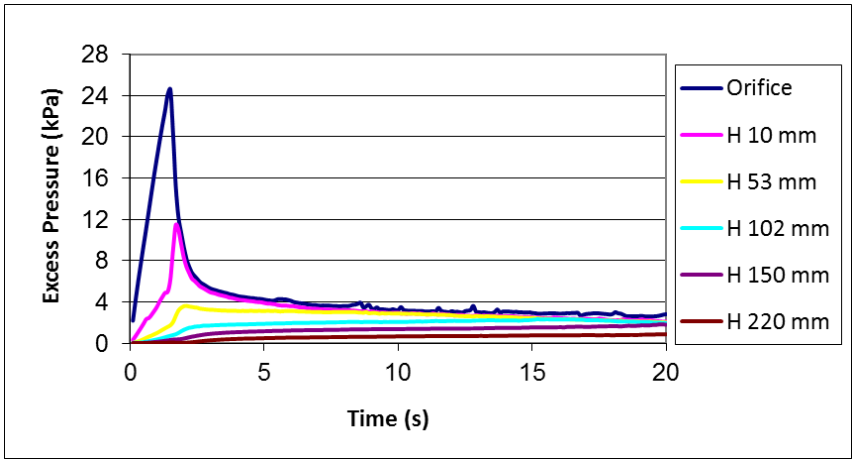

(d) Flow rate = 2.0 l/s

Figure 5.10 p-t curves at different heights directly above the orifice (stable-cavity regime)

5.3.5 Blow-out regime

If the applied flow rate is very high (i.e. exceeding 2.0 l/s with the current model parameters), the cavity keeps growing up to the bed surface so as to open up a fluid channel as a 'chimney flow' (see Figure 5.11). Such a case is referred to as a 'blow-out' failure. From Figure 5.11, it is noted that the cavity develops with an unsymmetrical pattern about the central axis of the bed. This can be attributed to the non-zero horizontal momentum of the fluid as it is injected with a horizontal velocity from right to left in the pipe. This can also be due to the fact that the bed is not really symmetric and the system is unstable, hence any small difference will be amplified.

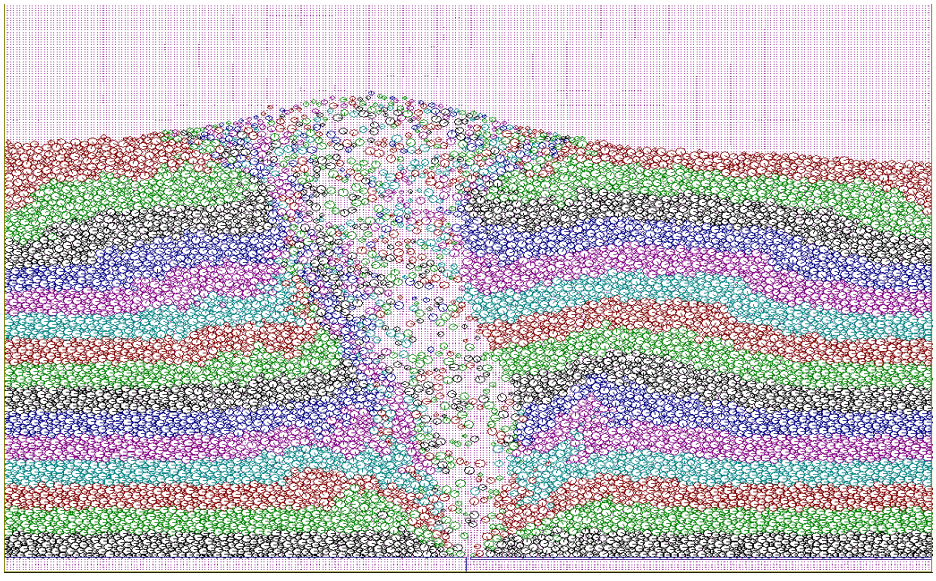

Figure 5.11 An example of blow-out failure, flow rate = 4.0 l/s, and t = 19s

In the corresponding p-t curves (see Figure 5.12), the excess pressures at deeper locations may become equal to the pressures near the bed surface (see Figures 5.12(a)-(c)).

Alternatively, the orifice pressure may even increase after the cavity forms (see Figure 5.12(d)). This is attributed to an extremely rapid energy input by a very high flow rate. The fluctuation in pressures is also noticed in the p-t curves, indicating unsteady flow behaviour. In addition, excess pressures at shallower locations are occasionally greater than those at deeper ones, suggesting backward flows and local vortices.

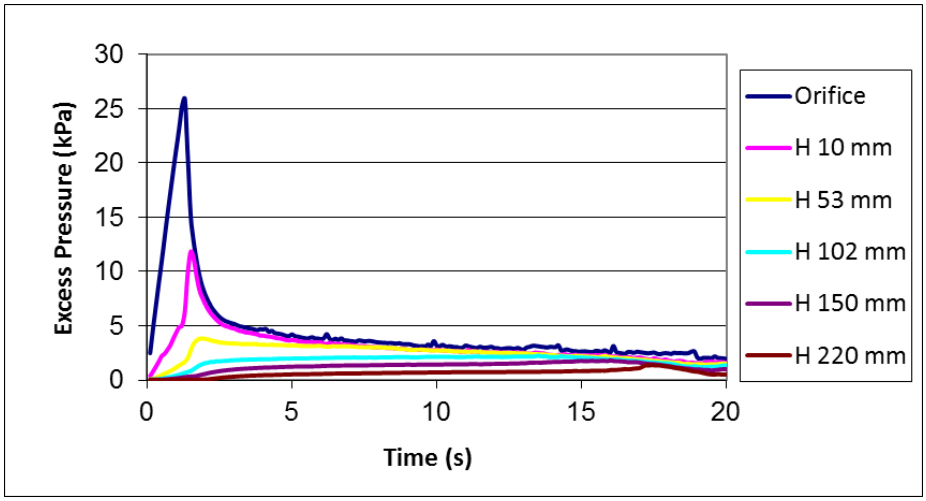

(a) Flow rate = 2.25 l/s

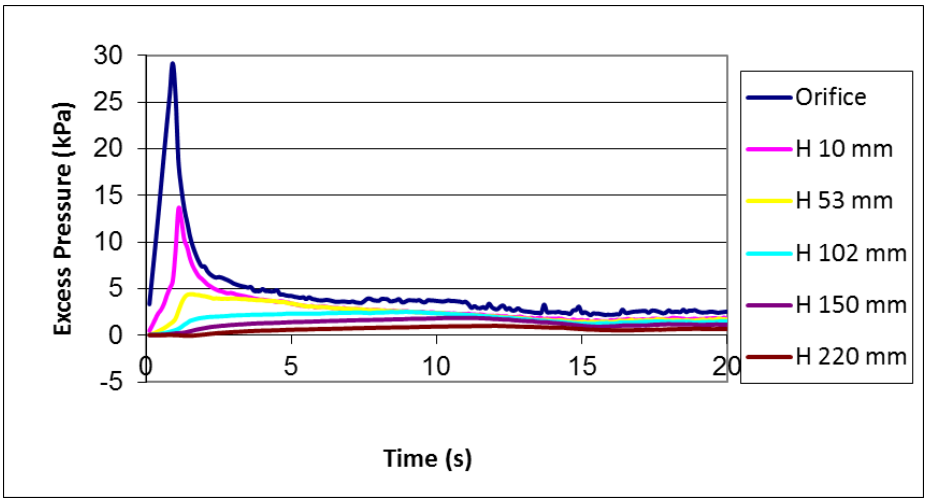

(b) Flow rate = 3.0 l/s

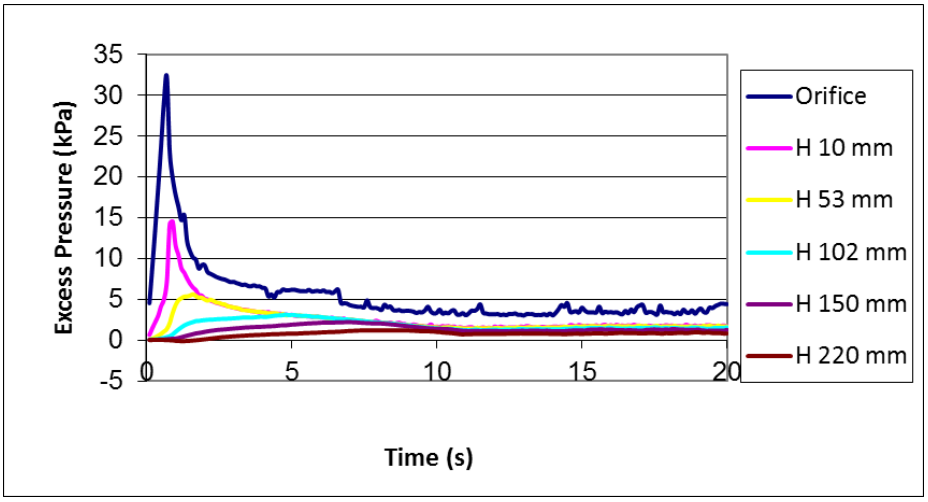

(c) Flow rate = 4.0 l/s

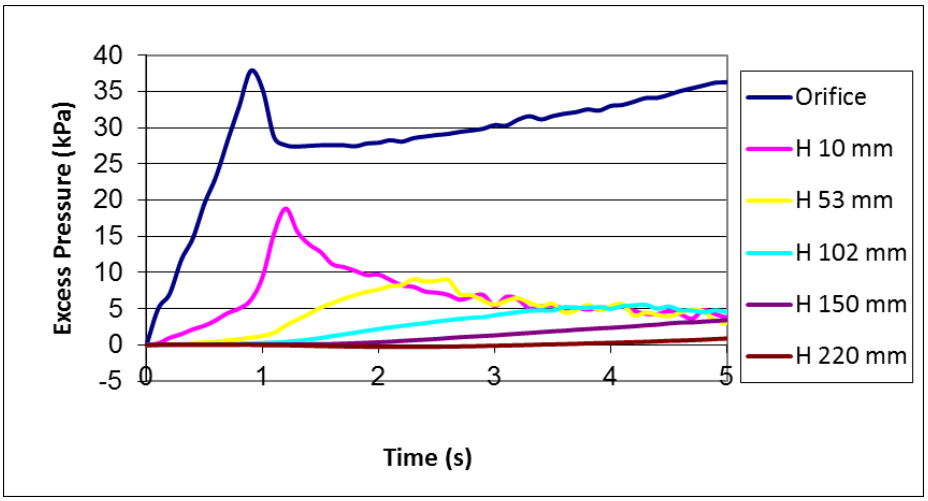

(d) Flow rate = 6.0 l/s

Figure 5.12 p-t curves at different heights directly above the orifice (blow-out regime)

As suggested by the p-t curves presented in this section, pore pressures within the soil near the leaking area may undergo a significant increase before fluidisation occurs. This implies a local loss of bearing capacity since the effective stress suffers a considerable reduction. It is regarded even more dangerous that such a significant problem takes place where it is not easily observed from above the ground.

5.4 Onset of Fluidisation

As stated in Section 2.2, Alsaydalani (2010) obtained some valuable findings on the onset of fluidisation. Therefore, in this section, a comparison between the numerical results and the experimental findings is conducted.

5.4.1 Excess pore pressure vs. flow rate

Figure 5.13 demonstrates how the excess pore pressures at different heights change with flow rate. It is found out that the numerical solutions agree well with the experimental results qualitatively. Both findings illustrate that, at the vicinity of the orifice, the excess pore pressure grows up to a peak point with the increase in the flow rate. Beyond this point, the pore pressure undergoes a sharp reduction as flow rate further increases. This sharp reduction indicates that fluidisation occurs so that pore pressure near the source of flow dissipates due to the 'unlocking' of particles. For instance, in the experimental work by Alsaydalani (2010), fluidisation was initialised when the flow rate was increased beyond the value of 1042 l/h (i.e. 0.289 l/s) which led to a peak value in the pore pressure at height of 10mm (see Figure 5.13(a)). Similarly, the onset of fluidisation is firstly observed in the numerical test when flow rate exceeds 0.8 l/s at which the orifice pressure reaches its maximum (see Figure 5.13(b)).

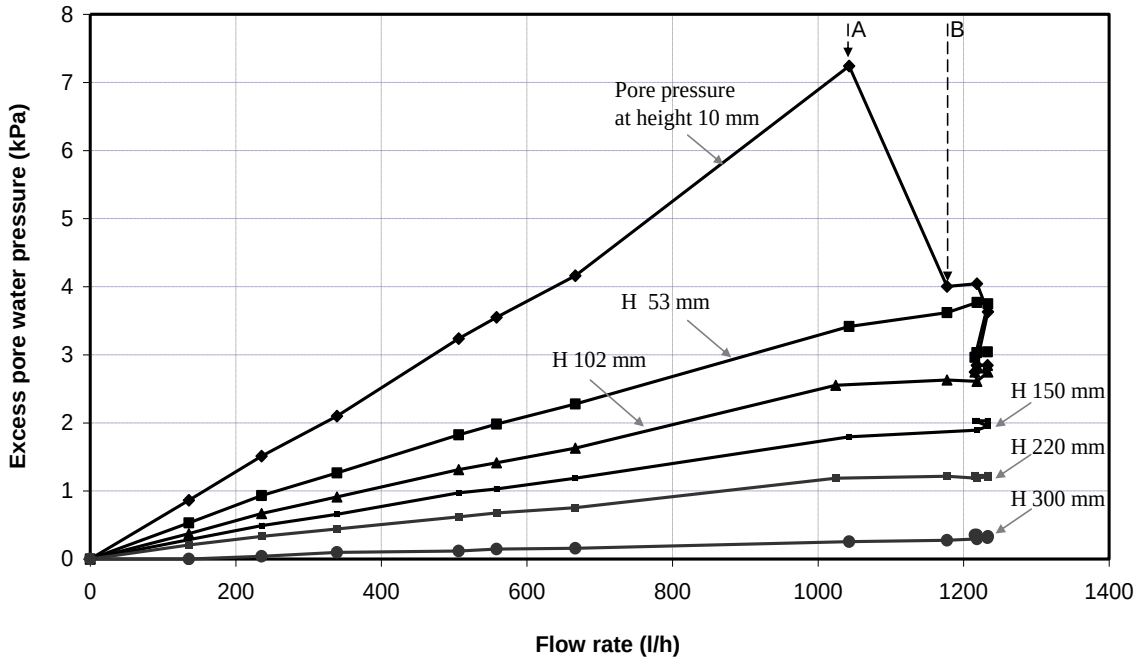

(a) Experimental results (Alsaydalani, 2010)

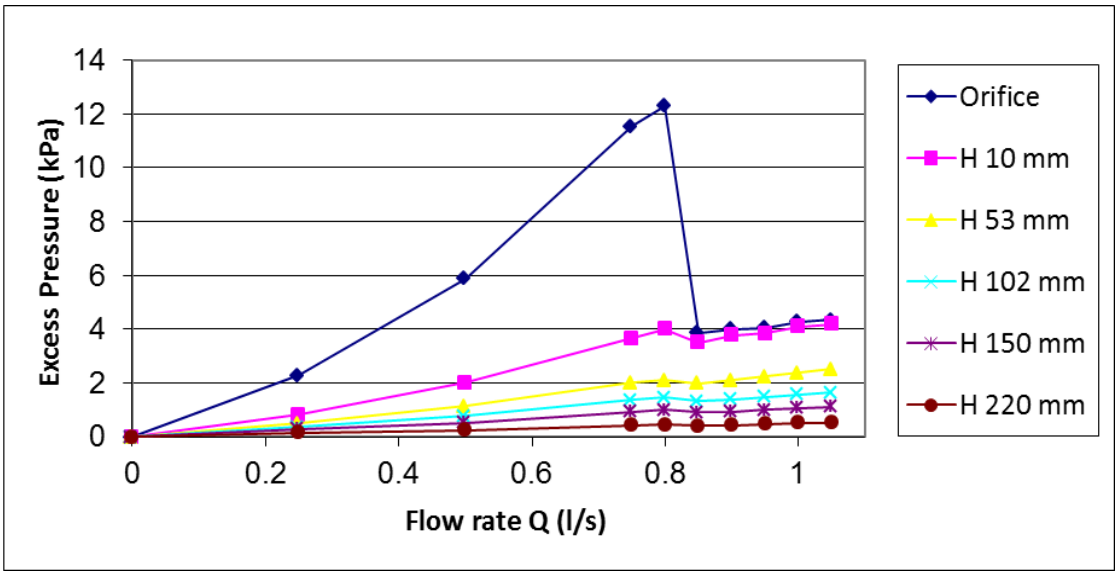

(b) Numerical results

Figure 5.13 Excess pore pressures at different heights as a function of flow rate

However, in the areas far from the orifice, the excess pore pressures accumulate much

slower with the increase in flow rate. Beyond the flow rate at which the pressure near the orifice reaches its peak point, pressures far from the source of flow may only have a slight drop, as shown in the numerical solutions (see Figure 5.13(b)), while remain at an approximately steady value as indicated by the experimental results (see Figure 5.13(a)). The difference is considered as a result of different frequency of data acquisition. In spite of such a difference, both numerical and experimental data suggest that a more obvious change in excess pore pressures takes place at an area closer to the source of flow. This is regarded as the localisation nature due to the locally injected fluid.

5.4.2 Vertical distribution of excess pore pressure

The same set of data is plotted to show the vertical distribution of the excess pore pressure directly above the orifice with different flow rates (see Figure 5.14(b)). Again, it agrees well with the experimental results qualitatively (Figure 5.14(a)). It is recognised the excess pore pressure is not linearly distributed in the vertical direction, as mentioned in Section 5.3.2. This is attributed to the concentration of pore pressure at the source of flow. The peak point in Figure 5.13 can also be identified from the most significant pressure gradient at the vicinity of the orifice shown in Figure 5.14.

With the flow rate increases, the build-up of pressure gradient is initially seen from the results until it reaches to its maximum. Thereafter, excess pressures near the source of

flow drop significantly as the flow rate is further increased. This indicates that internal fluidisation occurs. Alsaydalani (2010) pointed out that the critical hydraulic gradient in the internal fluidisation was greater than that of a normal seepage failure which is about one according to Terzaghi's hydraulic failure theory. This finding is also demonstrated from the numerical results by drawing a line indicating the unity hydraulic gradient (see Figure 5.14 (b)).

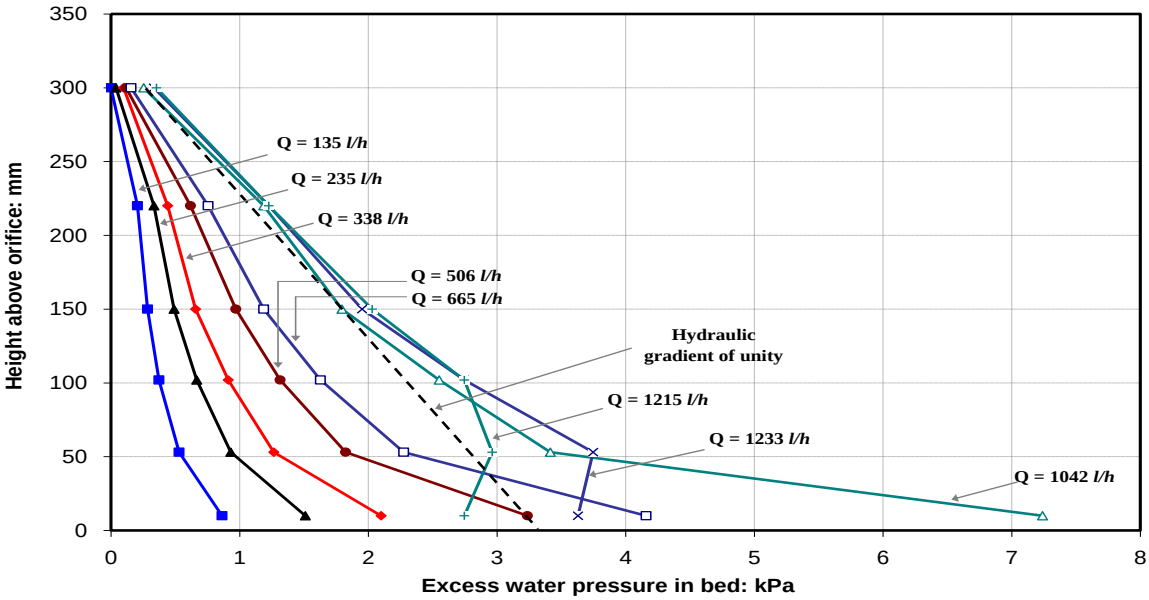

(a) Experimental results (Alsaydalani, 2010)

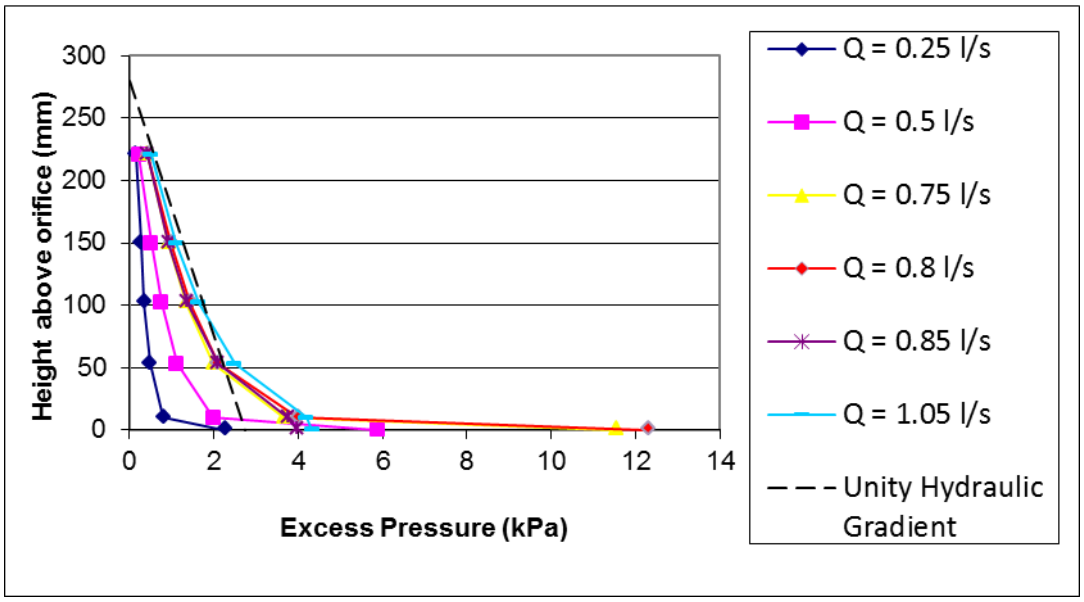

(b) Numerical results

Figure 5.14 Vertical distribution of excess pore pressure directly above the orifice with different flow rates

5.4.3 Fluidised zone and uplifting zone

As stated in Section 5.3.3, a sudden cavity formation indicates the onset of fluidisation. By observing the particle configuration from the numerical results, the cavity is viewed as a fluidised zone where particles are mobilised and moving freely with the injecting fluid (see Figure 5.15). This was also recognised by Alsaydalani (2010) as an 'internally fluidised zone'. Moreover, in agreement with his experimental findings, an uplifting zone with an inverted tapered shape is observed from the numerical results, as shown in Figure 5.16. It can be interpreted that, at the onset of fluidisation, the particles within the uplifting zone are being raised while those outside the zone remain steady. The wedge

angle measured from the experiments was in the order of 63.9°, of which the influencing factors could not be easily identified. While the numerical simulations show a common angle of 62°, which is slightly smaller than that given by experiments. This difference may be attributed to two main reasons. The first one is denoted as the error in image analysis, as the angle would slightly change by rotating the line enveloping the uplifting zone. In the particle displacement plots, however, defining the line could be dependent on personal skill of colour discrimination. Besides, the circular-shaped particles adopted in the numerical tests tend to demonstrate a smaller friction angle in the soil. In spite of such a small difference, the wedge angle obtained by numerical simulations is reasonably similar with that measured from the experiments.

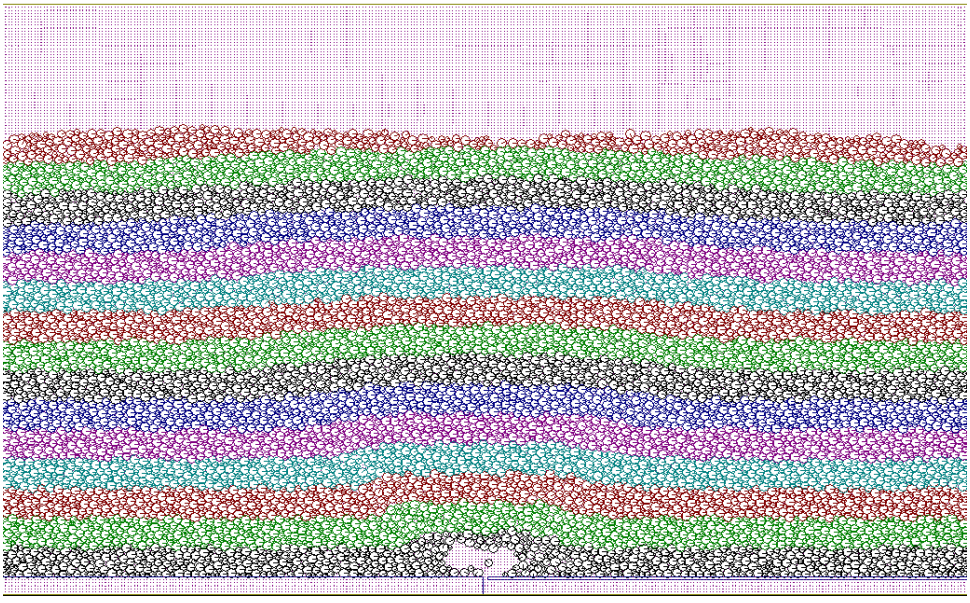

Figure 5.15 A snapshot of particle configuration of the bed: particles are mobilised and moving freely within the fluidised zone, flow rate = 1.2 l/s and t = 18.0 s

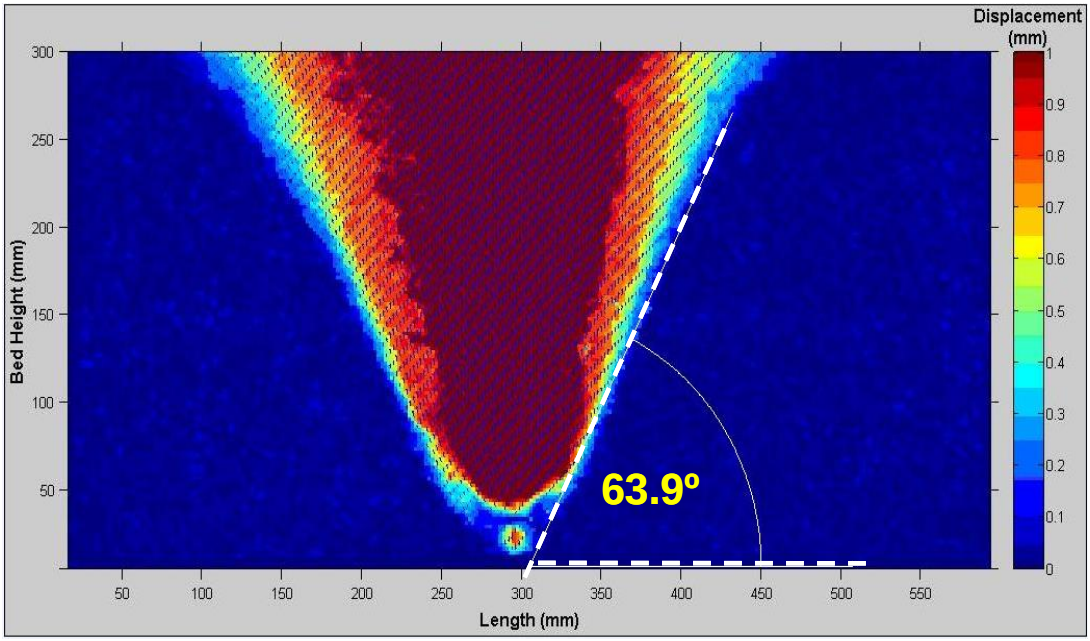

(a) Experimental results, flow rate = 1177 l/h (Alsaydalani, 2010)

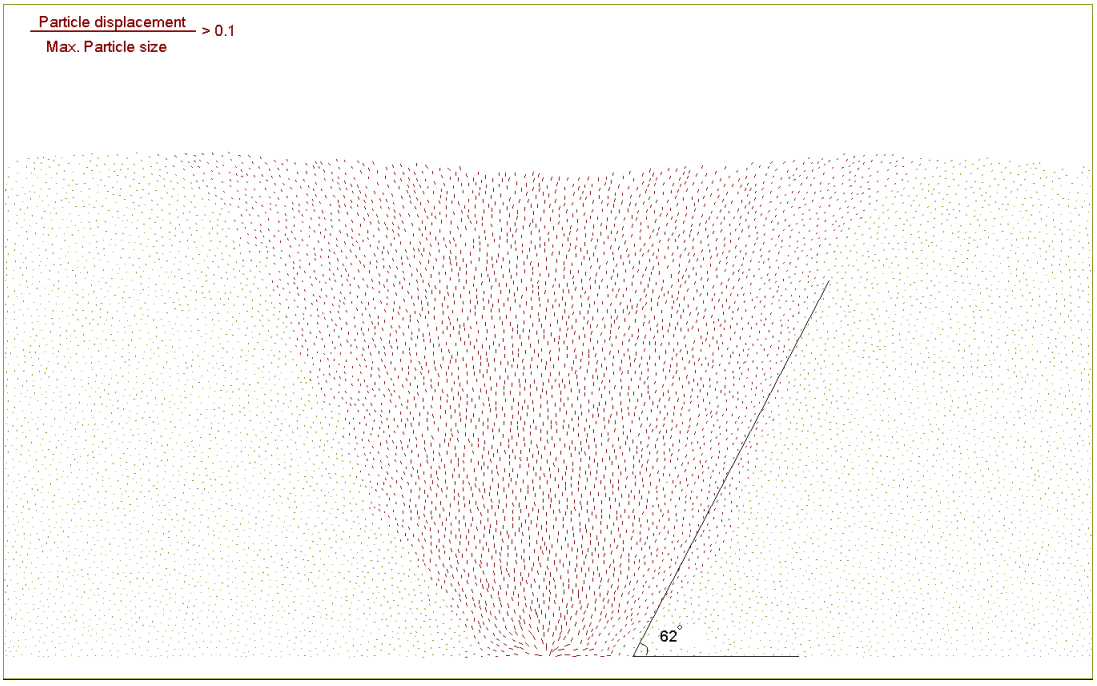

(b) Numerical results, flow rate = 0.9 l/s and t = 7.7 s

Figure 5.16 Particle displacement plot: uplifting zone and wedge angle

From the comparisons carried out in this section, it is seen that the current numerical

model using *FPS-BHAM* is capable of simulating the fundamental phenomena associated with the onset of fluidisation. The computational outcome agrees well with the experimental findings qualitatively. Furthermore, for a quantitative analysis with the numerical results, the following section provides a more in-depth investigation into the fluidising mechanism.

5.5 Fluidising Mechanism

5.5.1 Different fluid flow distributions

In Alsaydalani (2010), it was revealed and evidenced that, at the onset of fluidisation, a force balance is achieved between the upward drag force applied to the uplifting wedge and its bulk weight. The underlying mechanism is recognised to be consistent with that of the partial fluidisation in a tapered fluidised bed (Shi et al., 1984; and Peng and Fan, 1997). And the detailed theoretical derivation has been presented in Alsaydalani (2010).

In all the above models used for studying the mechanism, an assumption was made that the fluid flows are uniformly distributed in the horizontal direction at the onset of fluidisation, with only vertical velocities exist (see Figure 5.17). However, this is not exactly true in a real soil subject to a local leakage. As argued by Alsaydalani (2010), the leaking fluid shall be spreading radially although no further evidence was provided by his results.

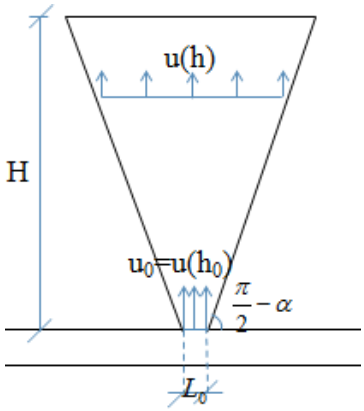

Figure 5.17 Sketch of vertical flow distribution within the wedge

With the aid of numerical simulation using *FPS-BHAM*, it is easy to identify a radial flow distribution from the pressure contour plot (see Figure 5.18). The concentric half-circles indicate a radial flow field before fluidisation occurs. This would lead to a different analytical expression of the flow equation, and hence the upward drag force calculations. Therefore, in Section 5.5.2, a modified flow equation is deduced, which results in a different analytical solution to fluidising pressure. Moreover, the predicted fluidising pressures are then compared with the measured ones in Section 5.5.3 so that a further validation of the numerical model can be accomplished.

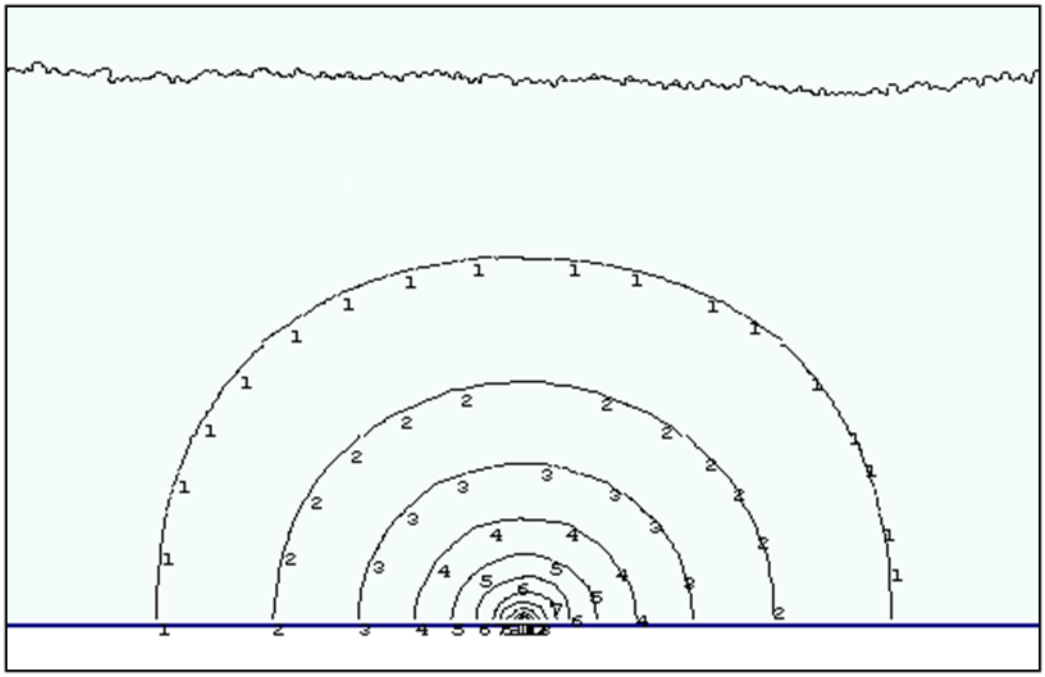

Figure 5.18 Pressure contour before fluidisation (scaled down to make the maximum represented as 10)

5.5.2 Fluidising pressure for a radial flow distribution

Figure 5.19 shows a simple sketch of the radial flow distribution in the uplifting wedge. The superficial velocity is assumed uniformly distributed along the circumferential direction. As the flow rate is constant at each half-circular shaped cross-sectional area, the superficial velocity at a distance of r from the middle of the orifice can be calculated as

$$u(r) = \frac{u_0 r_0}{r} = \frac{C_r}{r} \tag{5.1}$$

in which u_0 is the superficial velocity at the orifice, and C_r is linearly related to flow

rate and is a constant along the radial direction. The orifice size is equal to $2r_0$.

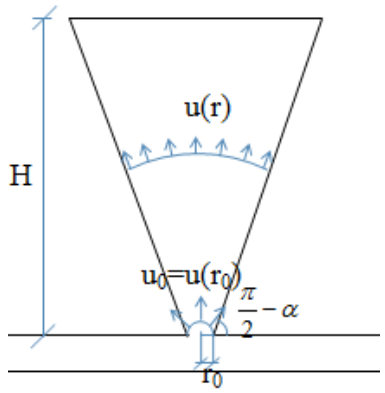

Figure 5.19 Sketch of radial flow distribution within the wedge

As stated in Section 2.2, the Ergun's flow equation through a packed bed has been proved valid before fluidisation occurs. In the case with a radial flow distribution, the Ergun's equation is written as

$$(-dP) = (Au + Bu^2)dr \tag{5.2}$$

where $(-dP)$ stands for the pressure drop across a differential radial dr. A and B can be calculated by

$$A = 150\frac{(1-\varepsilon_0)^2}{\varepsilon_0{}^3}\frac{\mu_f}{(\phi_s d_p)^2} \tag{5.3}$$

and

$$B = 1.75\frac{(1-\varepsilon_0)}{\varepsilon_0{}^3}\frac{\rho_f}{\phi_s d_p} \tag{5.4}$$

where ε_0, μ_f, ρ_f, ϕ_s, and d_p are the initial porosity of the bed, the fluid viscosity and density, the particle sphericity and diameter, respectively.

By substituting Eqn.(5.1) into Eqn.(5.2) and integrating Eqn.(5.2) along the radial direction, the flow equation in the wedge can be deduced,

$$(-\Delta P) = \int (Au + Bu^2)dr = \int (AC_r \frac{1}{r} + BC_r{}^2 \frac{1}{r^2})dr = AC_r \ln r - BC_r{}^2 \frac{1}{r} + const.$$

when $r = H$, $(-\Delta P) = 0$. Hence,

$$const. = -AC_r \ln H + BC_r{}^2 \frac{1}{H},$$

where H is the wedge height. And the flow equation before fluidisation occurs is expressed as

$$(-\Delta P) = AC_r \ln \frac{r}{H} + BC_r{}^2 (\frac{1}{H} - \frac{1}{r}) \tag{5.5}$$

Therefore, the pressure drop through the bed is calculated as

$$\Delta P_{\max} = AC_r \ln \frac{H}{r_0} + BC_r{}^2 (\frac{1}{r_0} - \frac{1}{H}) \tag{5.6}$$

in which the minus sign on the left is taken off so that an upward pressure drop is denoted positive in the following calculations.

The upward drag force F applied to the wedge can be approximately calculated as

$$\begin{aligned} F &= \int_{r_0}^{H} (Au + Bu^2) 2\alpha_w r \omega_0 dr \\ &= \int_{r_0}^{H} (2\alpha_w r \omega_0 A \frac{C_r}{r} + 2\alpha_w r \omega_0 BC_r{}^2 \frac{1}{r^2}) dr \\ &= 2\alpha_w \omega_0 AC_r (H - r_0) + 2\alpha_w \omega_0 BC_r{}^2 \ln \frac{H}{r_0} \end{aligned} \tag{5.7}$$

where ω_0 is the thickness of the wedge. α_w is the complement of the measured wedge

angle.

On the other hand, the submerged weight of the wedge W is

$$W = (L_0 + H\tan\alpha_w)H\omega_0(\rho_p - \rho_f)g(1-\varepsilon_0) = (L_0 + H\tan\alpha_w)H\omega_0 T \qquad (5.8)$$

in which L_0 is the orifice size, and hence $L_0 = 2r_0$. ρ_p is the particle density, and g is the gravitational acceleration. T denotes the volumetric submerged weight of the wedge.

According to Alsaydalani (2010), internal fluidisation due to a locally injected fluid is activated when a force balance between the upward drag force and the wedge weight is achieved:

$$F = W \qquad (5.9)$$

Substituting Eqns.(5.7) and (5.8) into Eqn.(5.9), one can obtain

$$2\alpha_w AC_r(H - r_0) + 2\alpha_w BC_r^{\,2}\ln\frac{H}{r_0} = (L_0 + H\tan\alpha_w)HT \qquad (5.10)$$

Combined Eqn.(5.10) with Eqn.(5.6), the pressure drop through the wedge required to initialise fluidisation, i.e. the fluidising pressure Δp_f, can be predicted as

$$\Delta p_f = [(\frac{1}{r_0} - \frac{1}{H}) - \frac{(\ln H - \ln r_0)^2}{H - r_0}]\cdot BC_r^{\,2} + \frac{\ln(\frac{H}{r_0})(L_0 + H\tan\alpha_w)HT}{2\alpha_w(H - r_0)} \qquad (5.11)$$

5.5.3 Measured vs. predicted fluidising pressure

In an effort to compare the measured fluidising pressures with the predicted ones, numerical tests are conducted on a series of bed samples with different heights. In this sub-section, the numerical model is further calibrated by adopting the cumulative beta distribution of particle size, as it provides double-curved shape which is usually identified for the particle size distribution in real soil (Voivret et al., 2007; and Mansouri et al., 2009). In all tests, the particle size ranges from 3 mm to 6 mm. Table 5.2 lists the particle number of each size adopted in different bed samples. The numerical tests are conducted under the controlled pressure in the pipe so as to easily capture the exact value of fluidising pressure.

For the initial 40,000 DEM-LBM calculation cycles (i.e., 4s), the particles are artificially kept from moving. This aims to achieve a well-developed flow in bed. The particles are then allowed to move after 4s. Different behaviours are obtained from the numerical results with various controlled pressures applied, and this is further illustrated and discussed in Section 7.3. It is recognised that, although fluidisation can be activated, a steady state is approximately achieved in excess pore pressures during the initial 40,000 cycles. And such a distribution shall satisfy the Ergun's flow equation derived as Eqn.(5.5). If taken the upward pressure drop as positive, Eqn.(5.5) is rewritten as

$$\Delta P = AC_r \ln\frac{H}{r} + BC_r^{\,2}\left(\frac{1}{r} - \frac{1}{H}\right) \tag{5.12}$$

Table 5.2 Particle number of each size for different bed samples

Particle size (mm)	$H = 340mm$	$H = 380mm$	$H = 420mm$	$H = 470mm$	$H = 500mm$
3.00	0	0	0	0	0
3.25	330	363	401	448	496
3.50	914	1003	1107	1240	1373
3.75	1380	1516	1673	1873	2073
4.00	1730	1900	2097	2348	2599
4.25	1963	2156	2380	2664	2950
4.50	2080	2285	2521	2822	3125
4.75	2080	2285	2521	2822	3125
5.00	1963	2156	2380	2664	2950
5.25	1730	1900	2097	2348	2599
5.50	1380	1516	1673	1873	2073
5.75	914	1003	1107	1240	1373
6.00	330	363	401	448	496
Total No.	16794	18447	20356	22791	25232

Figure 5.20 shows the excess pressure directly above the orifice against ln(1/r) at the steady state.

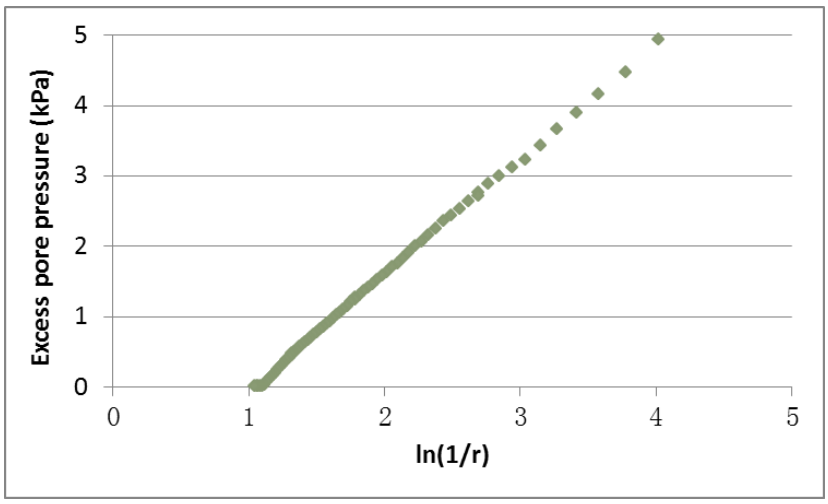

(a) bed height = 340mm, controlled pressure = 14kPa

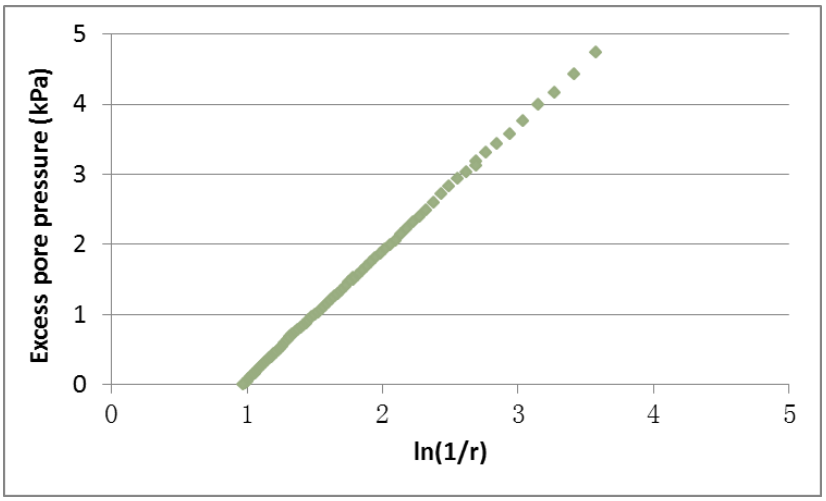

(b) bed height = 380mm, controlled pressure = 15kPa

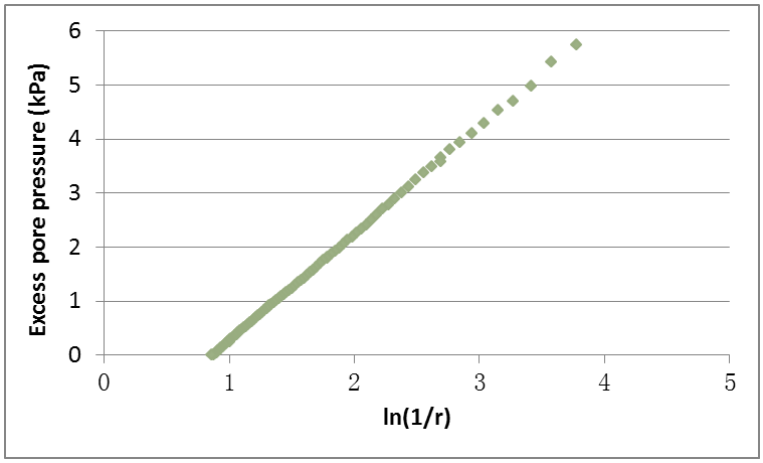

(c) bed height = 420mm, controlled pressure = 17kPa

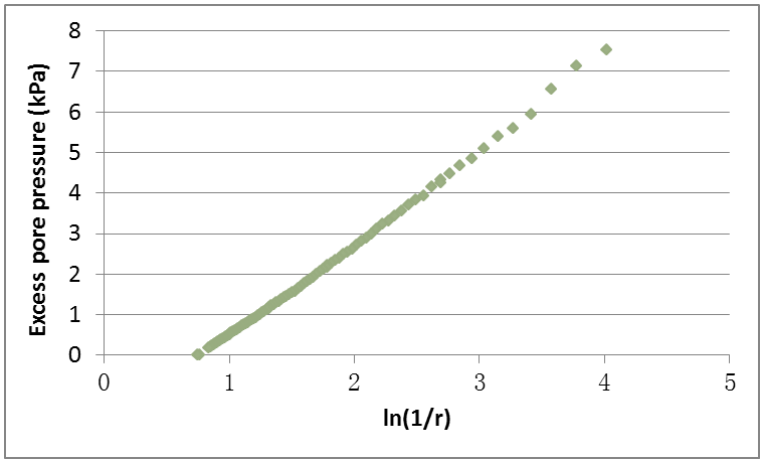

(d) bed height = 470mm, controlled pressure = 20kPa

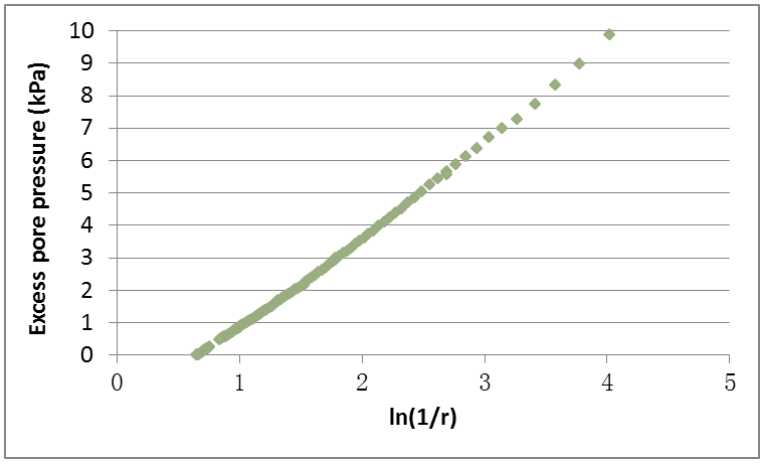

(e) bed height = 500mm, controlled pressure = 22kPa

Figure 5.20 Excess pore pressure directly above the orifice vs. ln(1/r) at the steady state

Figure 5.20 indicates a linear relationship between the steady pressure and ln(1/r). From Eqn.(5.12), it can be further recognised that the superficial velocity is so small that the impact of its second order on seepage can be neglected, hence the flow is primarily dominated by the first order of the superficial velocity. Therefore, with the current model parameters, Eqn.(5.11) can be simplified by neglecting its first term,

$$\Delta p_f = \frac{\ln(\frac{H}{r_0})(L_0 + H\tan\alpha_w)HT}{2\alpha_w(H - r_0)} \tag{5.13}$$

For all the tested bed samples, a comparison between the numerically measured fluidising pressures and the predicted ones by Eqn.(5.13) is shown in Figure 5.21. It is found out that a good agreement is achieved between them.

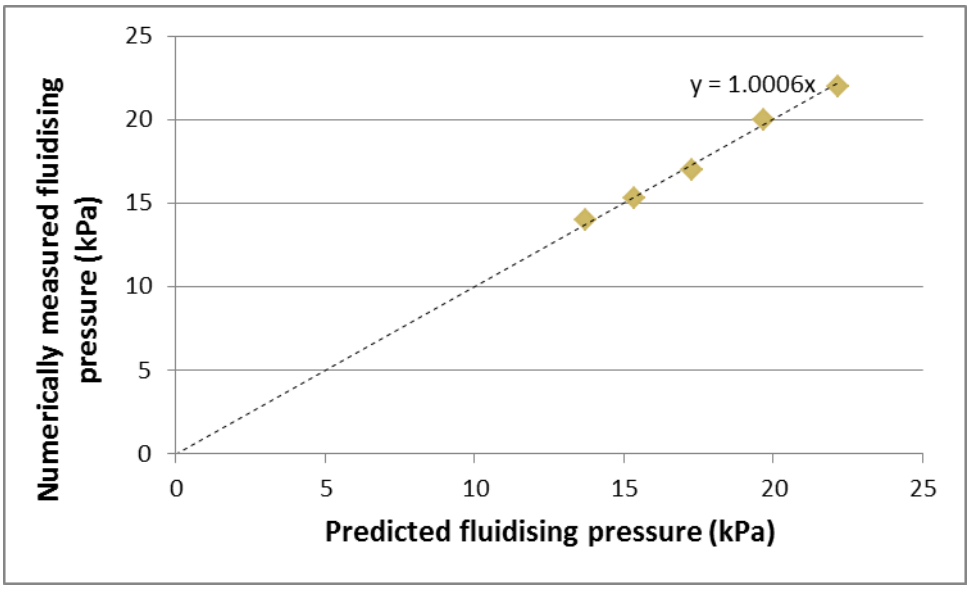

Figure 5.21 Numerically measured fluidising pressure vs. predicted fluidising pressure

Besides, as $r_0 << H$ and $L_0 = 2r_0$, Eqn.(5.13) can be further simplified as

$$\Delta p_f = \frac{\ln(\frac{2H}{L_0})(L_0 + H\tan\alpha_w)T}{2\alpha_w} \tag{5.14}$$

And since $L_0 << H$, it can approximately be obtained that, for a given bed material,

$$\Delta p_f \propto H \ln(\frac{2H}{L_0}) = H' \tag{5.15}$$

where H' can be viewed as an equivalent height deduced for a granular bed subject to a locally injected fluid, which is analytically proportional to the fluidising pressure for a given bed material.

Figure 5.22 indicates the agreement on Eqn.(5.15) by the numerical results.

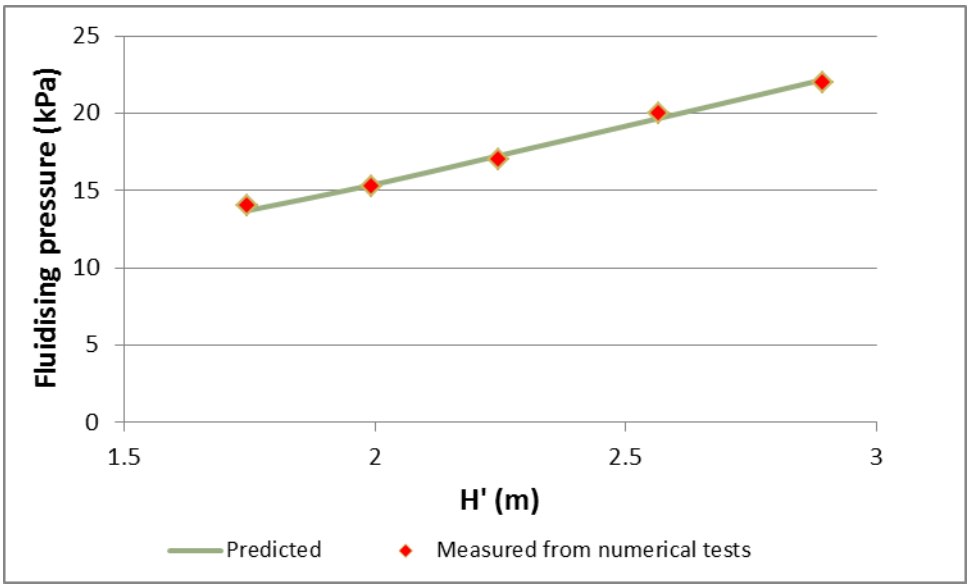

Figure 5.22 Fluidising pressure vs. H'

5.6 Summary

In this chapter, the capability of a numerical model using *FPS-BHAM* in simulating internal fluidisation due to a local leakage is validated. With the aid of numerical simulation, different regimes of bed behaviour under various flow rates are obtained.

With the controlled flow rate progressively increased among tests, the bed sequentially undergoes the following behaviours: (i) the fixed-bed regime; (ii) the stable-cavity regime; (iii) the growing-cavity regime; and (iv) the blow-out regime. The findings on the bed behaviours are evidenced by previous experimental studies (Zoueshtiagh and Merlen, 2007; Royal et al., 2008; and Alsaydalani, 2010).

Observed from the numerical results, the main findings on each bed regime are firstly demonstrated in this chapter, including:

- Excess pressures directly above the orifice initially accumulate before they level off. This indicates that the steady seepage prevails with no fluidisation being initiated. A greater excess pressure is generated at a deeper location, where it is closer to the source of flow. The pressure at the orifice increases most rapidly and attains the highest value during the whole test. Unlike the linear vertical distribution of pressure in one-dimensional upward seepage, the excess pressure in the case of a local leakage shows significant concentrations close to the source of flow. This is interpreted as a localisation nature. From analytical derivation and numerical validation as presented in Section 5.5, it is found out that the excess pressure is proportional to ln(1/r).
- If a higher flow rate is applied, fluidisation is observed at the vicinity of the orifice, which is characterised by a sudden cavity formation and a sharp pressure drop at the orifice. It is observed that the bed humps in the middle due to the cavity

formation, which agrees with the experimental findings by Alsaydalani (2010). Besides, the sharp pressure drop is attributed to the sudden ‘unblocking’ of the surrounding soil particles.

- Special attention is paid to a narrow range of flow rate where the cavity stops growing in a short period after its formation. Both the V-t curves and p-t curves eventually level off, indicating a steady state is reached. Although such a regime may be more dangerous to infrastructures as it is difficult to identify from the surface above, no further investigations have been provided among literatures. Therefore, Chapter 6 attempts to explore its underlying mechanism using numerical results.
- With the model parameters presented in Section 5.2, the cavity is continuously developing when the applied flow rate is higher than 1.05 l/s. The orifice pressure smoothly declines after its sharp drop when fluidisation occurs. The rate of cavity development is found to be constant for each case. It is also found out that a greater flow rate leads to an earlier fluidisation and a quicker cavity development. For quantifying the cavity evolution, Chapter 7 presents a further analysis using the numerical results.

Numerical simulation also demonstrates a blow-out failure with an even higher controlled flow rate. Within the test period, the cavity grows up to the bed surface so as to open up a fluid channel. Fluctuations are observed in the p-t curves, indicating unsteady flow

behaviour. In addition, excess pressures at shallower locations are occasionally greater than those at deeper locations, suggesting backward flows and local vortices. With an extremely high flow rate, the excess pressures near the orifice may even increase during the cavity development due to such a rapid energy input. An unsymmetrical pattern of the channel shape is also noticed, which is attributed to the non-zero horizontal momentum of the injected fluid. This is also due to the fact that the bed is not really symmetric and the system is unstable, hence any small difference will be amplified.

In addition, a comparable study is carried out in order to validate the numerical results against the experimental data by Alsaydalani (2010). Since the particle size, the orifice width, and the flow rate are not directly comparable to the experimental model, a quantitative comparison is not straightforward. In spite of this, good qualitative agreement on the main findings for the onset of fluidisation is still obtained. These include:

- The excess pressure near the orifice grows up to a peak point with the increase in the flow rate. The onset of fluidisation can be identified from this peak point. Beyond the point, the pressure undergoes a sharp reduction as flow rate further increases. However, at the area further from the orifice, both numerical and experimental data suggest a less obvious change in excess pore pressures. This is regarded as a major effect of localisation nature.
- With the increase in flow rate, the onset of fluidisation can also be identified from

the most significant pressure gradient near the orifice. In agreement with experimental results, the critical hydraulic gradient is found to be greater than that of a normal seepage failure according to Terzaghi's failure theory.

- The cavity is viewed as a fluidised zone in the numerical results, where particles are mobilised and moving freely with the injecting fluid. This was also recognised by Alsaydalani (2010) as an 'internally fluidised zone'.
- At the onset of fluidisation, the particles within an uplifting zone are being raised while those outside the zone remain steady. Both experimental and numerical results show that the uplifting zone is of an inverted-tapered shape. And the numerical results show a reasonably similar wedge angle with that measured from the experiments.

As shown by experimental data (Alsaydalani, 2010), the fluidising mechanism in a locally injected fluid is a force balance between the upward drag force applied to the uplifting wedge and its bulk weight. However, the previous prediction of fluidising pressure was based on an assumption of a vertical flow distribution. This is not exactly true in a real soil subject to a local leakage. Although Alsaydalani (2010) argued that the leaking fluid should be spreading radially, there is no further evidence provided by his results. With the aid of numerical simulation, a radial flow distribution is obtained, as presented in this chapter. Therefore, the flow equation and the expression of fluidising pressure are modified according to the radial distribution. The numerically measured

fluidising pressures are found to match well with the predicted ones using the modified equation. Furthermore, from the analytical derivation, it is recognised that the fluidising pressure is approximately proportional to an equivalent height H' which is defined by Eqn.(5.15), provided that the seepage flow is primarily dominated by the first order of superficial velocity. This can also be seen from the numerical solutions.

CHAPTER 6: A STABLE CAVITY

6.1 Introduction

Due to the special importance in safety issues raised by the stable-cavity regime, as stated in Section 5.3.1, this chapter is intended to achieve deeper understanding of such a phenomenon so that the underlying mechanism is explored. The changes in the flow field due to the formation of a stable cavity are firstly studied in Section 6.2. And the underlying mechanism is explored in Section 6.3. The main findings in this chapter are summarised in Section 6.4.

6.2 Changes in the Flow Field

6.2.1 Velocity distribution

Figure 6.1 shows a typical cavity evolution of the stable-cavity regime. The onset of fluidisation is found to occur at 4.3s in the test. The cavity grows for a short period and then remains at a steady size. The interstitial velocities directly above the orifice at 4s and 10s are respectively plotted against 1/h in Figure 6.2. At 4s, the soil bed remains motionless with only seepage flow prevails. Due to the radial flow distribution as demonstrated in Chapter 5, the flow rate is constant at each half-circular shaped cross-sectional area. Therefore, it is obtained

$$Q = \pi r \omega_0 u_{in} \varepsilon = const. \tag{6.1}$$

where Q is the flow rate. u_{in} and ε are the interstitial velocity and bed porosity, respectively. Their product indicates the superficial velocity. Eqn.(6.1) can then be simplified as

$$u_{in} = \frac{C'}{\varepsilon} \cdot \frac{1}{r} \tag{6.2}$$

where

$$C' = \frac{Q}{\pi \omega_0} \tag{6.3}$$

If taken the interstitial velocity directly above the orifice, Eqn.(6.2) can be rewritten as

$$u_{in} = \frac{C'}{\varepsilon} \cdot \frac{1}{h} \tag{6.4}$$

Eqn.(6.4) explains why an approximately linear relationship is found between the interstitial velocity and 1/h at 4s, as shown in Figure 6.2. However, at 10s when the cavity remains at a stable size, it is found the linear relationship is valid for most areas except those are near the orifice. The inflection point is found when $h = 0.016m$, as seen in the red scattered markers in Figure 6.2. It is thereafter identified as the exact height of the stable cavity, which can be measured from the particle configuration plot (see Figure 6.3). Hence, it indicates that the radial seepage flow still prevails above the cavity, while this is not the case in the cavity. Moreover, the slope in the linear relationship is found to decrease due to the cavity formation, as seen in Figure 6.2. This is likely to be the result of increased porosity above the cavity, according to Eqn.(6.4). On the other hand, the flow in the cavity possesses much higher velocity, and the radial distribution is not sustained any

longer. Actually, the velocity distribution is difficult to be described. With the velocity vectors being plotted, it is seen that local vortices exist within the cavity (see Figure 6.4).

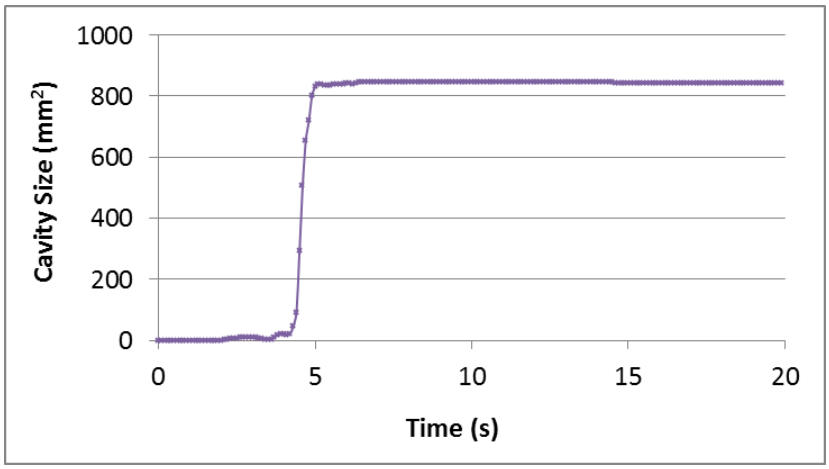

Figure 6.1 Cavity evolves to a stable size

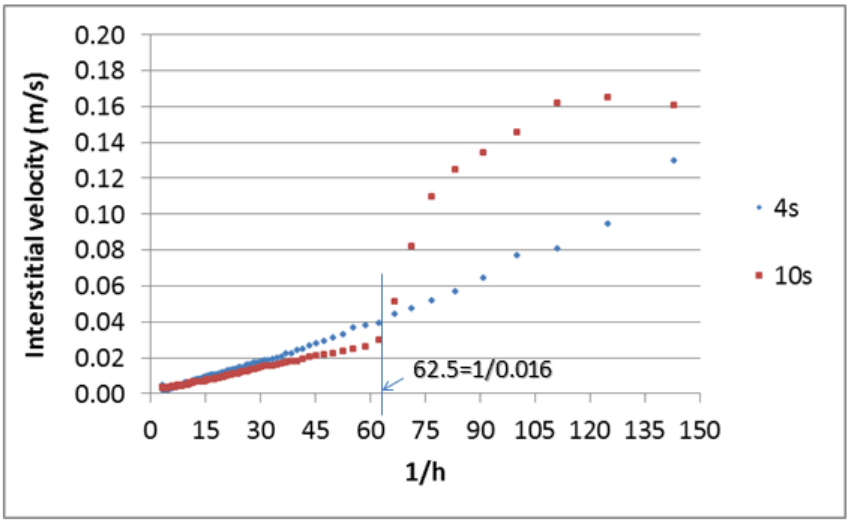

Figure 6.2 Interstitial velocity directly above the orifice vs. 1/h

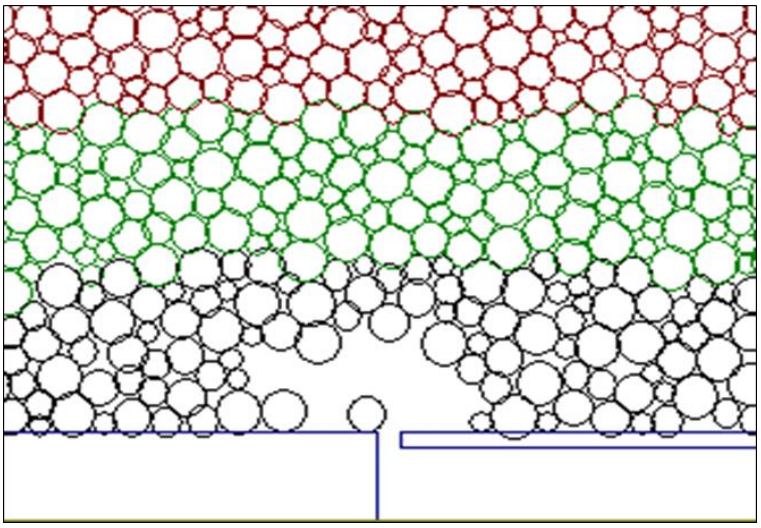

Figure 6.3 Particle configuration zoomed into the cavity area (each coloured single layer represents 0.02m in height)

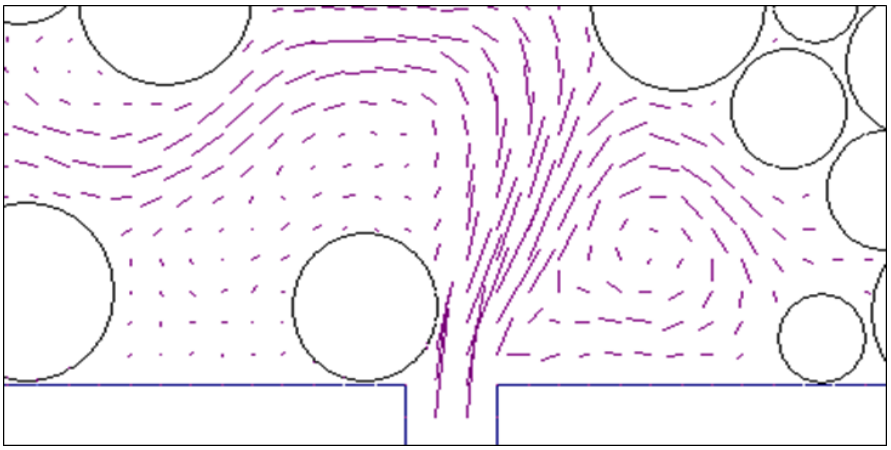

Figure 6.4 Velocity vector plot: vortices exist within the cavity

6.2.2 Pressure distribution

Figure 6.5 demonstrates how the excess pressure directly above the orifice distributes vertically, and how the distribution changes with time. It can be seen that the pressure at

any height is initially accumulating, until it reaches the maximum which triggers fluidisation at 4.3s. Within a short period afterwards, the excess pressure undergoes a significant drop near the orifice, but a remarkable increase at shallower locations. This is mainly resulted from the cavity formation. As time goes by, pressures at deeper locations are decreasing while at shallower ones increasing. This is because pressures are propagating from bottom to top. Till around 7s, the pressure distribution starts to stabilise, indicating a steady state is achieved.

With the aid of curve fitting, as shown in Figure 6.6, it is identified that the logarithmic flow equation derived as Eqn.(5.12) is satisfied at the onset of fluidisation. Moreover, after the steady state is achieved, the pressure distribution above the cavity still exhibits the logarithmic nature. This further implies that the seepage flow prevails above the cavity. However, within the cavity, the pressure distribution cannot be easily described.

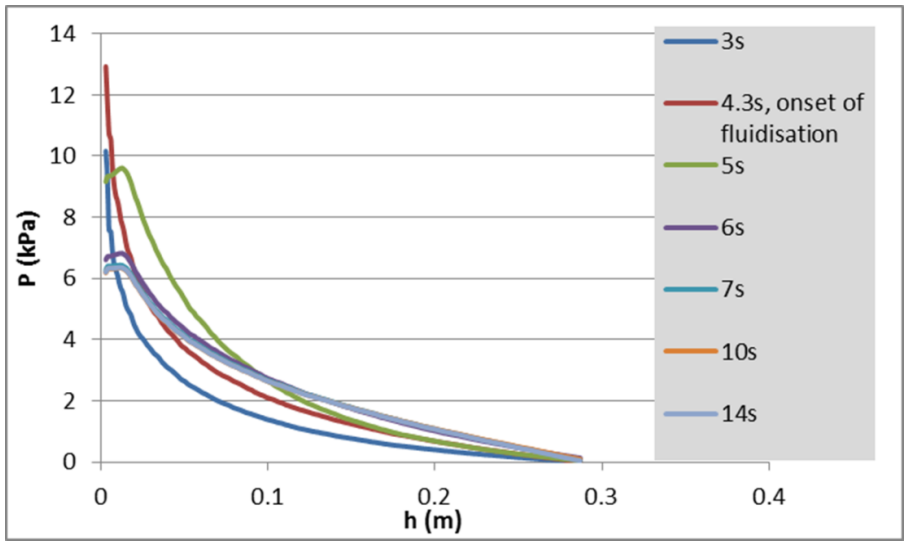

Figure 6.5 Vertical distribution of the excess pressure directly above the orifice

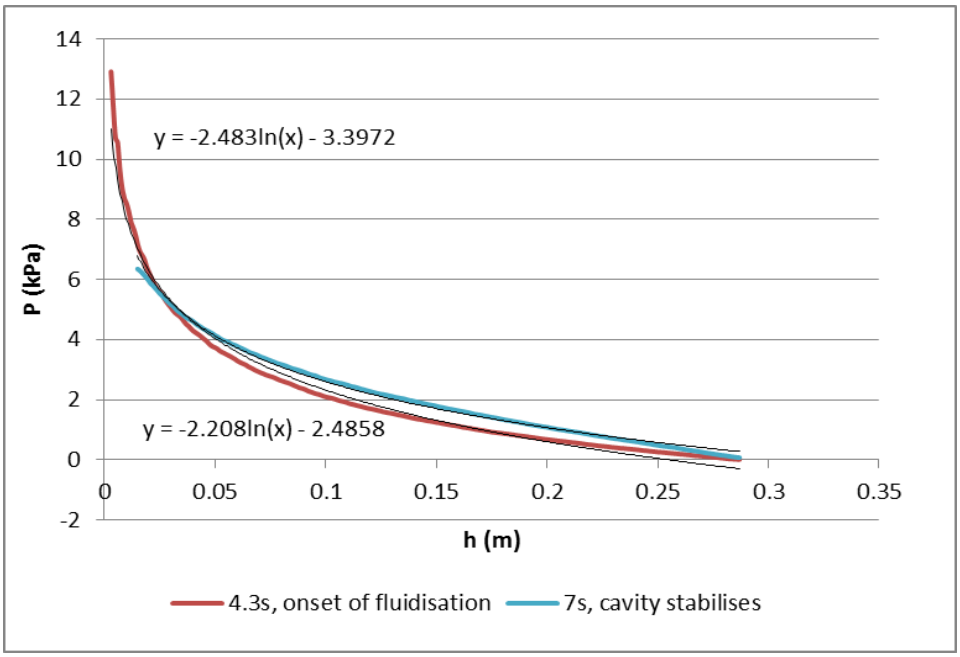

Figure 6.6 Logarithmic nature of the pressure distribution

6.3 Mechanism Underlying a Stable Cavity

In this section, the mechanism underlying the formation of a stable cavity is explored using the numerical outcome.

By drawing a wedge with the inclination angle of χ in the sample bed (see Figure 6.7), the fluid-induced forces calculated by IMB (see Eqn.(3.62)) are summed up over all the particles within the wedge, giving the total upward drag force denoted as F. Besides, the wedge weight W is also calculated by summing up the weight of each particle within the wedge.

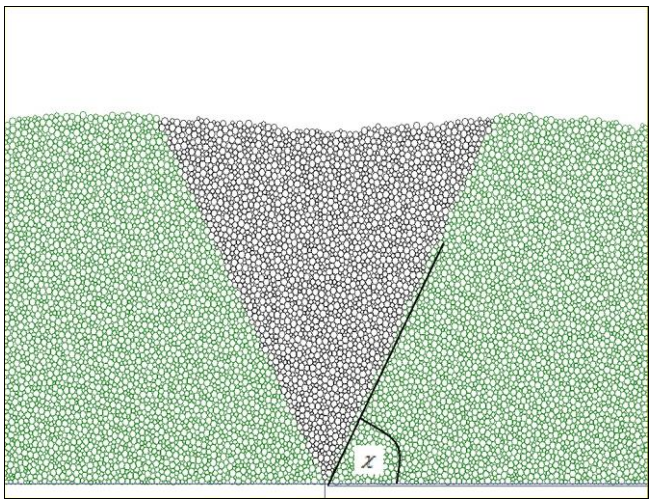

(a) Before fluidisation occurs

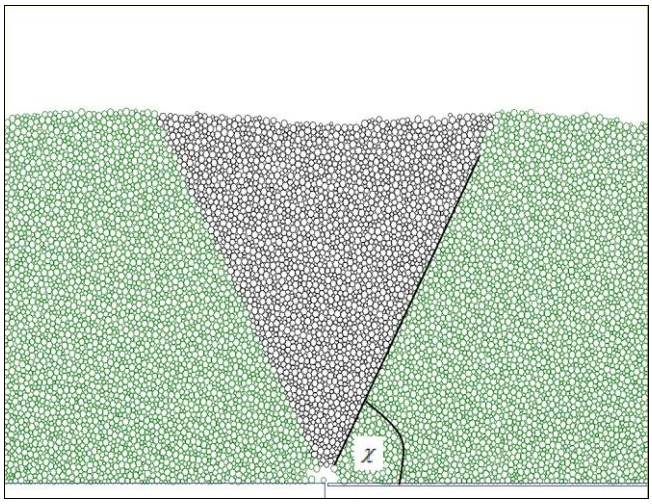

(b) After the cavity stabilises

Figure 6.7 A wedge drawn for force calculations

Figure 6.8 presents the evolution of F and W with different values of χ.

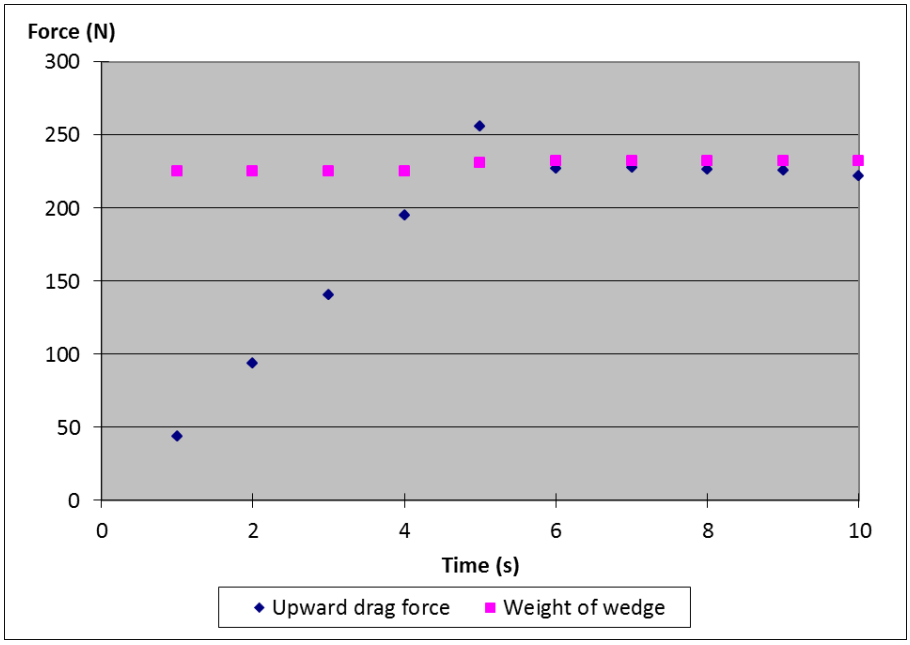

(a) $\chi = 80^{\circ}$

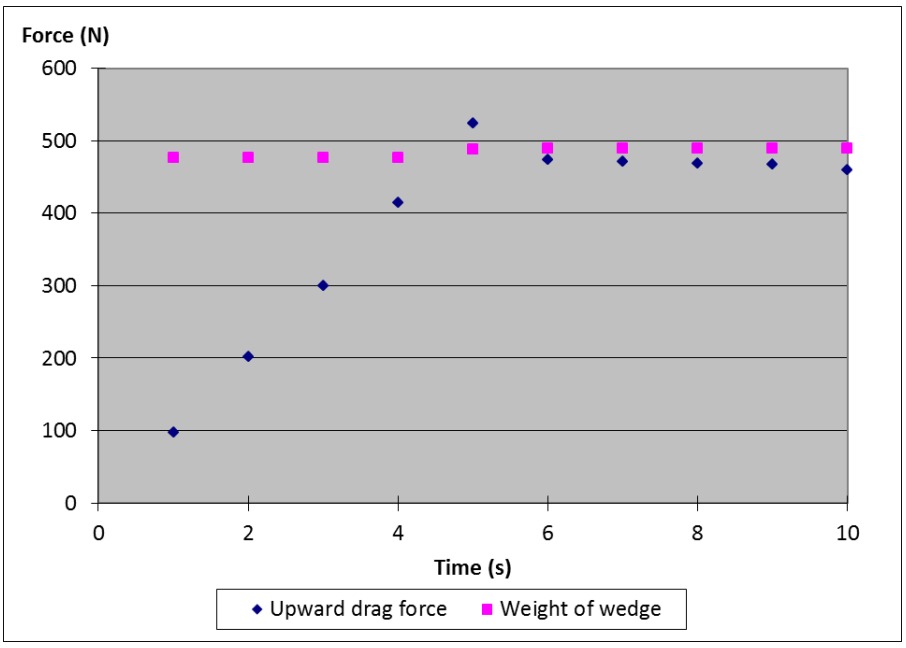

(b) $\chi = 70^{\circ}$

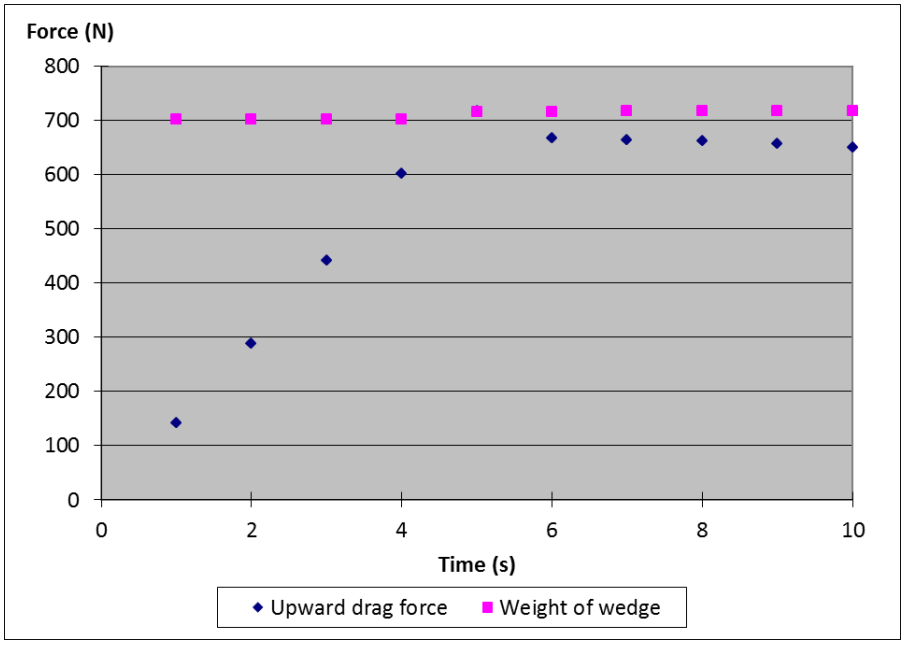

(c) $\chi = 62^{\circ}$

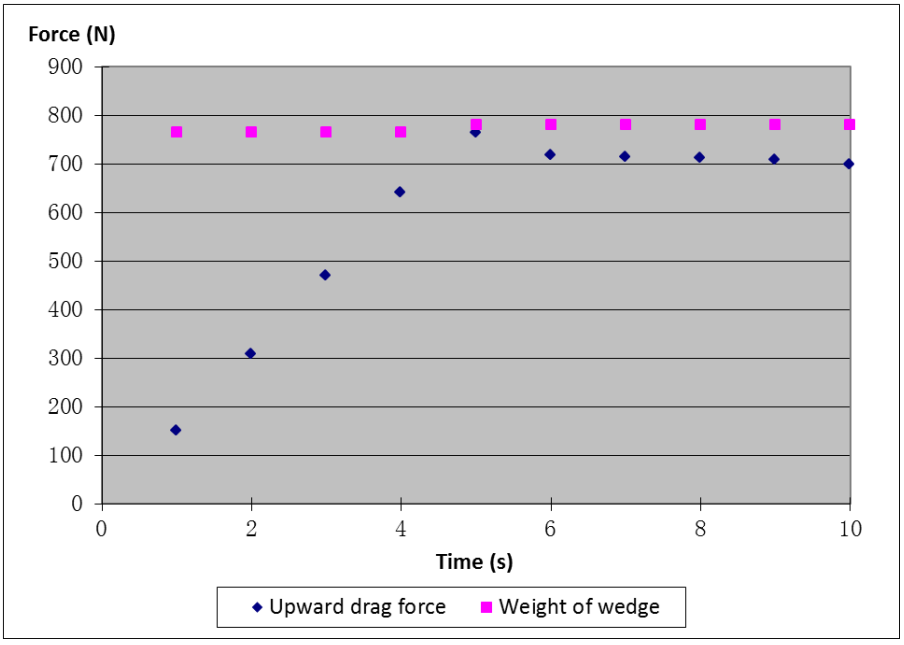

(d) $\chi = 60^{\circ}$

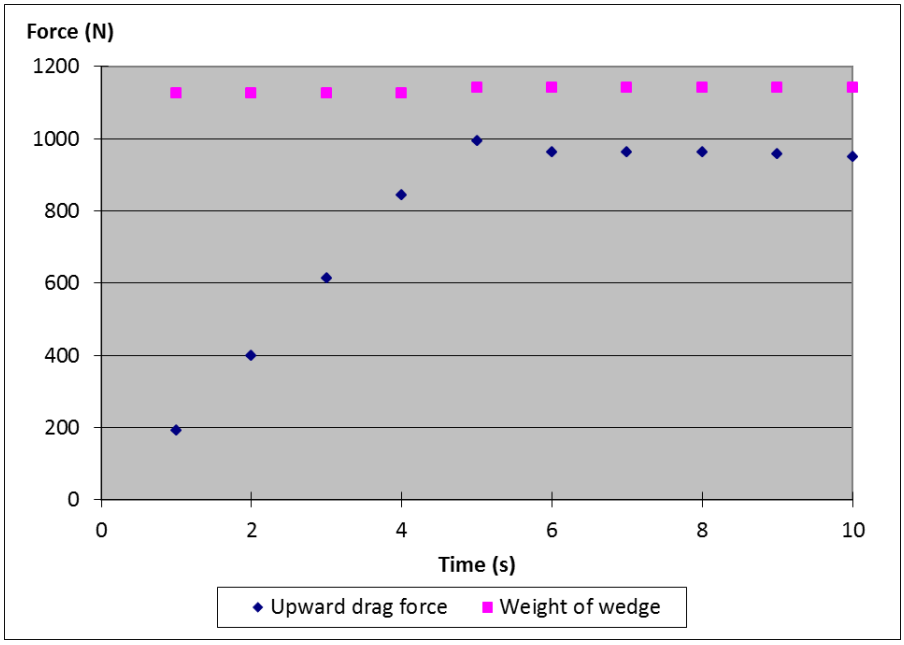

(e) $\chi = 50^{\circ}$

Figure 6.8 Evolutions of the upward drag force and wedge weight

From Figure 6.8, it can be seen that W undergoes a slight increase between 4s and 5s. By counting the number of particles, it is found out there are more particles in the wedge at 5s compared with 4s. This is mainly due to the cavity formation, where stresses on both sides are suddenly released during the uplifting mechanism, allowing particles beside the wedge to move into it. On the other hand, F initially goes up to the peak and then decreases till a steady level. It is believed that the decrease is induced by the pressure drop at the vicinity of the orifice during cavity evolution.

As presented in Section 5.4.3, the actual uplifting zone has an inclination angle of 62°. From Figure 6.8(c), it is recognised that F and W are becoming equal to each other

during 4s and 5s when fluidisation is initialised. This is identified as the force balance at the onset of fluidisation. However, as F then undergoes a decrease, it becomes less than W. It is therefore argued that a new mechanism is involved in the force balance in order to prevent the cavity from collapse under the excess weight. The argument is evidenced by plotting the force chains using DEM (see Figure 6.9). The thickest force chain represents the maximum contact force at a given time. From Figure 6.9, it can be identified that the initial force transmission is primarily along the vertical direction (see Figure 6.9(a)), but becoming inclined in the middle as the seepage flow permeates radially from the orifice (see Figure 6.9(b)). After the cavity forms (see Figures 6.9(c) and (d)), sparser vertical chains but denser horizontal ones are identified above the cavity. This indicates the fact that the soil on the side tries to slide down under gravity, but it is prevented by the fluid pressure in the cavity, so that the horizontal supports are formed on each side. It is believed that such supports generate upward friction and plays an important role in bearing the excess weight.

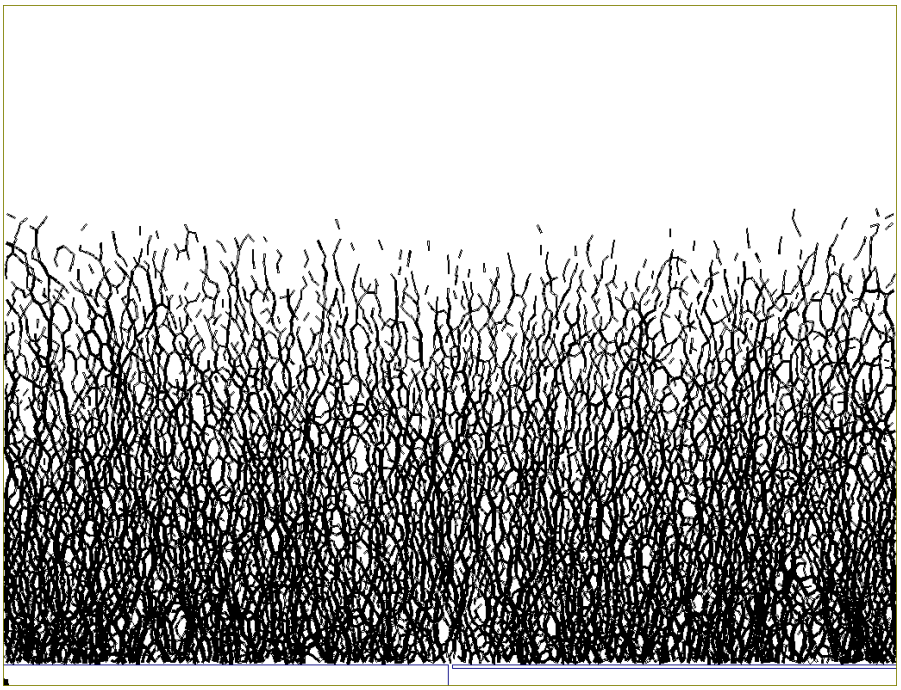

(a) t = 1s

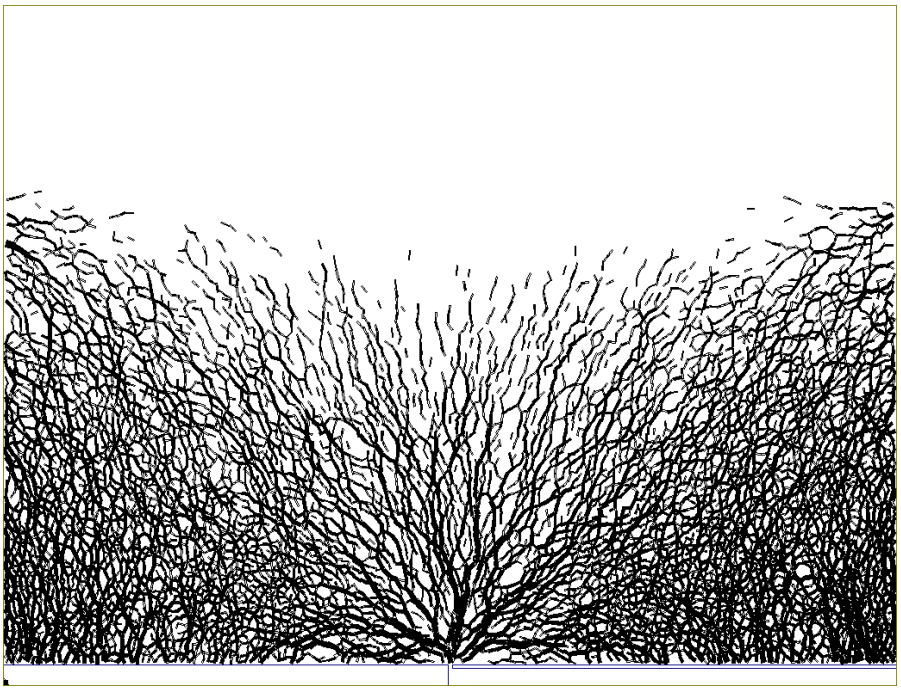

(b) t = 4s

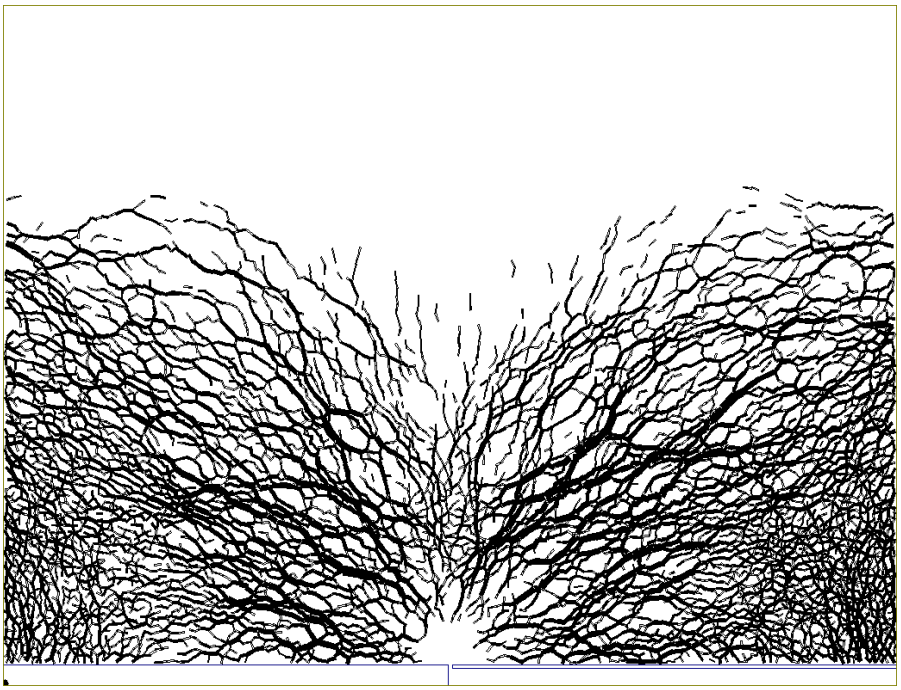

(c) t = 5s

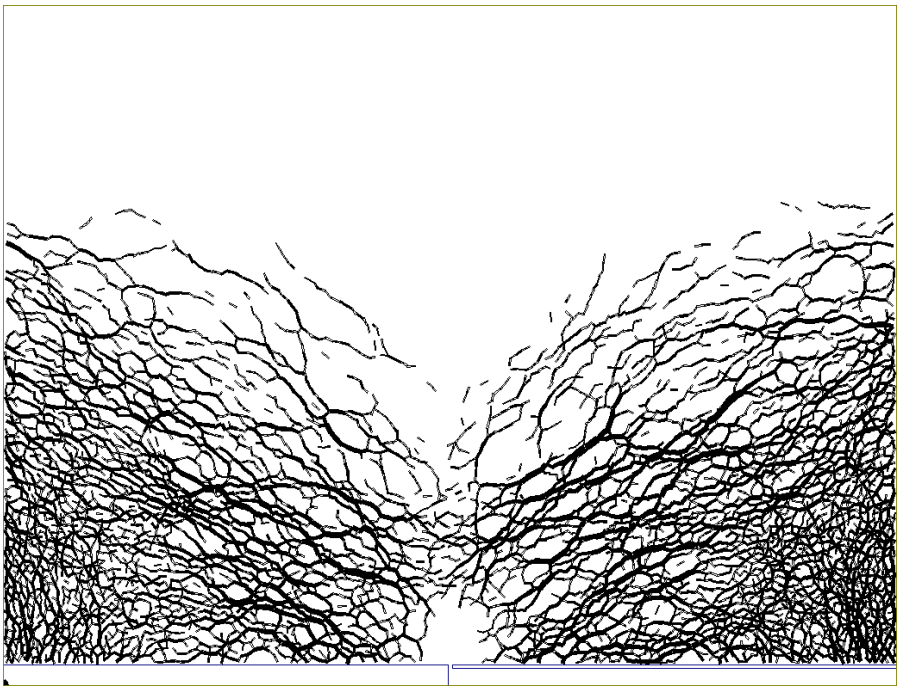

(d) t = 10s

Figure 6.9 Evolution of force chains during the formation of a stable cavity

Seen from Figure 6.8, for a wedge with χ greater than 62°, the excess weight after cavity formation is less than that in the case of $\chi = 62^{\circ}$. Therefore, it is recognised that a new force balance can be more easily achieved by the upward friction. However, for a wedge with χ less than 62°, F is smaller than W during the whole test period, hence fluidisation cannot be activated. This further explains why a wedge angle of 62° is obtained as a critical one for the sample model used in the numerical test.

6.4 Summary

This chapter studies on the stable-cavity regime, in which the cavity reaches to a steady size shortly after its formation. Numerical results suggest that the radial seepage flow prevails above the cavity, while this is not the case in the cavity. It also indicates that the porosity above the cavity is increased, and hence the slope in the linear relationship between interstitial velocity and 1/h is found to be lower than that before fluidisation occurs. On the other hand, the flow in the cavity possesses much higher velocity, and its distribution is difficult to be described. With the velocity vectors being plotted, it is seen that local vortices exist within the cavity.

Before fluidisation occurs, the excess pressure directly above the orifice at any height is accumulating, until it reaches to the maximum which activates fluidisation. The logarithmic flow equation derived as Eqn.(5.12) is found to be satisfied at the onset of

fluidisation. Within a short period afterwards, the excess pressure undergoes a significant drop near the orifice, but a remarkable increase at shallower locations. This is due to the cavity formation. As time goes by, pressures at deeper locations are decreasing while at shallower ones increasing. This is because pressures are propagating from bottom to top. From around 7s, the pressure distribution starts to stabilise, indicating a steady state is achieved. The pressure distribution above the cavity is found to exhibit the logarithmic nature, which again implies the seepage flow prevails. However, within the cavity, the pressure distribution cannot be easily described.

From the numerical outcome, it can be seen that the wedge weight W undergoes a slight increase. This is mainly due to the cavity formation, where stresses on both sides are suddenly released during the uplifting mechanism, allowing particles beside the wedge to move into it. On the other hand, F is initially goes up to the peak and then decreases till a steady level. It is believed that the decrease is induced by the pressure drop at the vicinity of the orifice during cavity evolution.

For a wedge with the inclination angle $\chi = 62^\circ$ in the numerical test, F and W are becoming equal to each other at the onset of fluidisation, indicating a force balance. Thereafter, F becomes less than W due to its decrease and a slight increase in W. By observing the force chain plot, it is then argued that horizontal supports are provided by fluid pressure in the cavity so as to generate upward friction on the side. This upward

friction is involved in a new force balance, and the cavity is prevented from collapse under the excess weight.

In addition, for a wedge with χ greater than 62°, the excess weight after cavity formation is less than that in the case of $\chi = 62^{\circ}$. Therefore, it is recognised that a new force balance can be more easily achieved by the arching effect. However, for a wedge with χ less than 62°, F is smaller than W during the whole test period, hence fluidisation cannot be activated. This further explains why a wedge angle of 62° is obtained as a critical one for the sample model used in the numerical test.

Furthermore, it is argued that, for a sufficiently high flow rate, it would be no chance to form a stable cavity if F sustains at a higher level than W after the cavity formation. In such a case, the cavity tends to enlarge over time. As for how the cavity evolves with time, Chapter 7 presents an analysis using numerical data from parametric studies.

CHAPTER 7: CAVITY EVOLUTION

7.1 Introduction

In this chapter, analyses are carried out in order to study the cavity evolution. With the results from parametric studies, general expressions of the cavity evolution under controlled flow rate and controlled pressure in the pipe are deduced in Sections 7.2 and 7.3, respectively. In addition, as cohesive soils are also common in the geotechnical engineering field, it would be worth considering the mechanical effect of cohesion in the pipe leakage problem. As stated in Section 2.3.2, the auto-adhesive contact model (Thornton, 1991; Thornton and Yin, 1991; and Thornton and Ning, 1998) is adopted for this reason, and how the inter-particle adhesion influences the cavity evolution is explored in Section 7.4. However, difficulties are encountered in determination of soil cohesion from the DEM parameter at the particulate scale. In an effort to build up the link between the cohesion effect and the inter-particle adhesion, in Section 7.5, numerical tests are carried out on a slope stability problem. Finally, a summary of the main findings in this chapter is given in Section 7.6.

7.2 Cavity Evolution under Controlled Flow Rate

In this section, cavity evolution is explored using the numerical results presented in Section 5.3. The flow rate in each test is held constant during the test period. If a blow-out failure occurs, fluidisation can be identified from above the bed surface, for which

studying the cavity evolution is of little importance any more. Hence, the blow-out regime is not considered in this section, and the flow rate varies from 0.25 l/s to 2.0 l/s among tests.

7.2.1 Cavity size vs. flow rate (V-Q curves)

From the numerical results, the cavity size is plotted against the controlled flow rate in Figure 7.1, which is denoted as the V-Q curves hereinafter. The bed regimes can be classified using these curves. It can be seen that in the fixed-bed regime, the V-Q curve remains at zero level because fluidisation is not initiated with a sufficiently low flow rate, i.e. 0.25 l/s to 0.8 l/s. While for a flow rate in the range from 0.85 l/s to 1.05 l/s, the cavity size evolves to a steady value shortly after fluidisation (i.e., the stable-cavity regime). For instance, with a flow rate of 0.9 l/s, no cavity has been identified during the initial seven seconds. Afterwards, a cavity forms and its size jumps to approximately 400 mm^2 within the next one second, before it stops growing and maintains at the same size. In addition, it can be recognised that a higher flow rate leads to an earlier cavity formation.

If the flow rate exceeds 1.05 l/s, it can be easily identified from the V-Q curves a continuous growth in the cavity size, indicating the growing-cavity regime. Again, it is found out that a higher flow rate induces a larger cavity at a given time. It is also worth noting that, if the flow rate is above 1.2 l/s in the current numerical model, the cavity size

is almost linear to the constant flow rate at any given time. Its size as a function of flow rate and time is then quantified by analysing the numerical data, which is presented in the following sub-section.

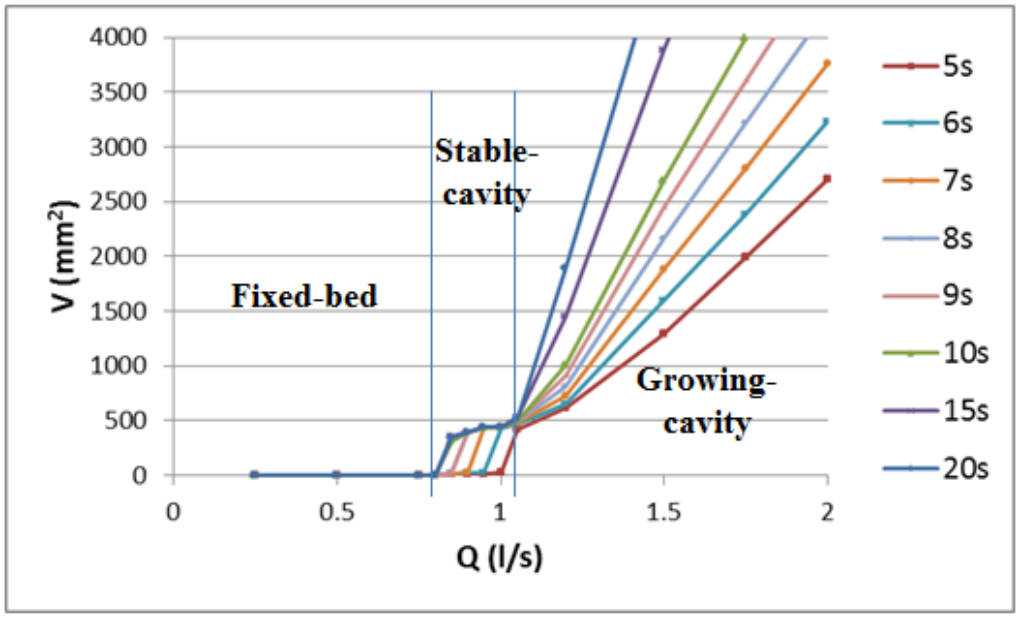

Figure 7.1 V-Q curves

7.2.2 Cavity size as a function of flow rate and time

For a constant flow rate at which a continuously growing cavity is induced, the cavity evolution is found to be linearly related to flow rate at a given time, as mentioned in Section 7.2.1. It is therefore worth studying for a general expression of cavity size as a function of flow rate and time. In Figure 7.2, the linear V-Q curves are firstly plotted and fitted by equations. It is then recognised that all the fitted curves tend to intercept at a single point, i.e. (1.0 l/s, 0). Hence, it can be written that,

$$V(Q)(mm^2) = k(Q - 1.0l/s) \tag{7.1}$$

where k is independent of flow rate. By the curve fitting as shown in Figure 7.2, the value of k at each given time can be obtained. Its value is then plotted against time, as shown in Figure 7.3. It is interesting to note that k is linear to time. By the curve fitting in Figure 7.3, it is given that,

$$k = C_1 t + C_2 \tag{7.2}$$

where C_1 and C_2 are independent of either time or the controlled flow rate.

Substituting Eqn.(7.2) into Eqn.(7.1), one can obtain

$$V(Q,t)(mm^2) = (C_1 t + C_2)(Q - 1.0l/s) \tag{7.3}$$

For a more general expression, Eqn.(7.3) can be rewritten as

$$V(Q,t) = (C_1 t + C_2)(Q - Q_0) \tag{7.4}$$

where Q_0 is interpreted as the theoretical critical controlled flow rate, beyond which a continuously growing cavity is thought to be generated. In the current numerical tests, Q_0 = 1.0 l/s. It may be noted that it is a bit different from 1.05 l/s which is identified from the numerical results (see Figure 7.1). Such a difference is mainly attributed to the following reason. Since Q_0 is derived by extrapolation of the V-Q curves, its value reflects the resistance to the continuous uplifting of the wedge, such as kinetic friction. However, a bit higher flow rate shall be required in order to overcome the initial resistance, including static friction. Therefore, Q_0 is regarded as a *theoretical* critical

value which is a bit smaller than the actual one required for the growing-cavity regime.

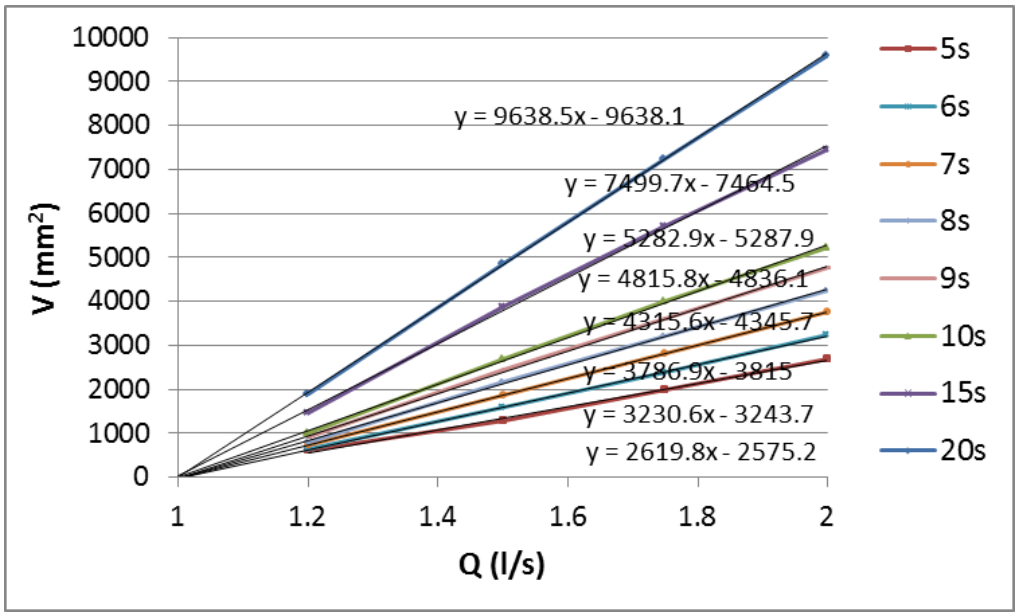

Figure 7.2 Linear V-Q curves with curve fitting

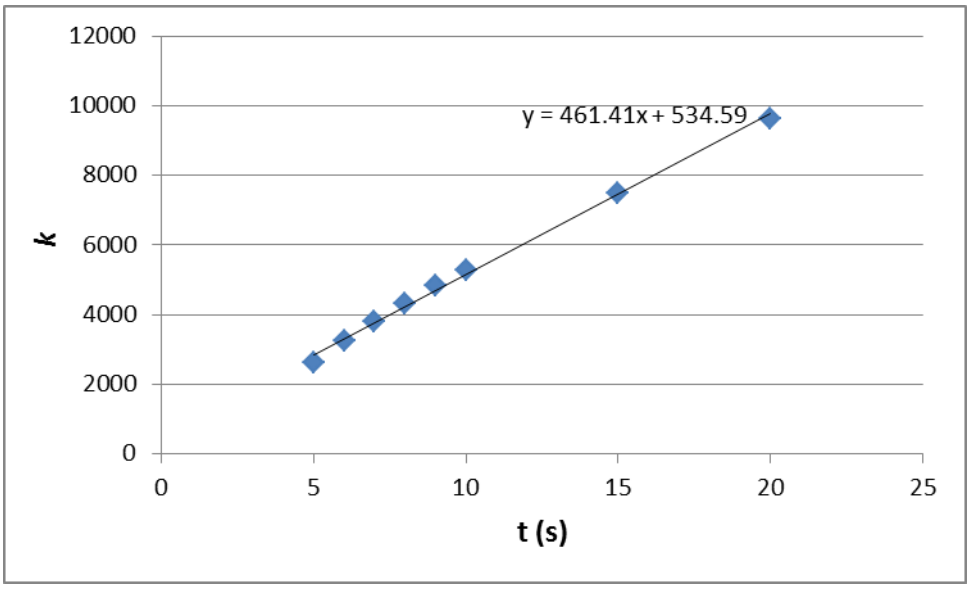

Figure 7.3 *k* vs. time

7.3 Cavity Evolution under Controlled Pressure in the Pipe

7.3.1 Numerical tests under controlled pressure in the pipe

In this section, a parametric study is carried out with pressure in the pipe being maintained constant during each test. In order to maintain a constant pressure in the pipe, a slight modification is made to the model illustrated in Section 5.2.2. In the modified model, the pipe spans the whole length of the soil bed, i.e. 600mm (see Figure 7.4). The orifice opening is located at the top surface of the pipe, representing a leak. An identical pressure is applied at both the pipe inlet (on the left) and outlet (on the right) during each test. Table 7.1 shows the test arrangement in this section. As stated in Section 5.5.3, the particles are artificially kept from moving during the initial four seconds in order to obtain a well-developed fluid flow in bed. The p-t curve at the orifice is presented in Figure 7.5. The initial oscillations are mainly due to wave propagation in the LBM computations (Li, 2012). It is also found out that an almost steady level is achieved at the end of 4s, indicating a steady state is approximately obtained.

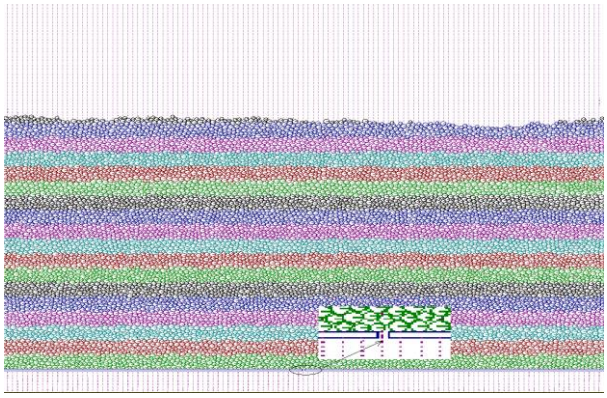

Figure 7.4 Setup of the modified numerical model (insert: details around the orifice)

Table 7.1 Test arrangement with controlled pressure in the pipe

Test No.	Controlled pressure in the pipe (kPa)
P1	4.67
P2	4.83
P3	4.90
P4	5.83
P5	6.67
P6	8.33
P7	10.00

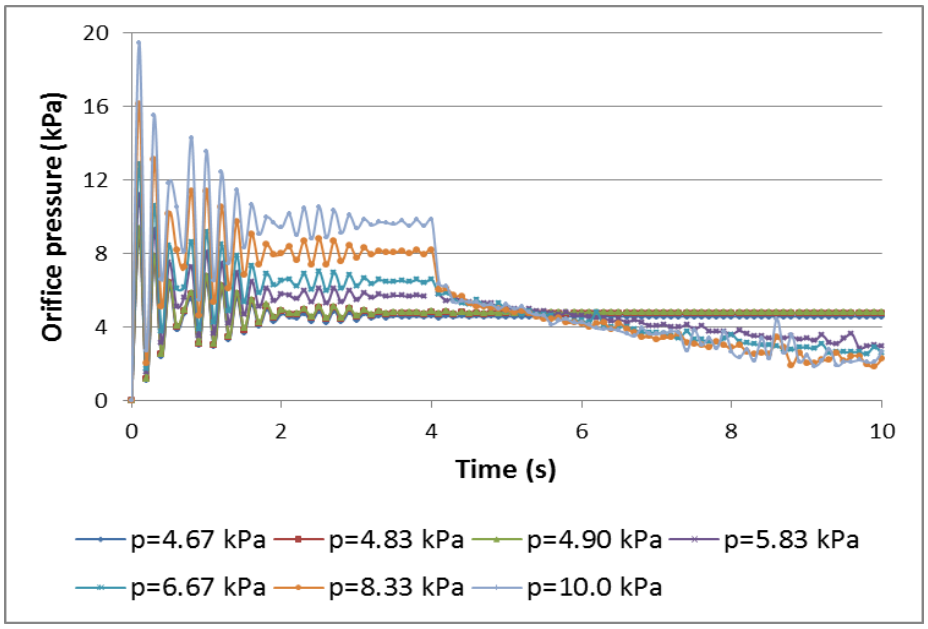

Figure 7.5 p-t curves at the orifice with different controlled pressures in the pipe

Once the particle movements are allowed at 4s, different soil behaviours are identified from Figure 7.5. With a controlled pressure no more than 4.9 kPa, the orifice pressure sustains at the original level. While with a higher controlled pressure, it starts to decrease. This indicates that fluidisation is activated by a sufficiently high pressure and a cavity starts to grow with time.

With a controlled pressure no lower than 6.67 kPa, blow-out failure is identified from the results. The cavity evolution (the V-t curve) before the blow-out failure is shown in Figure 7.6, in which the starting time is taken as the time when fluidisation occurs. A general expression of the cavity size as a function of controlled pressure and time is thereby deduced using the numerical results, as presented in the following sub-section.

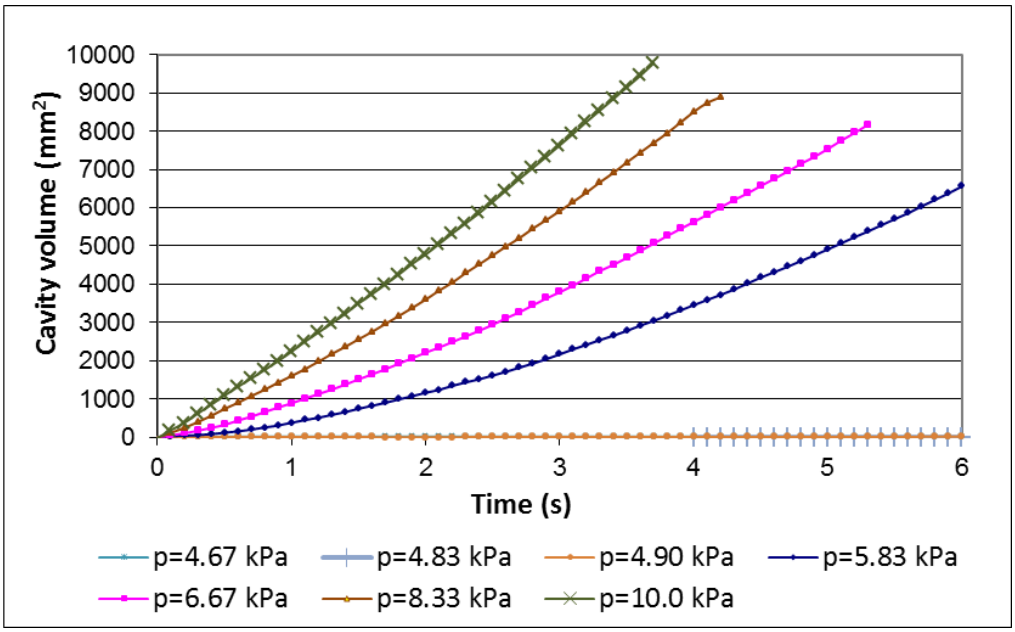

Figure 7.6 V-t curves with different controlled pressures in the pipe

7.3.2 Cavity size as a function of pressure in the pipe and time

Using the numerical data shown in Figure 7.6, the cavity size is plotted against the controlled pressure in the pipe in Figure 7.7, denoted as the V-p curves. By the curve fitting and extrapolation, it is recognised that the cavity size approximately increases linearly with pressure in the pipe at a given time. All the fitted straight lines in Figure 7.7 tend to intercept at a single point, i.e. (4.7 kPa, 0). Hence, it can be written that,

$$V(p)(mm^2) = k'(p - 4.7kPa) \tag{7.5}$$

where k' is independent of the controlled pressure in the pipe. The value of k' is then plotted against time in Figure 7.8. By the curve fitting, it can be seen that k' is a quadratic function of time. Therefore, it is given that,

$$k' = k_1 t^2 + k_2 t \tag{7.6}$$

where k_1 and k_2 are independent of either time or the controlled pressure in the pipe.

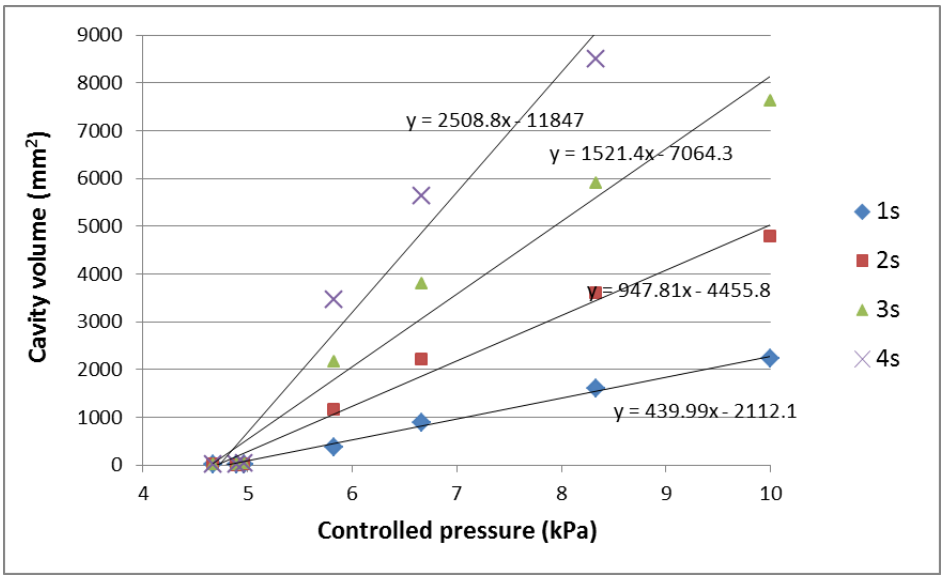

Figure 7.7 V-p curves

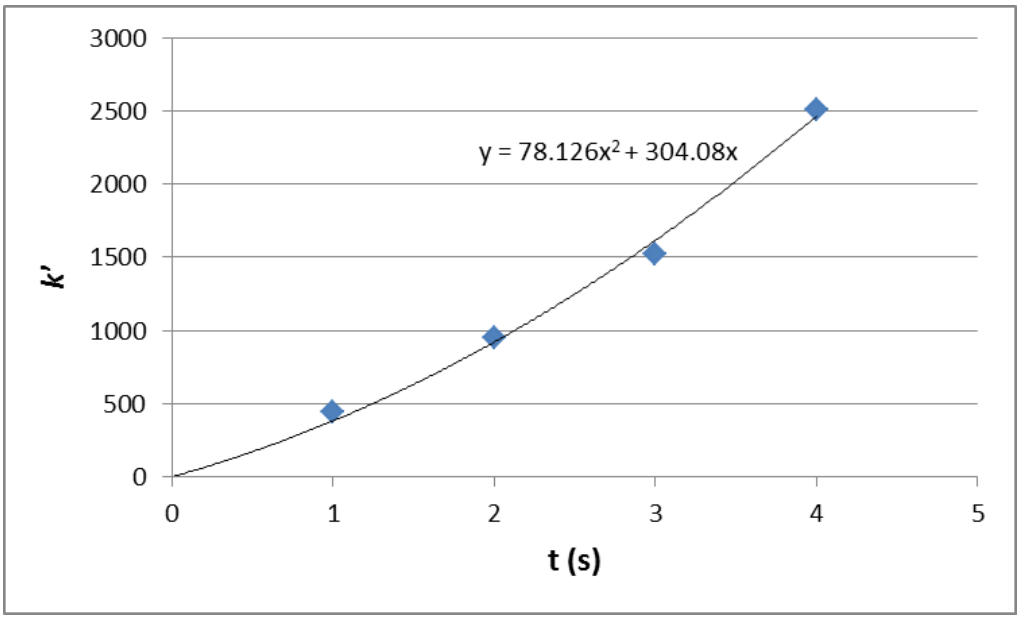

Figure 7.8 k' vs. time

Substituting Eqn.(7.6) into Eqn.(7.5), one can obtain

$$V(p,t)(mm^2) = (k_1 t^2 + k_2 t)(p - 4.7kPa) \tag{7.7}$$

For a more general expression, Eqn.(7.7) can be rewritten as

$$V(p,t) = (k_1 t^2 + k_2 t)(p - p_0) \tag{7.8}$$

where p_0 is interpreted as the theoretical controlled pressure to stimulate a growing cavity, which is 4.7 kPa in the current numerical tests. It is noted that this theoretical value is a bit lower than the actual fluidising pressure which is higher than 4.9 kPa identified from the numerical results. Similar to the reason explained in Section 7.2.2, such a difference is mainly attributed to the linear backward extrapolation scheme. In spite of the difference, p_0 is still taken as the *theoretical* fluidising pressure for further analysis

followed.

7.4 Cavity Evolution with Adhesive Particles

7.4.1 Numerical tests with inter-particle adhesion

As Stated in Section 7.1, since cohesive soils are commonly encountered in the geotechnical engineering field, it is worth studying the mechanical effect of soil cohesion in the cavity evolution. Hence, in this section, the adhesive particles are adopted. A parametric study is carried out with various inter-particle adhesion forces. Table 7.2 lists the controlled parameters used in this group of simulation, where K and Γ are defined in Eqns.(3.29) and (3.30). A constant pressure of 5.83 kPa is applied to both the pipe inlet and outlet in all tests. All other model parameters and the test procedure are the same as the previous ones in Section 7.3.

Figure 7.9 demonstrates the p-t curves at the orifice with different K values. It indicates that during the initial 4s when the sample bed is kept fixed artificially, the variations in orifice pressure show an identical pattern for all cases as the particle behaviour is not involved in calculations. Once the particle movements are permitted, the orifice pressure starts to decrease. However, a higher inter-particle adhesion force leads to a slower decrease. This can be attributed to a reduced cavity growth, which is further discussed in Section 7.4.2.

Table 7.2 The controlled parameters used to study the effect of inter-particle adhesion

Test No.	Ratio of inter-particle adhesion force to average particle weight, K	Particle surface energy, Γ (J/m^2)
A1/P4	0	0
A2	1	0.082
A3	3	0.246
A4	5	0.411
A5	7	0.575

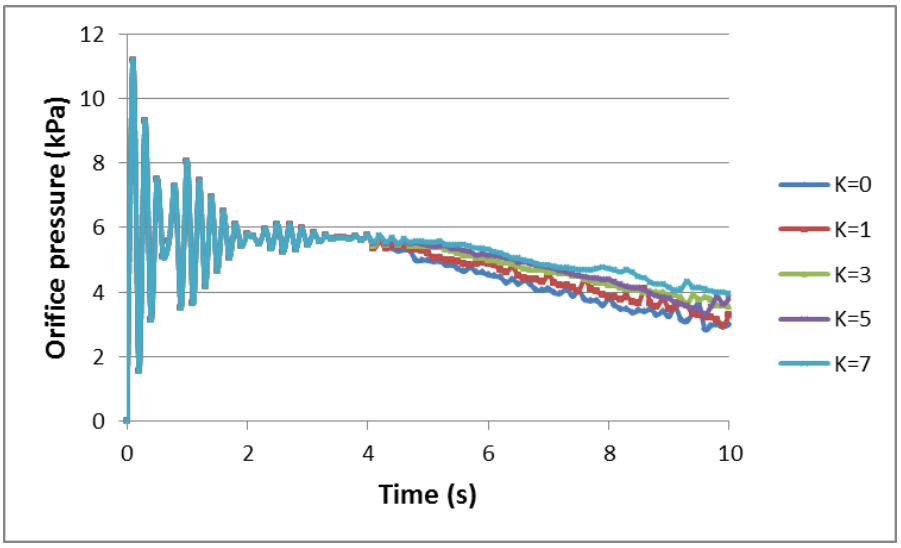

Figure 7.9 p-t curves at the orifice with different K values, and inlet/outlet pressure = 5.83 kPa

From the snapshots of particle configuration taken at the end of tests (see Figure 7.10), it can be identified that the cavity shape is also influenced by the presence of inter-particle adhesion. Unlike a more smooth and rounded cavity in the case with non-adhesive particles (i.e. $K = 0$), the cavity tends to have a branch-like or needle-like shape with inter-particle adhesion force due to hydraulic fracturing. It is interesting to note that similar shapes of cavity are also obtained by Royal et al. (2008) when they conducted laboratory tests on clayey soils. In their tests, epoxy was used to form a cast of the created cavity, and the typical cavity shapes obtained from their work are shown in Figure 7.11. It can be recognised that the use of adhesive particles is a promising approach to represent the mechanical effect of cohesive soils, in which the inter-particle bond cannot be neglected compared to particle weight.

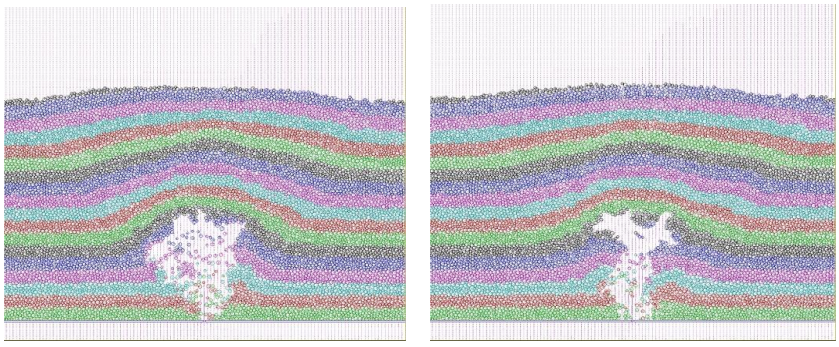

(a) $K = 0$ (b) $K = 1$

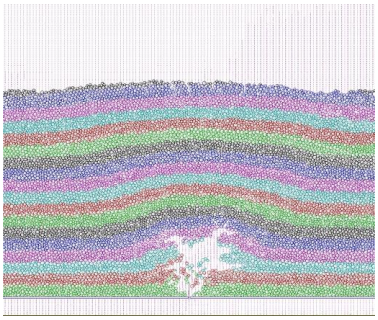

(c) $K = 3$

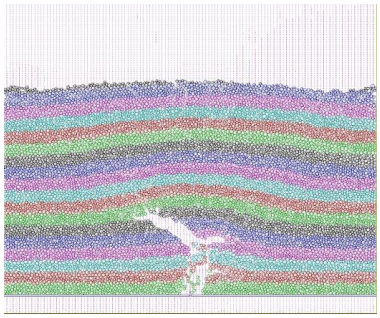

(d) $K = 5$

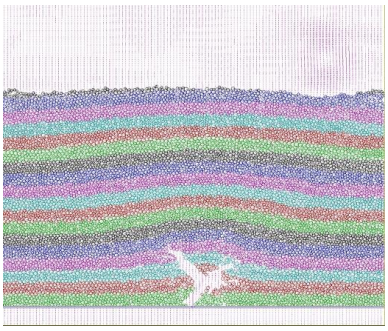

(e) $K = 7$

Figure 7.10 Snapshots of particle configuration with different K values, t = 10s

Scale 1:0.65

Scale 1:1.85

Scale 1:0.66

Figure 7.11 Typical branch-like and needle-like cavity shapes obtained from laboratory work by Royal et al. (2008)

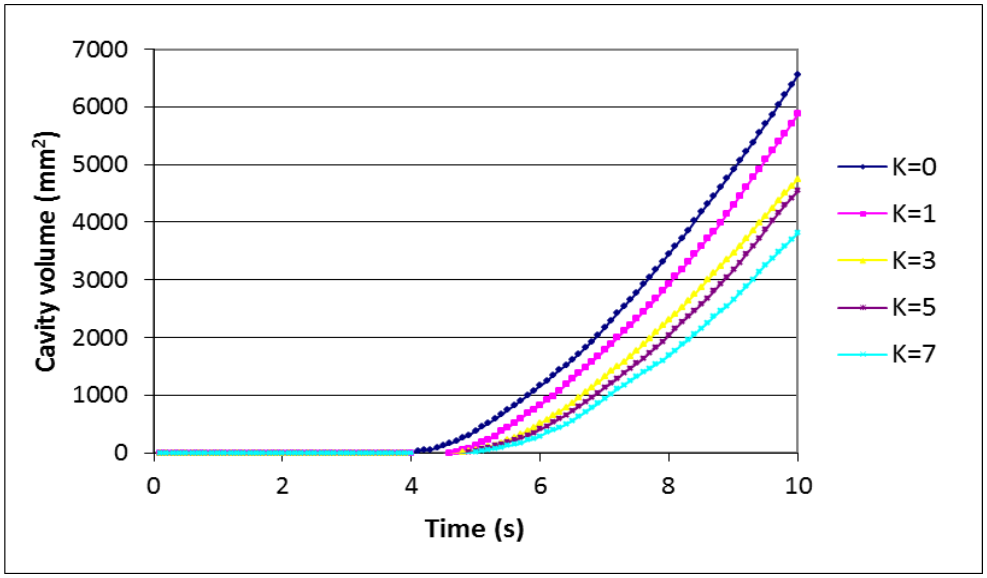

Figure 7.12 V-t curves with different K values, and inlet/outlet pressure = 5.83 kPa

Figure 7.12 illustrates the cavity evolution (i.e. V-t curves) with different K values. It is clear that a stronger inter-particle adhesion leads to a slower cavity development. And the following sub-section performs analysis in order to quantify such an effect of K.

7.4.2 Effect of adhesion force on cavity evolution

It is argued that the presence of inter-particle adhesion would increase the shear strength of a soil sample (see Section 7.5). Hence it leads to a higher fluidising pressure, and Eqn.(7.8) is required to be modified. In this sub-section, the general expression of cavity evolution with adhesive particles is analytically deduced as follows.

As demonstrated in Section 5.5.4, with the current model parameters, the superficial velocity is sufficiently small so that the seepage flow is primarily dominated by the first order of the superficial velocity. Therefore, by neglecting the second order term, it can be obtained from Eqn.(5.7) that,

$$F = 2\alpha_w \omega_0 A C_r (H - r_0) \tag{7.9}$$

Besides, according to Eqn.(5.12), the fluidising pressure can be simplified as

$$\Delta p_f = A C_r \ln \frac{H}{r_0} \tag{7.10}$$

Combining Eqns.(7.9) and (7.10), the fluidising pressure is presented as a function of the upward drag force:

$$\Delta p_f = \frac{\ln(H / r_0)}{2\alpha_w \omega_0 (H - r_0)} F_0 \tag{7.11}$$

where F_0 is the upward drag force applied to the wedge at the onset of fluidisation.

For the wedge consisting of adhesive particles, fluidisation can only be activated if the upward drag force is overcoming both the weight as well as the vertical component of the shear resistance. Therefore, the force balance at the onset of fluidisation is approximately written as below,

$$F_0 = W + \tau \cdot A_s \cos \alpha_w \tag{7.12}$$

where τ is the shear stress applied to the wedge, and A_s is the total area of the shear

planes. Since the effective stress is considered to be totally lost once fluidisation occurs, the shear stress can be considered to be composed of the undrained shear strength only, which is primarily contributed from soil cohesion. Hence, Eqn.(7.12) is rewritten as

$$F_0 = W + c_u \cdot A_s \cos\alpha_w \tag{7.13}$$

where c_u is the undrained shear strength of the soil sample.

From the results presented in Section 7.5, the relationship between c_u and K is expressed as

$$c_u = C_K \rho_p d_p K \tag{7.14}$$

in which C_K is as defined in Section 7.5.

Substituting Eqn.(7.14) into Eqn.(7.13), it is obtained that

$$F_0 = W + C_K \rho_p d_p A_s \cos\alpha_w \cdot K \tag{7.15}$$

Therefore, from Eqn.(7.11), the fluidising pressure for a wedge consisting of adhesive particles is presented as

$$\Delta p_f = \frac{\ln(H/r_0)}{2\alpha_w \omega_0 (H - r_0)} (W + C_K \rho_p d_p A_s \cos\alpha_w \cdot K) \tag{7.16}$$

Besides, as $p_0 \approx \Delta p_f$ in spite of the small difference explained in Section 7.3.2, the cavity evolution with adhesive particles is approximately expressed as

$$V = (k_1 t^2 + k_2 t)[p - \frac{\ln(H/r_0)}{2\alpha_w \omega_0 (H - r_0)}(W + C_k \rho_p d_p A_s \cos\alpha_w \cdot K)] \qquad (7.17)$$

Eqn.(7.17) indicates that due to the presence of adhesive particles, the cavity size is roughly decreased linearly with K increases for a given soil sample at a particular time. Figure 7.13 plots the cavity size against K using the numerical results presented in Figure 7.12. It can be seen that the above finding agrees well with the numerical results.

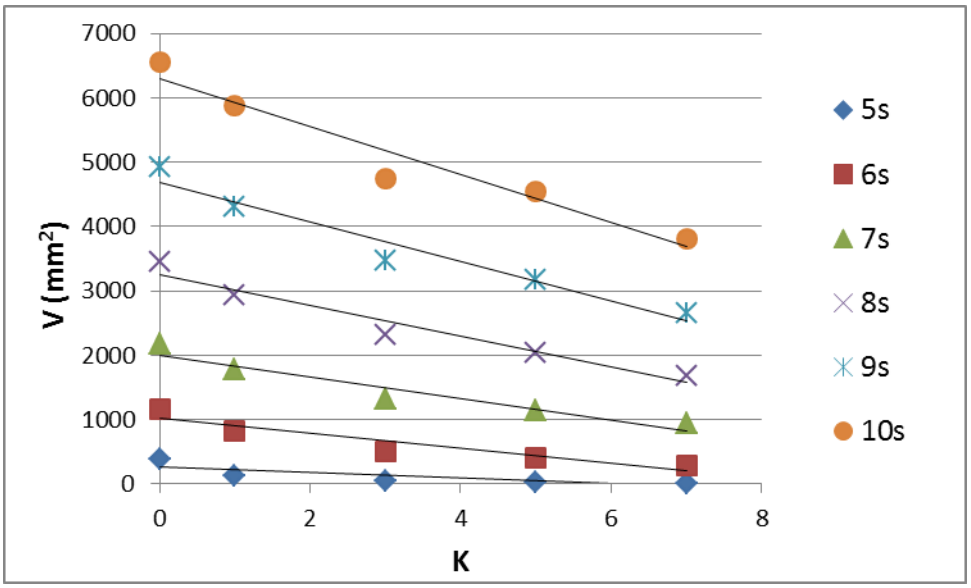

Figure 7.13 Cavity size vs. K

7.5 Relationship between Inter-particle Adhesion and Undrained Shear Strength

As previously mentioned, the adhesive particles are adopted with non-zero surface energy Γ to simulate the mechanical effect of soil cohesion. However, how this parameter on the particulate level relates to cohesion on the soil assembly level has not

been quite clearly defined so far, and very limited work has been found in literature regarding this issue. Therefore, this section aims to explore if any general correlations exist between the particle surface energy value and the undrained shear strength c_u.

A slope stability problem is considered in this section. DEM simulations are carried out on an upright slope formed by adhesive particles. These particles firstly dropped into a rectangular container under gravitational force. After the particles have fully settled (see Figure 7.14), the confining wall on the left is removed, allowing the left end of the soil moving freely under the effect of gravity. In the simulations, around 16,000 circular particles are adopted. During the tests, the DEM friction coefficient is set to zero so that the restraints of sliding between particles are only provided through inter-particle adhesion. Table 7.3 shows the simulation parameters used in the tests.

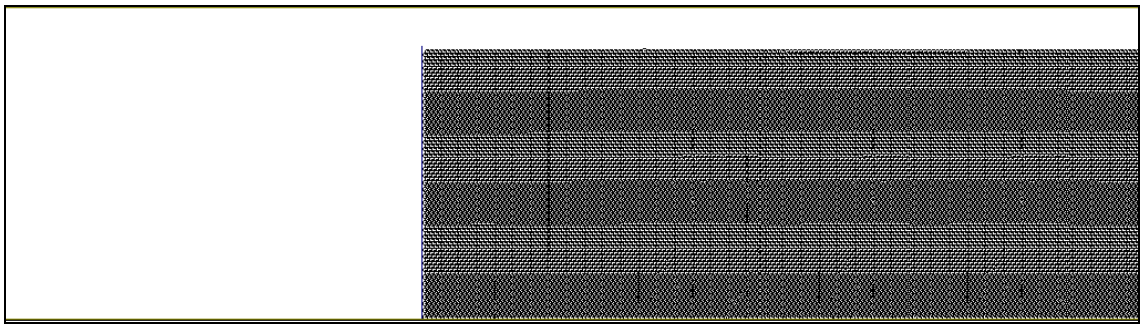

Figure 7.14 An upright slope is fully settled under gravitational force using DEM

Table 7.3 Parameters used in the slope stability tests

Parameters	Values
particle density (kg/m^3)	2700
inter-particle friction coefficient	0.0
Young's modulus of particle (MPa)	69
Poisson's ratio of particle	0.3
DEM time step (s)	1.0×10^{-5}

Numerical tests are conducted using different particle weights and sizes. By varying the input particle surface energy value, the left end of the soil may either collapse (see Figure 7.15), or remain globally stable (see Figure 7.16) after the removal of the confining wall. The minimum value of the input surface energy to maintain the global stability for each test is then determined for a given particle weight and size.

Figure 7.15 The slope loses its global stability after the removal of the confining wall

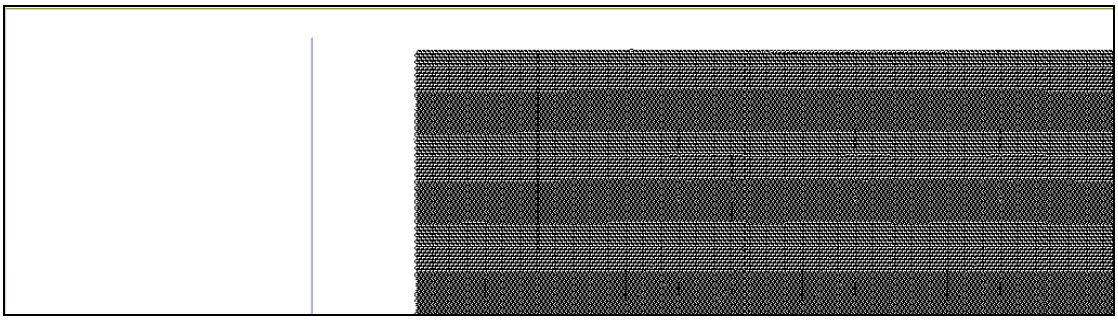

Figure 7.16 The slope remains stable after the removal of the confining wall

On the other hand, in order to maintain the condition of limit equilibrium of a particular homogeneous slope of height H, the minimum shear strength is calculated as shown in Eqn.(7.18) (Craig, 2004):

$$c_u = N_s F \gamma_{sat} H \tag{7.18}$$

where N_s is the Taylor's stability coefficient (Taylor, 1937; see Figure 7.17) which depends on the slope angle and the depth factor. For the tests reported in this section, the slope angle is 90° and the depth factor is 1.0, and hence $N_s = 0.26$. F is the factor of safety with respect to shear strength, which is unity in this study as the soil is at limiting equilibrium. γ_{sat} is the saturated unit weight of the soil, and is calculated from the porosity and particle density.

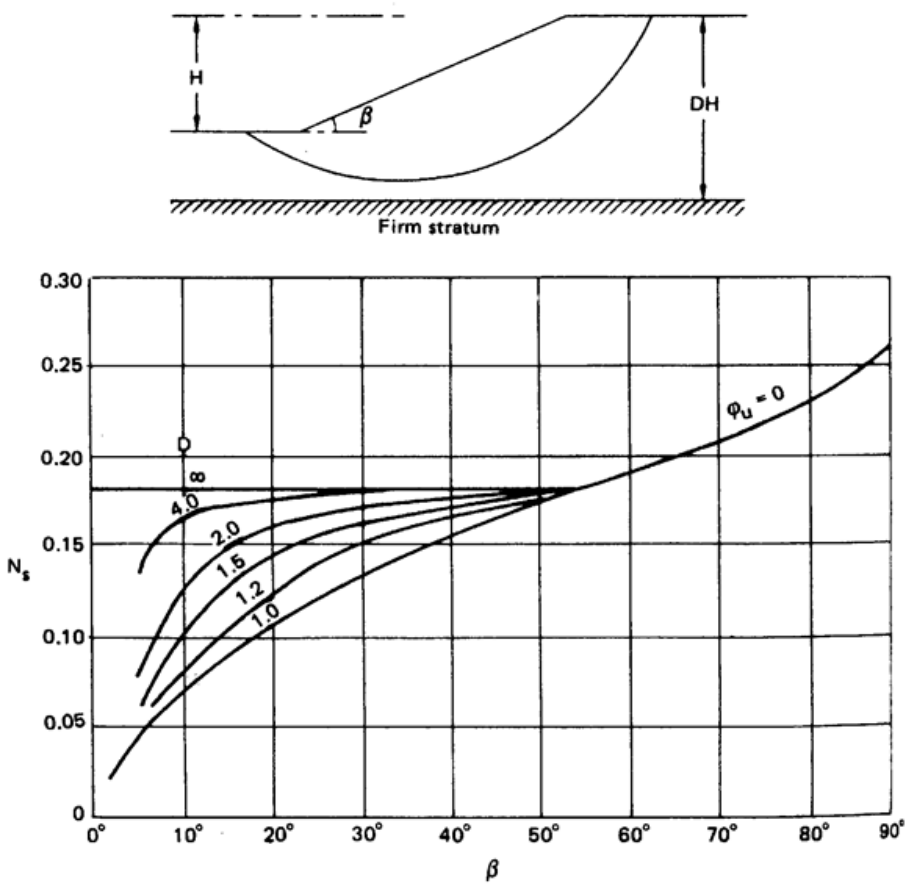

Fig. 9.3 Taylor's stability coefficients for $\phi_u = 0$. (Reproduced by permission of the Boston Society of Civil Engineers.)

Figure 7.17 Taylor's stability coefficients for $\varphi_u = 0$ (Boston Society of Civil Engineers as found in Craig, 2004)

The test results are presented in Table 7.4. By varying the particle weight, the numerical results indicate that the calculated shear strength is proportional to the surface energy value for a given particle size. This is shown in Figure 7.18 where c_u is plotted against Γ.

Table 7.4(1) Test results for the slope stability problem (to be continued)

Particle diameter d_p (mm)	Weight of a single particle (N)	γ_{sat} (kN/m^3)	H (m)	c_u (kPa)	Γ (J/m^2)
0.5	4.37×10^{-6}	40.17	0.035	0.36	0.23
	2.91×10^{-6}	26.79	0.035	0.24	0.16
	1.46×10^{-6}	13.39	0.035	0.12	0.08
	1.09×10^{-6}	10.05	0.035	0.09	0.07
	5.46×10^{-7}	5.02	0.035	0.05	0.04
1.0	1.75×10^{-5}	20.11	0.069	0.36	0.5
	8.74×10^{-6}	10.08	0.069	0.18	0.27
	6.99×10^{-6}	8.03	0.069	0.14	0.23
	5.24×10^{-6}	6.02	0.069	0.11	0.17
	3.49×10^{-6}	4.02	0.069	0.07	0.11
	1.75×10^{-6}	2.01	0.069	0.04	0.06

Table 7.4(2) Test results for the slope stability problem (cont.)

Particle diameter d_p (mm)	Weight of a single particle (N)	γ_{sat} (kN/m^3)	H (m)	c_u (kPa)	Γ (J/m^2)
2.0	6.99×10^{-5}	10.06	0.139	0.36	0.91
	3.49×10^{-5}	5.02	0.139	0.18	0.57
	2.33×10^{-5}	3.35	0.139	0.12	0.36
	1.40×10^{-5}	2.01	0.139	0.07	0.25
	6.99×10^{-6}	1.00	0.139	0.04	0.15
4.0	2.79×10^{-4}	5.03	0.277	0.36	1.79
	2.23×10^{-4}	4.02	0.277	0.29	1.40
	1.68×10^{-4}	3.01	0.277	0.22	1.00
	1.12×10^{-4}	2.01	0.277	0.14	0.91
	5.59×10^{-5}	1.01	0.277	0.07	0.51

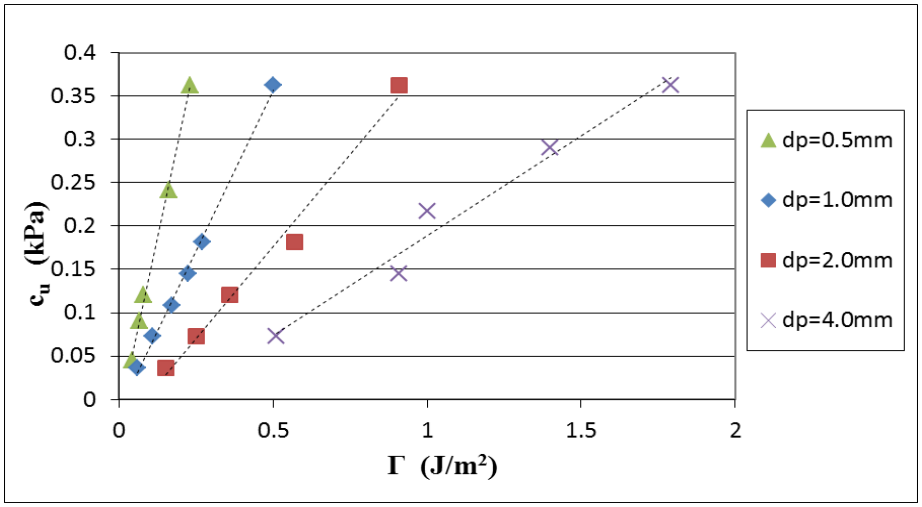

Figure 7.18 Relationship between c_u and Γ for different particle diameters

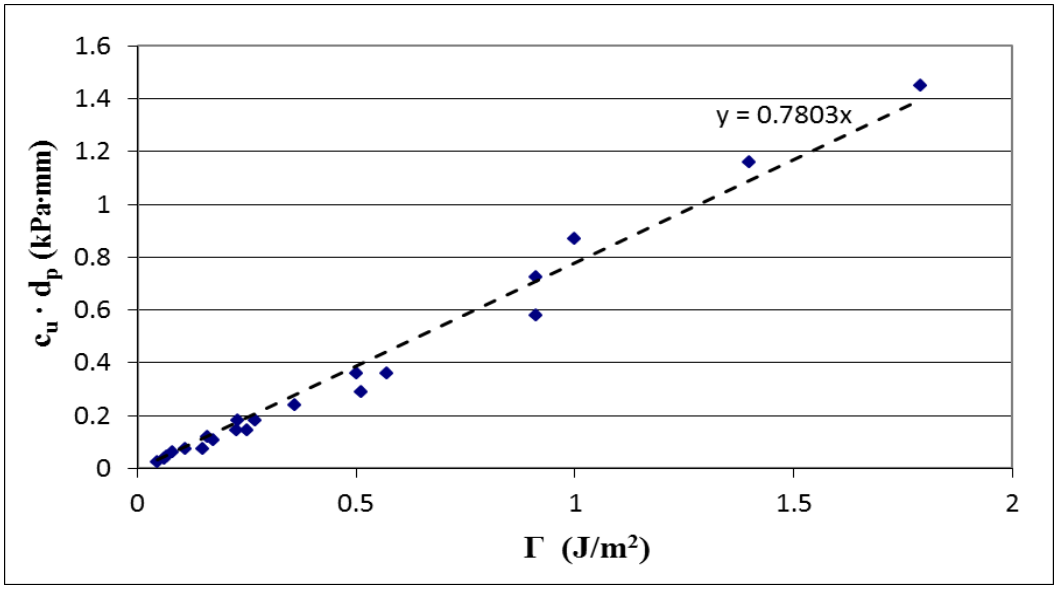

Figure 7.19 Relationship between $c_u \cdot d_p$ and Γ

By plotting all the data points using a $c_u \cdot d_p$ versus Γ graph (see Figure 7.19), the approximate relationship can be obtained with good correlation as,

$$c_u(kPa) = \frac{0.78\Gamma(J/m^2)}{d_p(mm)} \tag{7.19}$$

From Eqns.(3.29) and (3.30), it can be obtained that

$$\Gamma = \frac{2}{9}\rho_p {d_p}^2 g \cdot K \tag{7.20}$$

Substituting Eqn.(7.20) into Eqn.(7.19), the relationship between c_u and K can be deduced as

$$c_u(kPa) = \frac{1.56}{9}\rho_p d_p(mm) g \cdot K \tag{7.21}$$

Therefore, a general expression is given as

$$c_u = C_K \rho_p d_p K \tag{7.22}$$

where C_K is a constant for a given soil sample.

Eqn.(7.22) reveals that, by adopting the particle surface energy in DEM, the shear strength contributed from cohesion in a given soil can be described as a linear function of K, which is the ratio of inter-particle adhesion force to average particle weight. Such a relationship is employed to explore how cohesion influences the fluidising pressure and cavity evolution, as demonstrated in Section 7.4.

7.6 Summary

In this chapter, parametric studies are carried out to investigate the cavity evolution. The cavity size is given as functions of time, controlled flow rate, controlled pressure in the pipe, and the ratio of inter-particle adhesion force to average particle weight. With the flow rate being controlled constant during the test, the cavity size is found to be linearly developing with time; while with the pressure in the pipe being controlled constant, it becomes a quadratic function of time. Moreover, Eqns.(7.4) and (7.8) also indicate that, at a particular time, the cavity grows to a size which is either proportional to the flow rate excess the critical one (i.e. $Q - Q_0$), or to the pressure in the pipe excess the theoretical fluidising pressure (i.e. $p - p_0$).

With the presence of adhesive particles, the mechanical effect of soil cohesion is explored. By studying a slope stability problem in Section 7.5, the linear contribution of the inter-particle adhesion force to the undrained shear strength of the soil is identified. Such a correlation is adopted in the pipe leakage problem, and it is deduced that the cavity size is roughly reduced linearly with the increase in adhesion force at a particular time for a given soil sample. This finding is further evidenced by numerical results from a parametric study adopting various inter-particle adhesion forces.

CHAPTER 8: CONCLUSIONS AND FUTURE WORK

8.1 Conclusions of this Thesis

Motivated by the internal fluidisation phenomenon due to a pipe leakage, which has been recognised as a potential threat to infrastructures, this thesis aims to achieve a deeper understanding of the leakage-soil interaction. The problem is regarded complicated in nature, where fluid flows are localised and non-laminar at the vicinity of the leak, and involving intensive fluid-particle interactions after fluidisation occurs. Moreover, due to the localised large displacements in soil, continuum analytical methods would encounter difficulties. Besides, laboratory tools are regarded limited in flexibility and data acquisition especially under three-dimensional conditions. For the above reasons, numerical simulations are adopted in order to efficiently fulfill the aim of this thesis.

From literature, the coupled DEM-LBM technique is identified as an appropriate numerical tool to simulate the complicated behaviour of the problem. This is mainly due to the discrete nature of DEM as well as the microscopic nature of LBM. With the aid of the soft-sphere DEM model, complete information of each particle in an assembly can be obtained. When coupled with LBM, solid particles are merged into a fine Eulerian lattice. Incorporated with the Immersed Moving Boundary (IMB) scheme, DEM-LBM is capable of providing a smooth solution to the fluid-particle interactions with local descriptions.

A two-dimensional DEM-LBM computer program *FPS-BHAM* is therefore developed for this thesis. It consists of the following main elements:

(i) to establish the DEM calculation process, including transferring the contact force calculations from a well-established DEM code, *TRUBAL* ;

(ii) to implement the LBM computation with different boundary conditions; and

(iii) to incorporate the IMB scheme to LBM.

In order to identify failures and to correctly implement all the algorithms in the newly-established *FPS-BHAM*, a series of simple tests are carried out in Chapter 4. Through simulating the particle-wall and particle-particle collisions, the DEM calculations in *FPS-BHAM* are examined by comparing the computational results with those from *TRUBAL*. A slight difference is observed and can be attributed to round-off error and different DEM calculation procedures. In spite of the difference, *FPS-BHAM* provides valid results for tracing particle locations after contacts. On the other hand, in order to verify whether the LBM computations are correctly implemented, the Poiseuille flows with velocity and pressure boundaries, as well as the Couette flows with moving solid boundaries are simulated, respectively. The results are validated against analytical solutions. It is found *FPS-BHAM* not only achieves valid solutions, but also effectively obtains the fluid-induced torque acted on the moving boundary.

Code verifications in Chapter 4 imply the potential capability of *FPS-BHAM* in simulating a fluid-particle system. Hence, a granular bed subject to a locally injected fluid is tested using *FPS-BHAM* in Chapter 5. From the numerical results, different regimes of bed behaviour are obtained under various flow rates. With the controlled flow rate increased among tests, the bed sequentially undergoes the following behaviours: (i) the fixed-bed regime; (ii) the stable-cavity regime; (iii) the growing-cavity regime; and (iv) the blow-out regime. This is also evidenced by previous experimental studies (Zoueshtiagh and Merlen, 2007; Royal et al., 2008; and Alsaydalani, 2010).

It is recognised that seepage flows prevail in the fixed-bed regime, where a greater excess pressure is generated at a deeper location, which is closer to the source of flow. Although the pressures are initially accumulating with time, they finally reach a steady state with no fluidisation being initiated. Unlike the linear pressure distribution in a one-dimensional upward seepage, the excess pressure in a local leakage problem shows significant concentrations close to the source of flow. This is interpreted as a localisation nature.

If a higher flow rate is applied, fluidisation is observed at the source of flow, characterised by a sudden cavity formation and a sharp drop in the orifice pressure. The bed humps in the middle due to cavity formation, and the sharp pressure drop is attributed to the sudden ‘unblocking’ of surrounding particles. Both the experimental (Alsaydalani, 2010) and numerical results identify the onset of fluidisation from the most significant pressure

gradient near the orifice. And the critical hydraulic gradient is found to be greater than that of a normal seepage failure. The cavity being generated is recognised as the 'internally fluidised zone'. In this zone, particles are moving freely with the leaking fluid. An uplifting zone is also identified above the cavity, and particles in this zone are being raised at the onset of fluidisation, while those outside it remain steady. Both experimental and numerical results show that the uplifting zone is of an inverted-tapered shape. And the numerical tests demonstrate a reasonably similar wedge angle with that measured from the experiments.

The previous prediction of fluidising pressure in literatures was based on the assumption of a vertical flow distribution. However, this is not exactly true in a real soil subject to a local leakage. Although Alsaydalani (2010) argued that the leaking fluid should be spreading radially, there was no further evidence provided by his results. With the aid of numerical simulation, a radial flow distribution is obtained before fluidisation occurs. Hence, the flow equation is modified in this thesis according to the radial distribution. An approximate logarithmic nature is found out in the modified flow equation, which is also supported by simulation results.

As proofed by Alsaydalani (2010), at the onset of fluidisation, a force balance on the uplifting wedge is achieved between its bulk weight and the upward drag force. Based on this mechanism, the fluidising pressure is therefore derived for the radial flow distribution

in this thesis. The numerically measured fluidising pressures are found to match well with the predicted ones using the derived expression. Furthermore, from the analytical derivation, it is recognised that the fluidising pressure is approximately in direct proportion to an equivalent height H' (as defined by Eqn.(5.15)), provided that the seepage flow is primarily dominated by the first order of superficial velocity. This is also evidenced by the numerical solutions.

In addition, the post-fluidisation behaviour is explored in this thesis. A special attention is firstly paid to the 'stable-cavity' regime, where cavity stops growing in a short period after its formation. Chapter 6 studies on such a regime and the results suggest that a radial seepage flow still prevails above the cavity. Compared to the case before fluidisation, it is found out that the porosity above the cavity is increased while the fluid flow possesses higher velocity in the cavity. With the velocity vectors being plotted, local vortices are identified within the cavity. Moreover, p-t curves indicate that a steady state is achieved in soil after the cavity stops growing, and the pressure distribution above the cavity still exhibits the logarithmic nature. Furthermore, from the numerical outcome at the steady state, it is argued that a new force balance is achieved by the combined actions of the drag force, the wedge weight, and the upward friction generated due to horizontal supports provided by fluid pressure in the cavity.

With a higher flow rate being applied, the cavity is continuously growing. Its evolution is

investigated in Chapter 7. Analysing the numerical results from parametric studies, the cavity size is expressed as functions of time, controlled flow rate, controlled pressure in the pipe, and the ratio of inter-particle adhesion force to average particle weight. With a constant flow rate, the cavity size is found to be linearly increasing with time; while with a constant pressure in the pipe, it becomes a quadratic function of time. Moreover, at a particular time, the cavity grows to a size which is either proportional to the flow rate excess the critical one (i.e. $Q - Q_0$), or to the pressure in the pipe excess the theoretical fluidising pressure (i.e. $p - p_0$).

With the presence of adhesive particles, the mechanical effect of soil cohesion is explored. Unlike a more smooth and rounded cavity in the case with non-adhesive particles, the cavity tends to have a branch-like or needle-like shape with inter-particle adhesion force. Similar cavity shapes were also obtained by Royal et al. (2008) when they conducted laboratory tests on clayey soils. By studying a slope stability problem, it is identified a linear contribution of the inter-particle adhesion force to the undrained shear strength of the soil. Adopting such a correlation in the pipe leakage problem, it is then deduced that for a given soil sample, the cavity size is approximately linearly reduced by the increase in the inter-particle adhesion force. This finding is further evidenced by numerical results from a parametric study.

Furthermore, numerical simulations also demonstrate a blow-out failure when the cavity grows up to the bed surface so as to open up a fluid channel. Fluctuations are observed in the p-t curves, indicating unsteady flow behaviour. In addition, excess pressures at shallower locations are occasionally greater than those at deeper ones, suggesting backward flows and local vortices. With an extremely high flow rate, the excess pressure near the orifice may even increase during the cavity development due to such a rapid energy input. An unsymmetrical pattern of the channel shape is also noticed, which is attributed to the non-zero horizontal momentum of the injected fluid, as well as the unsymmetrical soil skeleton and the amplified difference in the unstable system.

8.2 Future Work

As the numerical investigations presented in this thesis are still at an early stage, some recommendations for the future work are given as follows:

- In the current two-dimensional simulations, fluid paths through the particle assembly are considered by artificially adopting the hydraulic radius. This makes the determination of permeability ambiguous, although it is sometimes necessary to obtain the flow field in soil. Moreover, the current model is difficult to give an explicit description of turbulent flow which involved at the vicinity of the orifice, as it is actually a three-dimensional phenomenon. Therefore, it is expected to extend the simulations by *FPS-BHAM* to three-dimensional ones, by

which the physical behaviour can be captured more accurately.

- With the current sample bed, the superficial velocity is sufficiently low, so that the flow equation before fluidisation occurs (see Eqn.(5.12) is simplified by neglecting the second-order term of superficial velocity. However, if a different soil sample is used, particularly a soil with higher permeability, the superficial velocity may be higher and its second term may be of importance in the flow equation. Besides, for a soil lack of medium grain sizes, piping (i.e. internal erosion) may take place where fine grains are washed away before the overall soil skeleton being largely deformed. For the above reasons, particle size and its distribution shall be varied in future studies, so as to explore on the effect of different permeability and potential of piping phenomenon.
- Moreover, in the current numerical model, only liquid-solid two phases are simulated and the soil is considered fully submerged under water. In the future, it would be worth extending the simulations to partially saturated soils by incorporating multi-phase fluid models, so that both the pore water and pore air can be simulated along with the solid phase.
- Furthermore, the wedge angle of the uplifting zone has not been fully investigated. It is believed that this angle may be dependent on the soil friction, which is further related to inter-particle friction and particle interlocks. Hence, different DEM particle friction coefficients and particle shapes are expected to be adopted in future studies. In addition, the relationship of the macroscopic soil

friction and the inter-particle friction is also required to be explored, in an effort to quantify the effect of soil friction on the wedge angle.

- More samples would be tested in the future so that the effects of bed geometry and orifice size and shape can be explored.
- Besides, in the research presented in this thesis, the leaking pipe is simply viewed as a fluid channel which provides a source of flow. However, in a real pipe leakage problem, the pipe itself may suffer from external loads due to the stress changes in soil which may lead to further breaks or leaks. Therefore, in the further, the interaction between the soil and pipe shall also be considered along with the leakage-soil interaction.

REFERENCES

Al-Karni, A.A.S. (1995). An experimental study on the stability of foundations due to water flowing from broken underground pipelines. The International Conference on Earthquake Engineering, Amman, Jordan, 482-490.

Al-Karni, A.A.S. (2000). Stability of saturated cohesionless soil layer due to water flowing from a broken underground pipeline. Journal of King Saud University, Engineering Science, **12**(1), 27-44.

Alsaydalani, M.O.A. (2010). Internal fluidisation of granular material. PhD thesis, University of Southampton.

Anandarajah, A. (2000). Numerical simulation of one-dimensional behaviour of kaolinite. Géotechnique, **50**(5), 509-519.

Anandarajah, A. (2003). Discrete element modelling of leaching-induced apparent overconsolidation in kaolinite. Soils and Foundations, **43**(6), 1-12.

Bonilla, R.R.O. (2004). Numerical simulations of undrained granular media. PhD thesis, University of Waterloo.

Boutt, D.F., Cook, B.K., McPherson, B.J.O.L., and Williams, J.R. (2007). Direct simulation of fluid-solid mechanics in porous media using the discrete element and lattice-Boltzmann methods. Journal of Geophysical Research B: Solid Earth, **112**, B10209.

Brenner, G. (2004). Application of Lattice-Boltzmann Methods in Fluid Mechanics. Extended abstract, Institute of Applied Mechanics, University of Clausthal.

Bui, H.H., Sako, K., and Fukagawa, R. (2007). Numerical simulation of soil-water interaction using smoothed particle hydrodynamics (SPH) method. Journal of Terramechanics, **44**(5), 339-346.

Campbell, C.S. and Brennen, C.E. (1985). Computer simulations of granular shear flows. Journal of Fluid Mechanics, **151**, 167–188.

Chen, S., Chen, H.D., Martinez, D., and Matthaeus, W. (1991). Lattice Boltzmann model for simulation of magnetohydrodynamics. Phys Rev. Lett. **67**, 3776-3779.

Chen, S. and Doolen, G.D. (1998). Lattice Boltzmann method for fluid flows. Annual Review of Fluid Mechanics, **30**, 329–364.

Chen, Y., Ohashi, H., and Akiyama, M. (1995). Heat transfer in lattice BGK modeled fluid. J. Stat. Phys., **81**(1/2), 71-85.

Clayton, C.R.I., Xu, M., Whiter, J.T., Ham, A., and Rust, M. (2010). Stresses in cast-iron pipes due to seasonal shrink-swell of clay soils. Proceedings of ICE, Water Management, 163(3), 157-162.

Cook, B.K., Noble, D.R., Preece, D.S., and Williams J.R. (2000). Direct simulation of particle-laden fluids. Pacific Rocks 2000, 279-286.

Cook, B.K., Noble, D.R., and Williams, J.R. (2004). A direct simulation method for particle-fluid systems. Engineering Computations, **21**(2-4), 151-168.

Craig, R.F. (2004). Craig's soil mechanics, seventh edition. Taylor & Francis Group.

Crespo, A.J.C. (2008). Application of the smoothed particle hydrodynamics model SPHysics to free-surface hydrodynamics. PhD thesis, Universidade de Vigo.

Cundall, P.A. (1971). A computer model for simulating progressive, large-scale movements in blocky rock systems. Proceedings Symposium of International Society for Rock Mechanics, **2**, 132-150.

Cundall, P.A. (1974). A computer model for rock-mass behaviour using interactive graphics for the input and output of geometrical data. Report for the Missouri River Division, U.S. Army Corps of Engineers, University of Minnesota.

Cundall, P.A. (1978). BALL-A computer program to model granular media using the distinct element method. Technical note TN-LN-13, Advance Technology Group, Dames and Moore, London.

Cundall, P.A. (1988). Computer simulations of dense sphere assemblies. Micromechanics of Granular Materials, Satake and Jenkins (eds), Elsevier Science Publishers, Amsterdam, Netherlands, 113-123.

Cundall, P.A. and Strack, O.D.L. (1978). The discrete element method as a tool for research in granular media. Part I. Report to National Science Foundation, University of Minnesota.

Cundall, P.A. and Strack, O.D.L. (1979a). The development of constitutive laws for soil using the distinct element method. Third International Conference on Numerical Methods in Geomechanics, Wittke (Eds), Balkema, Aachen, 289-298.

Cundall, P.A. and Strack, O.D.L. (1979b). A discrete numerical model for granular assembilies. Geotechnique, **29**(1), 47-65.

Cundall, P.A. and Strack, O.D.L. (1979c). The discrete element method as a tool for research in granular media. Part II. Report to National Science Foundation, University of Minnesota.

Deen, N.G., Van Sint Annaland, M., Van der Hoef, M.A., and Kuipers, J.A.M. (2007). Review of discrete particle modeling of fluidised beds. Chemical Engineering Science, **62**(1-2), 28-44.

Duran, J. (2000). Sands, powders, and grains: An introduction to the physics of granular materials, Springer, New York.

El Shamy, U. and Gröger, T. (2008). Micromechanical aspects of the shear strength of wet granular soils. Int. J. Numer. Anal. Methods Geomech., **32**(14), 1763-1790.

El Shamy, U., Zeghal, M., Shephard, M., Dobry, R., Fish, J., and Abodoun, T. (2002). Discrete element simulations of water flow through granular soils. 15th ASCE Engineering Mechanics Conference, Columbia University, New York..

Elhoud, A.M. (2012). Internal degradation of buried sewage pipe causes sinkhole in a main road. The Indian Concrete Journal/May, 2012, **86**(5), 52-56.

Ergun, S. (1952). Fluid flow through packed columns. Chemical Engineering Progress, **43**(2), 89-94.

Fell, R., Wan, C.F., Cyganiewicz, J., and Foster M. (2001). The time for development and detectability of internal erosion and piping in embankment dams and their foundations. UNICIV report R-399, University of New South Wales.

Feng, Y.T., Han, K., and Owen, D.R.J. (2007). Coupled lattice Boltzmann method and discrete element modelling of particle transport in turbulent fluid flows: computational issues. International Journal for Numerical Methods in Engineering, **72**(9), 1111-1134.

Feng, Y.T., Han, K., and Owen, D.R.J. (2010). Combined three-dimensional lattice Boltzmann method and discrete element method for modelling fluid–particle interactions with experimental assessment. International Journal for Numerical Methods in Engineering, **81**(2), 229–245.

Feng, Y.Q. and Yu, A.B., (2006). Discrete particle simulation of size segregation of particle mixtures in a gas fluidized bed. China Particuology, **4**(3-4), 122-126.

Foster, M., Fell, R., and Spannagle, M. (2000). The statics of embankment dam failures and accidents. Canadian Geotechnical Journal, **37**, 1000-1024.

Frisch, U., Hasslacher, B., and Pomeau, Y. (1986). Lattice-gas automata for the Navier-Stokes equations. Phys. Rev. Lett., **56**, 1505-1508.

Gernon, T.M., Gilbertson, M.A., Sparks, R.S.J., and Field, M. (2008). Gas-fluidisation in an experimental tapered bed: insights into processes in diverging volcanic conduits. Journal of Volcanology and Geothermal Research, **174**(1-3), 49-56.

Gingold, R.A. and Monaghan, J.J. (1977). Smoothed particle hydrodynamics: theory and application to non-spherical stars. Monthly Notices Royal Astronomical Society, **181**, 375–389.

Gong, G.B. (2008). DEM simulations of drained and undrained behaviour. PhD thesis, University of Birmingham.

Gong, G.B., Thornton, C., and Chan, A.H.C. (2012). DEM simulations of undrained triaxial behaviour of granular material, ASCE EM, **138**(6), 560-566.

Hakuno, M. and Tarumi, Y. (1988). Granular assembly simulation for the seismic liquefaction of sand. Doboku Gakkai Rombun-Hokokushu/Proceedings of the Japan Society of Civil Engineers, **398**(I-10), 129-138.

Han, K., Feng, Y.T., and Owen D.R.J. (2007a). Numerical simulations of irregular particle transport in turbulent flows using coupled LBM-DEM. Computer Modeling in Engineering and Sciences, **18**(2), 87-100.

Han, K., Feng, Y.T., and Owen D.R.J. (2007b). Coupled lattice Boltzmann and discrete element modelling of fluid-particle interaction problems. Computers and Structures, **85**(11-14), 1080-1088.

Hardy, J., de Pazzis, O., and Pomeau, Y. (1976). Molecular dynamics of a classical lattice gas: transport properties and time correlation functions. Phys. Rev., **A**(13), 1949-1961.

Higuera, F.J. and Jiménez, J. (1989). Boltzmann approach to lattice gas simulations. Europhys. Lett., **9**, 663-668.

Higuera, F.J., Succi, S., and Benzi, R. (1989). Lattice gas dynamics with enhanced collisions. Europhys. Lett., **9**, 345-349.

Hoomans, B.P.B., Kuipers, J.A.M., Briels, W.J., and Van Swaaij, W.P.M. (1996). Discrete particle simulation of bubble and slug formation in a two-dimensional gas-fluidised bed: a hard-sphere approach. Chemical Engineering Science, **51**(1), 99–118.

Hou, S., Sterling, J., Chen, S., and Doolen, G.D. (1996). A lattice Boltzmann subgrid model for high Reynolds number flows. Fields Institute Communications, **6**, 151-166.

Hu, H.H. (1996). Direct simulation of flows of solid–liquid mixtures. International Journal of Multiphase Flow, **22**, 335–352.

Huang, H., and Detournay, E. (2008). Intrinsic length scales in too-rock interaction. Int. J. Geomech., **8**(1), 39-44.

Jensen, R.P., Bosscher, P.J., Plesha, M.E., and Edil, T.B. (1999). DEM simulation of granular media-structure interface: effects of surface roughness and particle shape. Int. J. Numer. Anal. Meth. Geomech., **23**, 531-547.

Jensen, R.P. and Preece, D.S. (2000). Modelling sand production with Darcy-flow coupled with discrete elements. Sandia National Laboratories Reports.

Jiang, M.J., Leroueil, S., and Konrad, J.M. (2004). Insight into shear strength functions of unsaturated granulates by DEM analyses. Comput. Geotech., **31**(6), 473-489.

Johnson, K.L. (1985). Contact Mechanics. Cambridge University Press.

Johnson, K.L., Kendall, K., and Roberts, A.D. (1971). Surface energy and the contact of elastic solids. Proceedings of the Royal Society of London, Series A (Mathematical and Physical Sciences), **324**(1558), 301-313.

Kafui, K.D., Thornton, C., and Adams, M.J. (2002). Discrete particle-continuum fluid modelling of gas-solid fluidised beds. Chemical Engineering Science, **57**(13), 2395-2410.

Kawaguchi, T., Tanaka, T., and Tsuji, Y. (1998). Numerical simulation of two-dimensional fluidised beds using the discrete element method (comparison between the two- and three-dimensional models). Powder Technology, **96**(2), 129–138.

Kishino, Y. (1998). Disc model analysis of granular media. Micromechanics of granular materials. Satake and Jenkins (eds), Elsevier Science Publishers, Amsterdam, Netherlands, 143-152.

Kunkel, G., Laven, K., and Mergelas, B. (2008). Field report -- does your city have high-risk pipes? Journal AWWA, **100**(4), 70-74.

Ladd, A. (1994). Numerical simulations of fluid particulate suspensions via a discretized Boltzmann equation (Parts I & II). J. Fluid Mech., **271**, 285-339.

Ladd, A. and Verberg, R. (2001). Lattice-Boltzmann simulations of particle-fluid suspensions. J. Statist. Phys., **104**(5/6), 1191-1251.

Li, J. (2006). Two dimensional simulation of a stiffened slab on expansive soil subject to a leaking underground water pipe. 4th International Conference on Unsaturated Soils, Arizona, 2098-2109.

Li, J. (2012). Numerical investigations of the coupled DEM-LBM technique with application to leakage-soil interaction due to a leaking pipe. PhD Thesis, University of Birmingham.

Li, X.K., Chu, X.H., and Sheng, D.C. (2007). A saturated discrete particle model and characteristic-based SPH method in granular materials. International Journal For Numerical Methods In Engineering, **72**, 858-882.

Lin, X. and Ng, T.-T. (1997). A three-dimensional discrete element model using arrays of ellipsoids. Geotechnique, **47**(2), 319-329.

Liu, G.R. and Liu, M.B. (2003). Smoothed particle hydrodynamics: a meshfree particle method. World Scientific.

Lynch, M. and Stimpson, J. (2011). Network Rail battles to cure Croydon lines after mudslide, New civil engineer/18.08.11, 5.

Maeda, K. and Ibraim, E. (2008). DEM analysis of 2D fibre-reinforced granular soils. IS Atlanta 2008: Deformation Characteristics of Geomaterials, **2**, 623-628.

Makar, J.M. (2000). A preliminary analysis of failures in grey cast iron water pipes. Engineering Failure Analysis, **7**(1), 43-53.

Malvern, L. (1969). Introduction to the mechanics of a continuous medium. Prentice-Hall.

Mansouri, M., Delenne, J.Y., El Youssoufi, M.S., and Seridi, A. (2009). A 3D DEM-LBM approach for the assessment of the quick condition for sands. Comptes

Rendus Mecanique, **337**(9-10), 675-681.

Mansouri, M., Delenne, J.Y., Seridi, A., and El Youssoufi, M.S. (2010). Numerical model for the computation of permeability of a cemented granular material. Powder Technology, **208**(2), 532-536.

McNamara, G.R. and Zanetti, G. (1988). Use of the Boltzmann equation to simulate lattice-gas automata. Phys. Rev. Lett. **61**, 2332-2335.

Meguro, K. and Ravichandran, N. (2000). 3-dimensional distinct element simulation of liquefaction phenomena. Seisan-Kenkyu, **52**(12), 598-601.

Mindlin, R.D. (1949). Compliance of elastic bodies in contact. Journal of Applied Mechanics, **16**, 259-268.

Mindlin, R.D. and Deresiewicz, H. (1953). Elastic spheres in contact under varying oblique forces. Journal of Applied Mechanics, **20**, 327-344.

Nakase, H., Takeda, T., and Oda, M.A. (1999). Simulation study on liquefaction using DEM. Earthquake Geotechnical Engineering, **3**, 637-642.

Ng, T.-T. (2001). Fabric evolution of ellipsoidal arrays with different particle shapes. Journal of Engineering Mechanics, ASCE, **127**(10), 994-999.

Ng, T.-T. and Dobry, R. (1994). Numerical simulations of monotonic and cyclic loading of granular soil. Journal of Geotechnical & Geoenvironmental Engineering, **120**(2), 388–403.

Noble, D.R., Chen, S., Georgiadis, J.G., and Buckius, R.O. (1995). A consistent hydrodynamic boundary condition for the lattice Boltzmann method. Physics of Fluids, **7**(1), 203-209.

Noble D. and Torczynski J. (1998). A lattice Boltzmann method for partially saturated cells. International Journal of Modern Physics C, **9**, 1189–1201.

O'Connor, R.M., Torczynski, J.R., Preece, D.S., Klosek, J.T., and Williams, J.R. (1997). Discrete element modelling of sand production. International Journal of Rock Mechanics and Mining Sciences, **34**(3-4), paper No. 231.

O'Sullivan, C. (2011). Particle-based discrete element modelling: goemechanics perspective. International Journal of Geomechanics, **11**(6), 449-464.

Pan, T.W., Joseph, D.D., Bai, R., Glowinski, R. and Sarin, V. (2002). Fluidisation of 1204 spheres: simulation and experiment. Journal of Fluid Mechanics, **451**, 169–191.

Peng, Y. and Fan, L.T. (1997). Hydrodynamic characteristics of fluidization in liquid-solid tapered beds. Chemical Engineering Science, **52**(14), 2277-2290.

Peron, H., Delenne, J.Y., Laloui, L., and El Youssoufi, M.S. (2009). Discrete element modelling of drying shrinkage and cracking of soils. Comput. Geotech. **36**(1-2), 61-69.

Potapov, A.V., Hunt, M.L., and Campbell, C.S. (2001). Liquid-solid flows using smoothed particle hydrodynamics and the discrete element method. Powder Technology, **116**, 204-213.

Potyondy, D.O. and Cundall, P.A. (2004). A bonded-particle model for rock. International Journal of Rock Mechanics and Mining Sciences, **41**(8), 1329-1364.

Preece, D.S., Jensen, R.P., Perkins, E.D., and Williams, J.R. (1999). Sand production modeling using superquadric discrete elements and coupling of fluid flow and particle motion. Proceedings of the 37th U.S. Rock Mechanics Symposium.

Premnath, K.N., Nave, J.C. and Banerjee, S. (2005). Computation of multiphase flows

with Lattice Boltzmann methods. American Society of Mechanical Engineers, Fluid Engineering Division, **261**, 403-420.

Qian, Y.H. (1990). Lattice gas and lattice kinetic theory applied to the Navier-Stokes equations. PhD thesis. Universit é Pierre et Marie Curie, Paris.

Rajani, B. and Kleiner, Y. (2012). Fatigue failure of large-diameter cast iron mains. Proceedings of Water Distribution System Analysis 2010, 1146-1159.

Rajani, B., Lewandowski, J., and Margevicius, A. (2012). Failure analysis of cast iron trunk main in Cleveland, Ohio. J. Fail. Anal. and Preven., **12**, 217-236.

Rajani, B. and McDonald, S. (1994). Water main break data on different pipe materials for 1992 and 1993. National Research Council, Ottawa, Ontario.

Richards, K.S. and Reddy, K.R. (2007). Critical appraisal of piping phenomena in earth dams. Bull. Eng. Geol. Environ., **66**, 381-402.

Richefeu, V., Radjai, F., and El Youssoufi, M.S. (2006). Stress transmission in wet granular materials, The European Physical Journal E: Soft Matter and Biological Physics, **21**(4), 359-369.

Rogers, C.D.F., Chapman, D.N., and Royal, A.C.D. (2008). Experimental investigation of the effects of soil properties on leakage: final report. University of Birmingham.

Rogers, B. and Dalrymple, R.A. (2004). SPH modeling of breaking waves. Proceedings of the 29th International Conference on Coastal Engineering, 415-427.

Rothenburg, L. and Bathurst, R.J. (1992). Micromechanical features of granular assemblies with planar elliptical particles. Geotechnique, **42**(1), 79-95.

Royal, A.C.D., Rogers, C.D.F., Chapman, D.N., Prescott, A. and Algaard, E. (2008). Experimental investigation of the effects of soil properties on leakage. (unpublished)

Satofuka, N. and Nishioka, T. (1999). Parallelisation of lattice Boltzmann method for incompressible flow computations. Computational Mechanics, **23**(2), 164-171.

Shafipour, R. and Soroush, A. (2008). Fluid coupled-DEM modelling of undrained behavior of granular media. Computers and Geotechnics, **35**(5), 673-685.

Shi, Y.F., Yu, Y.S., and Fan, L.T. (1984). Incipient fluidization condition for a tapered fluidized bed. Industrial and Engineering Chemistry, Fundamentals, **23**(4), 484-489.

Shire, T. and O'Sullivan C. (2013). Micromechanical assessment of an internal stability criterion. Acta Geotechnica, **8**(1), 81-90.

Smagorinski, J. (1963). General circulation model of the atmosphere. Weather Rev., 99-164.

Söderlund M., Bots, P.J., Eriksson, P., Nilsson, P. and Hartlen, J. (2007). Evaluating the domino-effect of failure of critical constructions due to damage of underground water pipelines. Loss Prevention Bulletin, **195**, 22-27.

Steindorff, K. (2008). Sinking into a hole new level: Downtown sinkhole costs & concerns. The Undergrounder/February 2008, 19-20.

Supraksorn, T. (2009). Investigating the effects of soil type on leakage from water pipes. MSc dissertation, University of Birmingham.

Suzuki, K., Bardet, J.P., Oda, M., Iwashita, K., Tsuji, Y., Tanaka, T., and Kawaguchi, T. (2007). Simulation of upward seepage flow in a single column of spheres using discrete-element method with fluid-particle interaction. Journal of Geotechnical and Geoenvironmental Engineering, **133**(1), 104-109.

Taylor, D.W. (1937). Stability of earth slopes. J. Boston Soc. Civil Eng., **24**(3). Reprinted in: Contributions to Soil Mechanics 1925 to 1940, Boston Society of Civil Engineers, 337-386.

Terzaghi, K. (1939). Soil Mechanics: a new chapter in engineering science. Insinuation of Civil Engineers, **12**(1039), 106-141.

Thornton, C. (1991). Interparticle sliding in the presence of adhesion. Journal of Physics D (Applied Physics), **24**(11), 1942-1946.

Thornton, C. (2000). Numerical simulations of deviatoric shear deformation of granular media. Geotechnique, **50**(1), 43-53.

Thornton, C. and Ning, Z. (1998). A theoretical model for the stick/bounce behaviour of adhesive, elastic-plastic spheres. Powder Technology, **99**(2), 154-162.

Thornton, C. and Randall, C.W. (1988). Applications of theoretical contact mechanics to solid particle system simulation. Micromechanics of granular materials, Satake and Jenkins (eds), Elsevier Science Publishers, Amsterdam, Netherlands, 133-142.

Thornton, C. and Yin, K.K. (1991). Impact of elastic spheres with and without adhesion. Powder Technology, **65**(1-3), 153-166.

Ting, J.M., Meachum, L., and Rowell, J.D. (1995). Effect of particle shape on the strength and deformation mechanism of ellipse-shaped granular assemblages. Engineering Computations, **12**(2), 99-108.

Tsuji, Y., Kawaguchi, T., and Tanaka, T. (1993). Discrete particle simulation of two-dimensional fluidised bed. Powder Technology, **77**(1), 79–87.

Voivret, C., Radjai, F., Delenne, J.Y., and El Youssoufi, M.S. Space-filling properties of polydisperse granular media. Physical Review E – Statistical, Nonlinear, and Soft Matter Physics, **76**(2), 021301-1-021301-12.

van Zyl, J.E. and Clayton, C.R.I. (2007). The effect of pressure on leakage in water distribution systems. Proceedings of the Institution of Civil Engineers, Water Management 160, 109-114.

Wan, C.F. and Fell, R. (2008). Assessing the potential of internal instability and suffusion in embankment dams and their foundations. Journal of Geotechnical and Geoenvironmental Engineering, **134**(3), 401-407.

Wolfram, S. (1986). Cellular automaton fluids. 1: Basic theory. J. Stat. Phys. **45**, 471-526.

Wray, W.K., El-Garhy, B.M., and Youssef, A.A. (2004). Three-dimensional model for moisture and volume changes prediction in expansive soils. Journal of Geotechnical and Geoenvironmental engineering, **131**(3), 311-324.

Xu, B.H. and Yu, A.B. (1997). Numerical simulation of the gas-solid flow in a fluidised bed by combining discrete particle method with computational fluid dynamics. Chemical Engineering Science, **52**(16), 2785-2809.

Yang F. (2009). A numerical examination of the fluidised behaviour of Geldart's group A type particle beds. PhD thesis, University of Birmingham.

Zeghal, M. and El Shamy, U. (2008). Liquefaction of saturated loose and cemented granular soils. Powder Technology, **184**(2), 254-265.

Zhang, L. and Thornton, C. (2007). A numerical examination of the direct shear test. Geotechnique, **57**(4), 343-354.

Zhao, X.L., Li, S.Q., Liu, G.Q., Yao, Q., and Marshall, J.S. (2008). DEM simulation of the particle dynamics in two-dimensional spouted beds. Powder Technology, **184**(2), 205-213.

Zhou, X., Jie, Y., and Li, G. (2012). Numerical simulation of the developing course of piping. Computers and Geotechnics, **44**, 104-108.

Zhu, H.P., Zhou, Z.Y., Yang, R.Y., and Yu, A.B. (2007). Discrete particle simulation of particulate systems: Theoretical developments. Chemical Engineering Science, **62**(13), 3378–3396.

Zhu, H.P., Zhou, Z.Y., Yang, R.Y., and Yu, A.B. (2008). Discrete particle simulation of particulate systems: A review of major applications and findings. Chemical Engineering Science, **63**(23), 5728-5770.

Zou, Q. and He, X. (1997). On pressure and velocity boundary conditions for the lattice Boltzmann BGK model. Physics of Fluids, **9**(6), 1591–1598.

Zoueshtiagh, F. and Merlen, A. (2007). Effect of a vertically flowing water jet underneath a granular bed. Physical Review E 75, 056313-1-056313-12.